

























GEMS JWST: Transmission spectroscopy of TOI-5205b reveals significant stellar contamination and a metal-poor atmosphere

CALEB I. CAÑAS ^{1,*} JACOB LUSTIG-YAEGER ² SHANG-MIN TSAI ³ SIMON MÜLLER ⁴ RAVIT HELLED ⁴
DANA R. LOUIE ^{5,1,6} GIANNINA GUZMÁN CALOCA ^{7,1} SHUBHAM KANODIA ⁸ PETER GAO ⁸
JESSICA LIBBY-ROBERTS ^{9,10} KEVIN K. HARDEGREE-ULLMAN ¹¹ KNICOLE D. COLÓN ¹ IAN CZEKALA ¹²
MEGAN DELAMER ^{9,10} TE HAN ¹³ ANDREA S.J. LIN ¹⁴ SUVRATH MAHADEVAN ^{9,10} ERIN M. MAY ²
JOE P. NINAN ¹⁵ ANJALI A. A. PIETTE ¹⁶ GUÐMUNDUR STEFÁNSSON ¹⁷ KEVIN B. STEVENSON ²
JOHANNA TESKE ⁸ AND NICOLE L. WALLACK ⁸

¹NASA Goddard Space Flight Center, 8800 Greenbelt Road, Greenbelt, MD 20771, USA

²Johns Hopkins APL, 11100 Johns Hopkins Rd, Laurel, MD 20723, USA

³Department of Earth and Planetary Sciences, University of California, Riverside, CA, USA

⁴Department of Astrophysics, University of Zürich, Winterthurerstrasse 190, 8057 Zürich, Switzerland

⁵Catholic University of America, Department of Physics, Washington, DC, 20064, USA

⁶Center for Research and Exploration in Space Science and Technology II, NASA/GSFC, Greenbelt, MD 20771, USA

⁷Department of Astronomy, University of Maryland, College Park, MD 20742, USA

⁸Earth and Planets Laboratory, Carnegie Science, 5241 Broad Branch Road, NW, Washington, DC 20015, USA

⁹Department of Astronomy & Astrophysics, The Pennsylvania State University, 525 Davey Laboratory, University Park, PA 16802, USA

¹⁰Center for Exoplanets and Habitable Worlds, The Pennsylvania State University, 525 Davey Laboratory, University Park, PA 16802, USA

¹¹Caltech/IPAC-NASA Exoplanet Science Institute, 1200 E. California Blvd., MC 100-22, Pasadena, CA 91125, USA

¹²School of Physics & Astronomy, University of St. Andrews, North Haugh, St. Andrews KY16 9SS, UK

¹³Department of Physics & Astronomy, The University of California, Irvine, Irvine, CA 92697, USA

¹⁴Department of Astronomy, California Institute of Technology, 1200 E California Blvd, Pasadena, CA 91125, USA

¹⁵Department of Astronomy and Astrophysics, Tata Institute of Fundamental Research, Homi Bhabha Road, Colaba, Mumbai 400005, India

¹⁶School of Physics and Astronomy, University of Birmingham, Edgbaston, Birmingham B15 2TT, UK

¹⁷Anton Pannekoek Institute for Astronomy, University of Amsterdam, Science Park 904, 1098 XH Amsterdam, The Netherlands

ABSTRACT

Recent discoveries of transiting giant exoplanets ($R_p \gtrsim 8 R_\oplus$) around M dwarfs (GEMS) present an opportunity to investigate their atmospheric compositions and explore how such massive planets can form around low-mass stars contrary to canonical formation models. Here, we present the first transmission spectra of TOI-5205b, a short-period ($P = 1.63$ days) Jupiter-like planet ($M_p = 1.08 M_J$ and $R_p = 0.94 R_J$) orbiting an M4 dwarf. We obtained three transits using the PRISM mode of the JWST Near Infrared Spectrograph (NIRSpec) spanning $0.6 - 5.3 \mu\text{m}$. Our data reveal significant stellar contamination that is evident in the light curves as spot-crossing events and in the transmission spectra as a larger transit depth at bluer wavelengths. Atmospheric retrievals demonstrate that stellar contamination from unocculted star spots is the dominant component of the transmission spectrum at wavelengths $\lambda \lesssim 3.0 \mu\text{m}$, which reduced the sensitivity to the presence of clouds or hazes in our models. The degree of stellar contamination also prevented the definitive detection of any H_2O , which has primary absorption features at these shorter wavelengths. The broad wavelength coverage of NIRSpec PRISM enabled a robust detection of CH_4 and H_2S , which have detectable molecular features between $3.0 - 5.0 \mu\text{m}$. Our gridded and Bayesian retrievals consistently favored an atmosphere with both sub-solar metallicity ($\log [M/H] \sim -2$ for a clear atmosphere) and super-solar C/O ratio ($\log [C/O] \sim 3$ for a clear or cloudy atmosphere). This contrasts with estimates from planetary interior models that

Corresponding author: Caleb Cañas

c.canas@nasa.gov

predict a bulk metallicity of 10–20%, which is $\sim 100\times$ the atmospheric metallicity, and suggests that the planetary interior for TOI-5205b is decoupled from its atmosphere and not well mixed.

1. INTRODUCTION

Short-period ($P < 10$ days), Jupiter-mass planets were the first type of exoplanet discovered around main-sequence Sun-like stars (Mayor & Queloz 1995), but their formation process remains uncertain. The growing number of short-period Giant Exoplanets around M dwarf Stars (GEMS) presents additional complications to theories of gas giant formation (e.g., Kanodia et al. 2023; Delamer et al. 2024). GEMS are difficult to form through core accretion because the low disk masses and long orbital timescales for M dwarfs impede the efficient formation of massive planetary cores ($\sim 10 M_{\oplus}$) capable of initiating runaway gas accretion (e.g., Laughlin et al. 2004; Burn et al. 2021). These planets represent an extreme regime of planet formation for the lowest mass M dwarfs because the high planet-to-star mass ratios require core masses that exceed the estimated dust mass in the protoplanetary disk (e.g., Morales et al. 2019; Quirrenbach et al. 2022).

Understanding giant planet formation around all types of stars is crucial for explaining the architectures of exoplanetary systems. Studies both inside (Raymond et al. 2009; Brasser et al. 2016) and outside (Mulders et al. 2021) our Solar System show that the presence of gas giant planets affects the formation and evolution of smaller terrestrial planets. Close-in giant exoplanets have inspired multiple theories of planet formation and evolution (e.g., Dawson & Johnson 2018; Fortney et al. 2021), with the dominant origin channel suggesting that these planets form at large separations from their host star and subsequently migrate to their present-day observed location through various mechanisms (e.g., Rice et al. 2022; Jackson et al. 2022; Wu et al. 2023). Alternatively, they could have formed at their present-day location, (i.e., *in-situ*; Bodenheimer et al. 2000). The degeneracies among both migration and *in-situ* formation limit direct connections between the present-day observations of a giant planet and its primordial location in the disk (Mollière et al. 2022).

Studying the atmospheres of GEMS offers an opportunity to both characterize their chemical compositions and compare them with giant planets orbiting FGK stars. Any trends in the present-day atmospheric and bulk metallicities may provide insight into possible formation and evolution pathways, and thus a better understanding of giant planet formation processes for M

dwarfs. This is especially useful for the most massive GEMS, such as TOI-5205b, a Jupiter-like planet orbiting an M4 dwarf. Kanodia et al. (2023) used canonical disk mass ratio scaling laws to determine that there should be insufficient dust in the disk (estimated at $\sim 4 - 5 M_{\oplus}$) to initiate runaway gas accretion and form TOI-5205b.

In this work, we characterize the atmosphere of TOI-5205b using three transits obtained with JWST as part of our large Cycle 2 program (GO 3171) — *Red Dwarfs and the Seven Giants: First Insights Into the Atmospheres of Giant Exoplanets around M dwarf Stars* (Kanodia et al. 2023). In §2, we describe the design of this survey, followed by descriptions of the observations and data reduction in §3. We recovered the atmospheric properties from the spectra using two independent approaches: forward modeling (§4) and Bayesian retrievals (§5). In §6, we provide a new empirical measurement for the stellar metallicity of TOI-5205 and estimate the bulk metallicity of TOI-5205b in §7. We present our interpretation of the observed transmission spectra and discuss the implications for the formation of TOI-5205b in §8.

2. SURVEY DESIGN

Our GEMS JWST survey has two main components. First, we aim to measure atmospheric abundances of GEMS and directly compare them with the population of hot Jupiters orbiting FGK dwarfs and Solar System gas giants. Our goal is to explore whether the atmospheric mass-metallicity trends investigated by the community for planets around FGK dwarfs (e.g., Welbanks et al. 2019; Edwards et al. 2023) are applicable to the population of GEMS (§2.2). Second, we seek to perform the first study of bulk metallicities for GEMS to investigate whether there are any trends that may be a result of the formation processes involved (see §2.3).

2.1. Target selection

To select our sample of GEMS, we queried the NASA Exoplanet Archive (Akeson et al. 2013) along with then-recent publications (in January 2023) for transiting gas giant planets satisfying the following requirements: (i) $T_{\text{eff}} < 4000$ K, (ii) $R_p \gtrsim 8 R_{\oplus}$, (iii) a mass and radius precision $> 3\sigma$, and (iv) J mag > 11.5 to ensure no saturation in the NIRSpec PRISM mode. This search produced nine planets from which we excluded (i) HATS-74 Ab (Jordán et al. 2022) due to the presence

* NASA Postdoctoral Program Fellow

Table 1. Input Sample for the GEMS JWST survey (sorted by increasing planet mass)

Name	Pl. Mass	Pl. Radius	Period	Pl. T_{eq}	T_{eff}	St. Mass	J mag	References
	M_{\oplus}	R_{\oplus}	d	K	K	M_{\odot}		
TOI-3984 Ab	$44.00^{+8.70}_{-8.00}$	7.90 ± 0.24	4.3533	567	3476	0.49 ± 0.02	11.93 ± 0.02	Cañas et al. (2023)
TOI-3757b	$85.30^{+8.80}_{-8.70}$	$12.00^{+0.40}_{-0.50}$	3.4388	758	3913	0.64 ± 0.02	12.00 ± 0.03	Kanodia et al. (2022)
HATS-6b	101.39 ± 22.25	11.19 ± 0.21	3.3253	713	3724	$0.57^{+0.02}_{-0.03}$	12.05 ± 0.02	Hartman et al. (2015)
HATS-75b	156.05 ± 12.40	9.91 ± 0.15	2.7887	770	3790	0.60 ± 0.01	12.48 ± 0.02	Jordán et al. (2022)
TOI-5293 Ab	$170.40^{+21.80}_{-21.90}$	11.90 ± 0.40	2.9303	690	3586	0.54 ± 0.02	12.46 ± 0.03	Cañas et al. (2023)
TOI-3714b	222.48 ± 9.53	11.32 ± 0.34	2.1548	775	3660	0.53 ± 0.02	11.74 ± 0.02	Cañas et al. (2022)
TOI-5205b	$343.00^{+18.00}_{-17.00}$	$11.60 \pm 0.30^*$	1.6308	733	3430	0.39 ± 0.01	11.93 ± 0.03	Kanodia et al. (2023)

* - See refined parameters in Table 2, as well as Appendix B for discussion regarding the radius discrepancy for TOI-5205b.

of a bright nearby stellar companion ($\Delta J = 2.6$ mag at a separation of $0.844''$) and (ii) Kepler-45b (Johnson et al. 2012) as it was within 1σ in planetary mass of two other planets (HATS-75b and TOI-5293b) while having a much fainter host star ($J = 13.75 \pm 0.02$). This left our remaining sample of seven giant planets that spanned $T_{eq} = 570 - 850$ K with host spectral types M0 – M4 (see Table 1). We observed all seven planets using the JWST Near Infrared Spectrograph (NIRSpec) PRISM mode to obtain low-resolution spectra spanning $0.6 - 5.3 \mu\text{m}$ across 18 transits.

2.2. Mass - atmospheric metallicity trend

The atmospheric metallicity controls the efficiency of radiative cooling for a nascent gas giant planet and may impact the minimum core mass necessary to trigger runaway gas accretion, thus leading to predictions of a linear mass-metallicity trend (e.g., Ikoma et al. 2000; Movshovitz et al. 2010; Mordasini et al. 2014; Atreya et al. 2018). For the Solar System ice and gas giants, measurements of the atmospheric methane abundance demonstrate that these planets (i) are significantly enriched in heavy elements compared to the Sun and (ii) have decreasing enrichment with increasing planetary mass (e.g., Fortney et al. 2013; Movshovitz et al. 2010; Mordasini et al. 2014; Guillot & Gautier 2015). The metallicities of the Solar System ice and gas giants are inferred from their methane abundances because of their low equilibrium temperatures ($T_{eq} \lesssim 120$ K).

Measurements of atmospheric methane for hot Jupiters are difficult because the dominant carbon-bearing molecule is expected to be CO instead of methane due to their high temperatures ($T \gtrsim 1000$ K; Goukenleuque et al. 2000; Fortney et al. 2020). As such, the atmospheric metallicity of hot Jupiters are typically measured through their water abundance (e.g., Sing et al. 2016). GEMS have typical equilibrium tem-

peratures $T \lesssim 800$ K and are cooler than hot Jupiters, which increases the likelihood of detecting methane and water (Baxter et al. 2021). A key goal of our GEMS JWST survey is to compare our population of GEMS with both hot Jupiters (using water) and Solar System giant planets (with methane) to investigate the presence of trends between planetary mass and atmospheric metallicity (e.g., Welbanks et al. 2019; Pinhas et al. 2019; Sun et al. 2024).

2.3. Mass - bulk metallicity trend

In the core accretion theory of planet formation, the planetary mass is expected to be inversely proportional to the bulk metallicity, and may serve as a probe of the formation processes involved (e.g., Miller & Fortney 2011; Thorngren et al. 2016; Guillot et al. 2023; Swain et al. 2024). The bulk metallicity cannot be directly measured and therefore planetary evolution models are used to determine this value for non-inflated giant planets (e.g., Fortney et al. 2007; Thorngren et al. 2016). These estimates of bulk metallicity typically rely on various model assumptions (e.g., atmospheric composition, equations of state) that result in several possible solutions for a set of measured planetary parameters (e.g., Müller & Helled 2021). Measurements of the atmospheric metallicity reduce the reliance on theoretical models and can improve the accuracy of the inferred bulk composition (e.g., Thorngren & Fortney 2019; Müller & Helled 2021; Bloor et al. 2023; Acuña et al. 2024; Sing et al. 2024) and facilitate the study of any trends with planetary mass.

3. OBSERVATIONS AND DATA REDUCTION

We obtained three consecutive transits of TOI-5205b using the JWST NIRSpec PRISM in Bright Object Time Series (BOTS) mode (Birkmann et al. 2022; Espinoza et al. 2023) on 2023 October 10, October 11,

and October 13 (GO-3171; observation numbers 16, 17, and 18). The host star was used directly for target acquisition with the NRSRAPID readout pattern and the SUB32 array. All observations used the NRS1 detector with the SUB512 subarray (32×512 pixels) and consisted of 15784 integrations with 4 groups per integration, providing a median observational cadence of 1.15s. None of the observations saturated (i.e., the counts remained $< 80\%$ the saturation threshold of 2^{16} or 65,536 ADUs).¹ Each observation had at least a 1.5 hour pre-transit baseline and a 1 hour post-transit baseline.

We excluded the first 2070 data points from analysis in the second visit (observation 17) due to a large change in the trace position attributed to a “tilt event” (Perrin et al. 2024) where an abrupt change in the position of a mirror segment introduces a sudden jump in the time series. We reduced the observations with two pipelines designed for JWST exoplanet time-series observations: ExoTiC-JEDI (Alderson et al. 2022) and Eureka! (Bell et al. 2022). A detailed description of the reduction for each pipeline is presented in Appendix A.

For both the ExoTiC-JEDI and Eureka! data sets, we generated white and spectroscopic light curves at native resolution from our 1D spectra using Stage 4 of the Eureka! pipeline. The light curves were extracted for columns 30 – 491 ($\sim 0.520 - 5.579 \mu\text{m}$). The white light curves were generated by integrating over all wavelengths and both pipelines reveal a $\sim 6\%$ transit with spot-crossing events in each transit (see Figure 1). The recovered transit depth was shallower than the value derived with ground-based photometry from Kanodia et al. (2023) and we attributed this discrepancy to un-

corrected trends in the ground-based photometry due to the limited baseline and suboptimal observing conditions on those nights (see Appendix B for more details).

3.1. White light curve fits

We performed a white light curve fit only to the ExoTiC-JEDI reduction. We jointly fit all three white light curves using a modified version of `juliet` (Espinoza et al. 2019) that models spot crossing events. To mitigate the computational time, we binned the white light curves to a cadence of 5s. We did not use any limb darkening grids because of the limited coverage² at the host star’s effective temperature ($T_{\text{eff}} \sim 3430$ K, see a comparison of limb darkening coefficients in Appendix C) and, instead, adopted a quadratic limb darkening law following the parametrization presented in Kipping (2013). We modeled star spots using a semi-analytical model calculated with the `spotrod` package (see details on the spot model in Appendix D; Béky et al. 2014).

We placed priors on the orbit parameters and adopted a circular orbit based on results from Kanodia et al. (2023). We used a two-degree polynomial to model the trend known to exist in the NRS1 detector (e.g., Espinoza et al. 2023; Moran et al. 2023). We investigated various combinations of spot configurations by jointly fitting all white light curves with a varying number of spots (1 – 4) for each transit (see more details in Appendix D). We adopted the spot configuration of 4 spots in observation 16, 4 spots in observation 17, and 3 spots in observation 18. The derived parameters are presented in Table 2 while the spot parameters are listed in Appendix Table 7. The fit is presented in Figure 1.

Table 2. System parameters for TOI-5205

Name	Prior ^a	Value	Source
Stellar parameters:			
Stellar Mass (M_{\star})	...	0.394 ± 0.011	1
Stellar Radius (R_{\star})	...	0.392 ± 0.015	1
Effective Temperature (T_{eff})	...	3430 ± 54	1
Surface Gravity ($\log g_{\star}$)	...	4.84 ± 0.03	1
Metallicity ($[\text{Fe}/\text{H}]$)	...	0.56 ± 0.10	This work
Fitted transit parameters:			

Table 2 continued

¹ <https://jwst-docs.stsci.edu/jwst-near-infrared-spectrograph/nirspec-instrumentation/nirspec-detectors/nirspec-detector-performance>

² <https://zenodo.org/records/7874921>

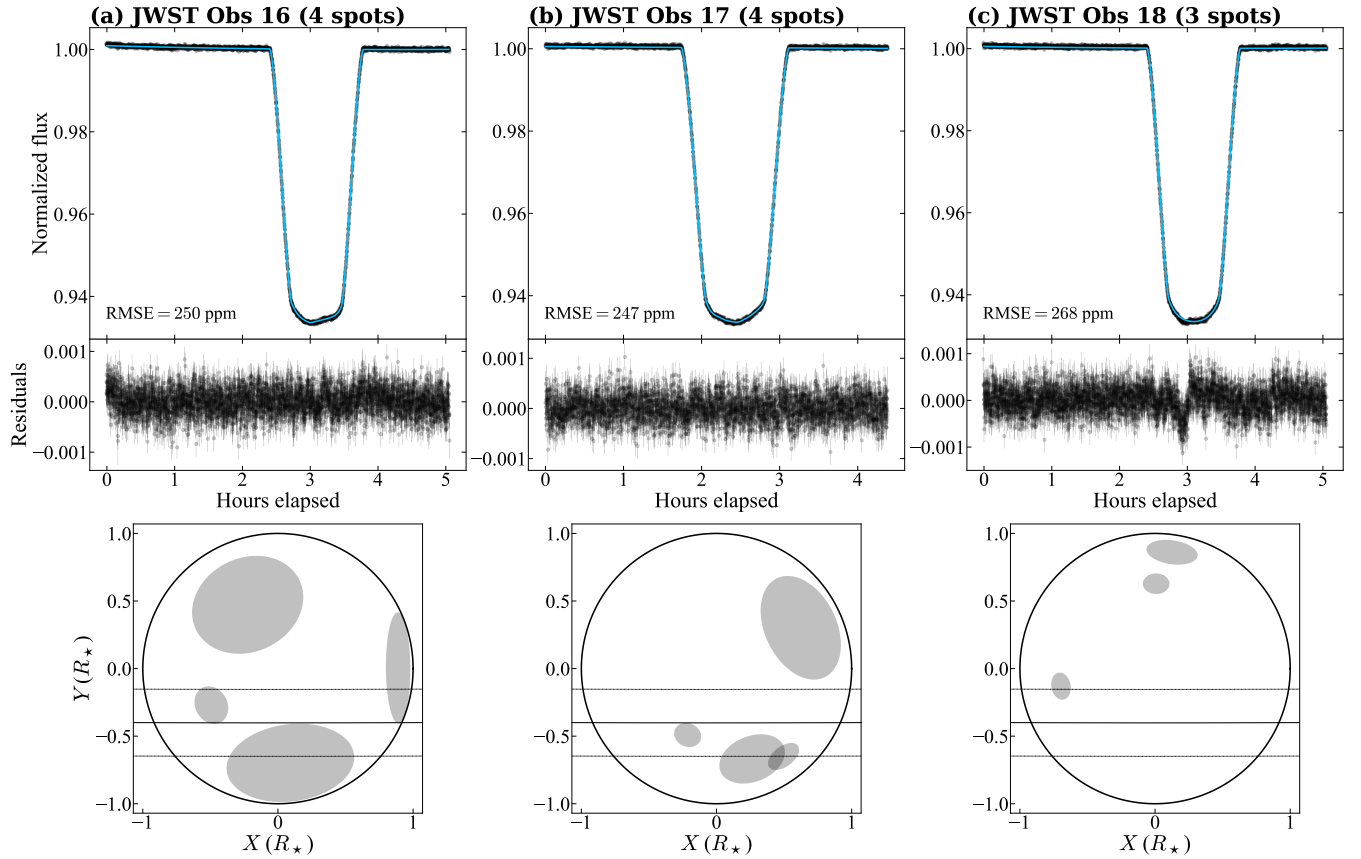


Figure 1. Panels (a)-(c) are the JWST NIRSpect PRISM white light curves produced using ExoTiC-JEDI, after binning to 5s for plotting purposes. The best-fitting model is indicated by the solid line with residuals to the fit indicated in the middle row. The bottom row displays the 2D projection of the stellar surface and the adopted spot configuration from the white light curve fit.

Table 2 (*continued*)

Name	Prior ^a	Value	Source
Period (P)	$\mathcal{N}(1.63, 0.01)$	1.630731 ± 0.000003	This work
Time of mid-transit (T_0)	$\mathcal{N}(2460227.86, 0.01)$	$2460227.864967 \pm 0.000004$	This work
Eccentricity (e)	Fixed	0	This work
Argument of periastron (ω)	Fixed	90	This work
Scaled radius (R_p/R_*)	$\mathcal{U}(0, 1)$	$0.2475^{+0.0003}_{-0.0002}$	This work
Scaled semi-major axis (a/R_*)	$\mathcal{N}(10.94, 0.22)$	$10.695^{+0.006}_{-0.005}$	This work
Impact parameter (b)	$\mathcal{U}(0, 1)$	0.402 ± 0.001	This work
Derived system parameters:			
Inclination (i)	...	$87.847^{+0.007}_{-0.006}$	This work
Semi-major axis (a)	...	0.0195 ± 0.0007	This work
Planet Radius (R_p)	...	0.94 ± 0.04	This work
Planet Mass (M_p)	...	1.08 ± 0.06	1
Equilibrium temperature (T_{eq})	...	742 ± 12	This work
Spot temperature ^b (T_{spot})	...	3350 ± 50	This work

Table 2 *continued*

Table 2 (continued)

Name	Prior ^a	Value	Source
------	--------------------	-------	--------

References—1) Kanodia et al. (2023)

^aNormal priors with a mean of X and standard deviation of Y are denoted as $\mathcal{N}(X, Y)$.

Uniform priors between a lower limit of X and upper limit of Y are denoted as $U(X, Y)$.

^bThe spot temperature was derived using the spot flux ratio, the NIRSpec/PRISM throughput, obtained with the ExoTiC-LD package, and model spectra from the PHOENIX stellar library (Husser et al. 2013) accessed via pysynphot (STScI Development Team 2013).

3.2. Transmission spectra

To derive the transmission spectra, we modeled the spectroscopic light curves of both reductions using stage 5 of the Eureka! pipeline modified to include spot modeling with `spotrod` (see Appendix D for a detailed description). The resulting spectra for both the ExoTiC-JEDI and Eureka! reductions are presented in Figure 2. Both reductions (and all three transits) showed an increase in the transit depth towards bluer wavelengths, which we attributed to the effect of stellar contamination by unocculted spots (the transit light source or TLS effect; e.g., Rackham et al. 2017). At the pixel level, the differences between the two pipelines were minimal and most of the data showed differences $< 1\sigma$. The largest region of scatter occurred between $1 - 2 \mu\text{m}$ and was most likely due to differences in the spectral extraction. Given the similarities between the spectra, we utilized the ExoTiC-JEDI reduction for all subsequent analysis in this work.

4. ATMOSPHERIC FORWARD MODELING

4.1. Chemical equilibrium atmospheric modeling with PICASO

We used the open-source modeling package PICASO (v3.2.2; Batalha et al. 2019; Mukherjee et al. 2023) to investigate how the transmission spectrum compared to models for a gas giant in chemical equilibrium. We computed radiative-convective thermochemical equilibrium (RCTE) atmospheric models for TOI-5205b using the one-dimensional climate code from PICASO. We adopted the Guillot (2010) pressure-temperature profile approximation as the initial guess for the climate model. PICASO uses the publicly available correlated-k opacities (see Lupu et al. 2023) from the Sonora Bobcat models of brown dwarfs and gas giants (Marley et al. 2021). The model atmospheres were created on a grid that spanned (i) 13 metallicities ($[M/H] = -1.0, -0.7, -0.5, -0.3, 0.0, 0.3, 0.5, 0.7, 1.0, 1.3, 1.5, 1.7, 2.0 \text{ dex}$), (ii) 6 carbon-to-oxygen ratios ($C/O = 0.25, 0.5, 1.0, 1.5, 2.0, 2.5$),

(iii) 5 intrinsic temperatures ($T_{\text{int}} = 100, 200, 300, 400, 500 \text{ K}$), and (iv) 3 heat redistribution factors³ ($r_{st} = 0.25, 0.50, 0.75$), resulting in 1130 models. The model transmission spectra were computed from the climate models with PICASO using an opacity database that was resampled to $R = 60,000$ (Batalha et al. 2022) from the original $R \sim 10^6$ line-by-line calculations presented in Freedman et al. (2008) and EXOPLINES (Gharib-Nezhad et al. 2021). There were a total of 1170 model transmission spectra representing the different combinations of grid parameters.

For TOI-5205b, clear spot-crossing events are observed in all JWST observations and, given the rapid evolution of the occulted spots, we also expected the presence of unocculted spots. Due to the observed contamination in the transmission spectra by the TLS effect, we adopted a few configurations for a spot-contaminated stellar photosphere by post-processing the spectral output of PICASO. The disk-integrated spectral energy distribution (SED) of the host star was calculated as a weighted combination of two components: (i) a spotted region that was modeled using a PHOENIX spectrum (Husser et al. 2013) that adopted a cooler temperature but identical surface gravity and metallicity to the host star with a spot coverage fraction of f_{spot} and (ii) a quiet photosphere that was modeled using a PHOENIX spectrum that matched the known parameters of the host star (see Table 2) with a weight of $1 - f_{\text{spot}}$. We followed the methodology of Rackham et al. (2018) to determine the contamination spectrum⁴ for two different spot temperatures ($T_{\text{spot}} = 3230 \text{ or } 3330 \text{ K}$) and a range of spot coverage fractions ($f_{\text{spot}} = 0.01, 0.05, 0.1, 0.2, 0.3$). Adding these additional parameters to account for the TLS ef-

³ The fractional contribution of the stellar radiation to the net flux per atmospheric layer, see Equation 20 in Mukherjee et al. (2023). A value of $r_{st} = 0.5$ corresponds to efficient day-night energy redistribution.

⁴ $\epsilon_{\lambda, \text{het}}$ in Equation 2 of Rackham et al. (2018), or the multiplicative factor that is a function of wavelength and represents the ratio of the homogeneous stellar SED to the contaminated SED.

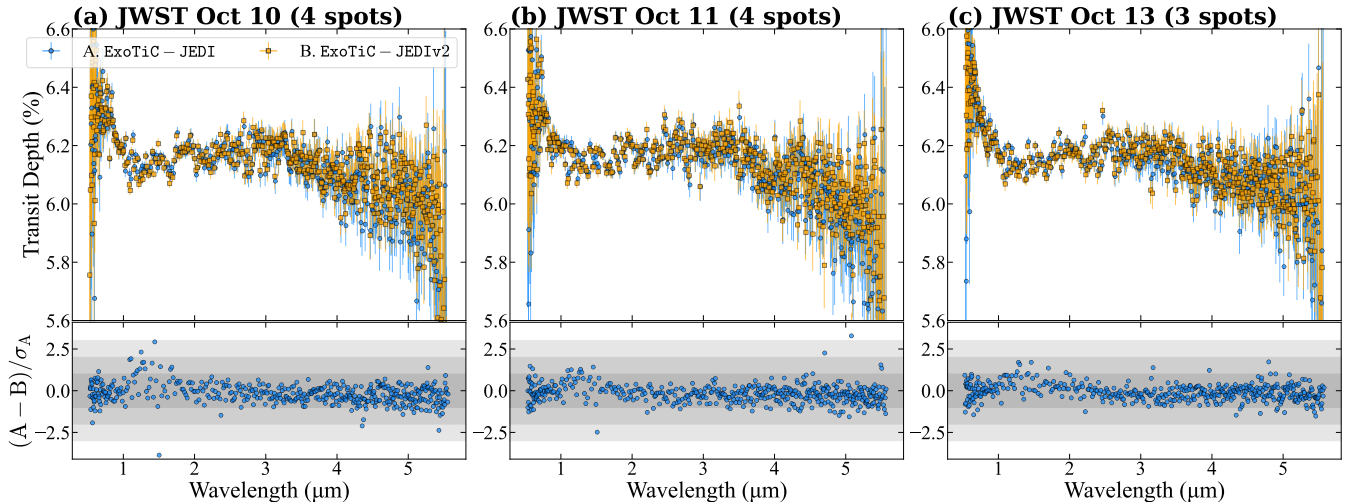


Figure 2. TOI-5205b transmission spectra (top row) and differences (bottom row). In each top panel, the ExoTiC-JEDI reductions are denoted as blue circles and the **Eureka!** reductions are plotted as orange squares. The differences, scaled by the errors of the data, are presented in the bottom row. The 1, 2, and 3σ regions are shaded in the bottom panel. The transmission spectra for both pipelines and all visits are included as data behind the figure.

fect resulted in 11700 unique model spectra. We do not consider a grid with both spots and faculae in part due to the large grid size resulting for only one heterogeneity alone (spots) on the stellar surface. We ultimately only considered spots because the shape of the features observed in the region $< 1 \mu\text{m}$ indicates increasing transit depths towards bluer wavelengths, which is inconsistent with faculae (see Rackham et al. 2018).

We fit the grids to the co-added (derived using a weighted average) ExoTiC-JEDI spectrum using the χ^2_ν grid search method implemented in PICASO. The RCTE models which do not include the TLS effect were highly discrepant from the observed spectrum ($\chi^2_\nu > 14$), but the models including the TLS effect were able to fit the observations with a $\chi^2_\nu \sim 2.6$ (see Figure 3). The best-fitting model from the RCTE grid that included the TLS effect had $[\text{M}/\text{H}] = -1.0$ dex, $\text{C}/\text{O} = 1.0$, $T_{\text{int}} = 300$ K, $r_{\text{st}} = 0.25$, $T_{\text{spot}} = 3330$ K and $f_{\text{spot}} = 0.3$. This fit reached the lower limit of the metallicities from the PICASO grid and therefore did not exclude an even lower atmospheric metallicity for TOI-5205b. Although the χ^2_ν (see Table 3) improved by an order of magnitude when accounting for the TLS effect, the RCTE models still displayed residuals $> 3\sigma$ in the region $< 3.5 \mu\text{m}$. This suggests that limitations in the assumption of chemical equilibrium or the adopted spot configuration may impact the recovered atmospheric parameters.

4.2. Investigating disequilibrium processes with VULCAN

To investigate the atmospheric composition when incorporating disequilibrium processes, we employed the

photochemical model VULCAN (Tsai et al. 2017, 2021) with the temperature profiles computed by PICASO as input. These temperature profiles remained fixed without performing iteration to account for the radiative feedback of the disequilibrium abundances. The initial composition was determined by the equilibrium abundance for the given elemental abundances, calculated by FastChem (Stock et al. 2018) and incorporated in VULCAN. We used the most recent S-N-C-H-O photochemical network⁵ for these calculations. TOI-5205 is an M4 dwarf with an effective temperature of 3430 K and we adopted the UV spectrum of GJ 436 (M3; France et al. 2016; Youngblood et al. 2016; Loyd et al. 2016) as an analogue for the stellar UV spectrum. We explored the same atmospheric parameter space as the RCTE models.

As the best-fitting RCTE models reached the lower limit of the PICASO metallicity grid, we extended the grid to lower metallicities using VULCAN to investigate potential biases in atmospheric parameters due to grid limits. We did not calculate new pressure-temperature profiles for the lower metallicity models, but instead adopted the pressure-temperature profile from the nearest model in the RCTE grid. In addition, motivated by the strong detection of H_2S (see §8.2), we explored a range of sulfur elemental abundances that deviated from the solar elemental ratio. Specifically, we (i) used two different strengths of vertical mixing ($K_{zz} = 10^6$ and $10^9 \text{ cm}^{-2} \text{ s}^{-1}$), (ii) expanded the grid to lower metallicities down

⁵ https://github.com/exoclimate/VULCAN/blob/master/thermo/SNCHO_photo_network_2024.txt

Table 3. Parameters for the best-fitting models derived from PICASO and VULCAN. Parameters that were not used for a specific model are empty.

Parameter	Units	PICASO (RCTE)		VULCAN (Disequilibrium Chemistry)					
Atmospheric metallicity ([M/H])	dex	0.0	-1.0	-2.0	-2.0	-2.0	-2.0	-1.7	-2.0
Atmospheric carbon-to-oxygen ratio (C/O)	dex	2.5	1.0	1.0	1.0	0.5	1.0	0.25	0.5
Intrinsic Temperature (T_{int})	K	100	300	200	200	100	200	100	100
Heat redistribution factor (r_{st})	...	0.20	0.2	0.5	0.5	0.5	0.5	0.5	0.5
Spot coverage fraction (f_{spot})	0.3	0.3	0.3	0.3	0.3	0.3	0.3
Spot temperature (T_{spot})	K	...	3330	3330	3330	3330	3330	3330	3330
Eddy diffusive coefficient (K_{zz})	dex	6	6	6	9	9	9
Sulfur abundance (S/H)	1	10	100	1	10	100
Reduced chi-squared (χ^2_{ν})	...	14.714	2.635	2.626	2.611	2.565	2.626	2.610	2.558

to $[M/H] = -2.0$, and (iii) included different sulfur enhancements ($f_S = 1, 10, 100$), where f_S is the sulfur enhancement factor relative to the solar value from [Asplund et al. \(2021\)](#). For reference, the adopted solar elemental abundances are $[C/H] = -3.54$, $[O/H] = -3.31$, and $[S/H] = -4.88$.

Similar to the PICASO modeling in §4.1, we post-processed the spectra to account for stellar contamination (with identical spot parameters) and fit the grid to the data using the same χ^2_{ν} method. We did not consider VULCAN models without the TLS effect given the results from the RCTE grid. The modeling results are summarized in [Figure 3](#) and [Table 3](#). The models derived using VULCAN were better fits when compared to the RCTE models ($\chi^2_{\nu} = 2.635$ for RCTE compared to $\chi^2_{\nu} = 2.565$ for the models processed with VULCAN). K_{zz} was unconstrained as there was a minimal difference in χ^2_{ν} between the two values, while the highest sulfur enhancement appeared to be slightly favored. The best fitting model that accounted for disequilibrium processes had $[M/H] = -2.0$ dex, $C/O = 0.5$, $T_{\text{int}} = 100$ K, $r_{st} = 0.5$, $T_{\text{spot}} = 3330$ K, $f_{\text{spot}} = 0.3$, $K_{zz} = 10^9$ cm⁻² s⁻¹, and $S/H = 100$. The recovered atmospheric metallicity appeared to favor a lower limit imposed by the chemistry grids used by VULCAN and PICASO. Qualitatively, the RCTE and VULCAN grids both suggested that the planetary atmosphere was potentially metal-poor.

5. ATMOSPHERIC RETRIEVALS

To aid interpretation of the transmission spectrum beyond grid-based models, we investigated the atmospheric properties of TOI-5205b by performing Bayesian atmospheric retrievals (e.g., [Madhusudhan 2018](#)) assuming both chemical equilibrium and free chemistry.

5.1. Equilibrium Chemistry Retrievals

5.1.1. PLATON Analysis

We performed retrievals on the co-added spectrum, assuming chemical equilibrium, using the PLanetary Atmospheric Tool for Observer Noobs modeling package (PLATON v6.1; [Zhang et al. 2019, 2020](#)).⁶ PLATON allows for modeling of the TLS effect assuming one type of stellar heterogeneity (e.g., either spots or faculae, but not both). The dilution due to unocculted star spots was modeled following [Rackham et al. \(2018\)](#) and, similar to our PICASO implementation (see §4.1), was parameterized with a spot coverage fraction and spot temperature. PLATON computed chemical equilibrium abundances using [FastChem](#) with a grid that spanned a range of $-2 \leq \log[M/H] \leq 3$ and $0.001 \leq C/O \leq 2$. We adopted an isothermal pressure-temperature profile for this fit. The default PLATON opacity database has a resolution of $R = 20,000$. We sampled the parameter space using the dynamic nested sampler [dynesty](#) with $N = 5000$ live points and a convergence criterion of $\Delta \log Z = 0.5$.

5.1.2. POSEIDON Analysis

We also performed retrievals on the co-added spectrum, assuming chemical equilibrium, using the POSEIDON code ([MacDonald & Madhusudhan 2017; MacDonald 2023](#)). POSEIDON also uses [FastChem](#) to compute equilibrium chemical abundances that spans a range of $-1 \leq \log[M/H] \leq 4$ and $0.2 \leq C/O \leq 2$. We adopted an isothermal pressure-temperature profile for these models. We performed the radiative transfer calculations on an intermediate resolution spectral grid set to $R = 20,000$ from $0.5 - 5.3$ μm . POSEIDON retrievals also included a stellar contamination model (albeit with both spots and faculae) to account for the TLS effect.

⁶ <https://github.com/ideasrule/platon>

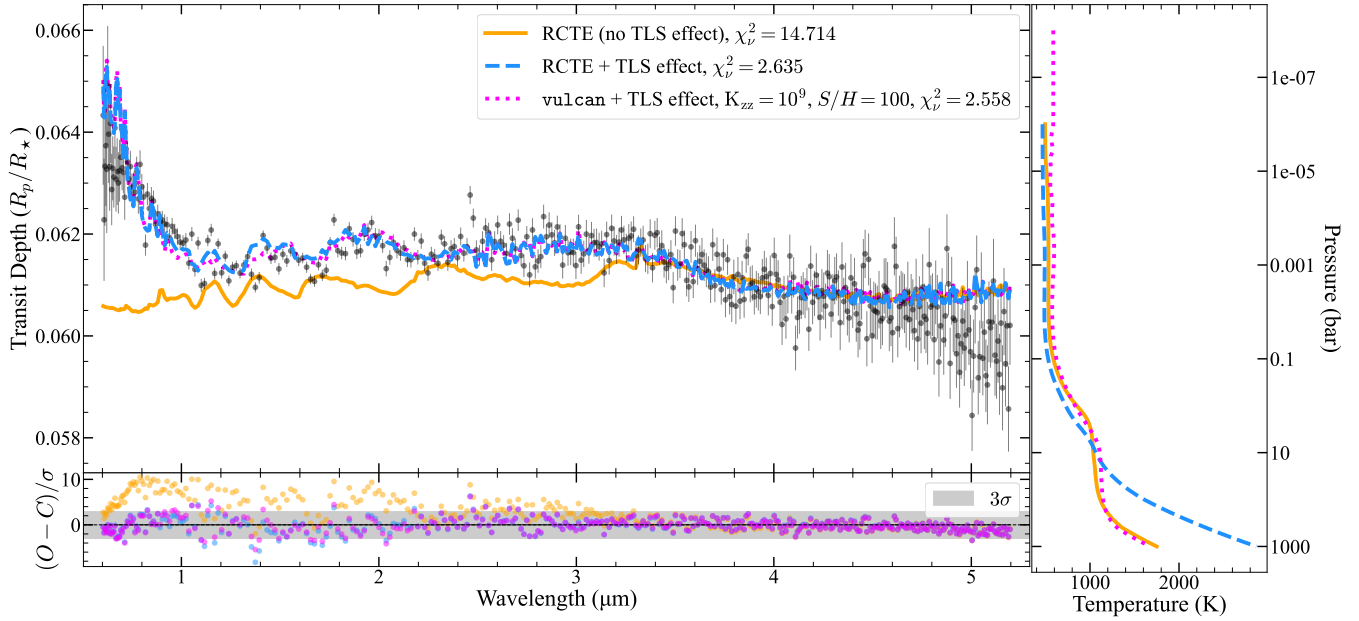


Figure 3. Top left panel: The co-added TOI-5205b ExoTiC-JEDI transmission spectrum along with the best-fitting grid-based models assuming chemical equilibrium (obtained from PICASO) or chemical disequilibrium (obtained via VULCAN). Bottom row: The difference, scaled by the errors of the data to each model. The $\pm 3\sigma$ region is shaded in the bottom panel. Right: The pressure-temperature profile for each model. The co-added spectrum, at native resolution, is available as data behind the figure.

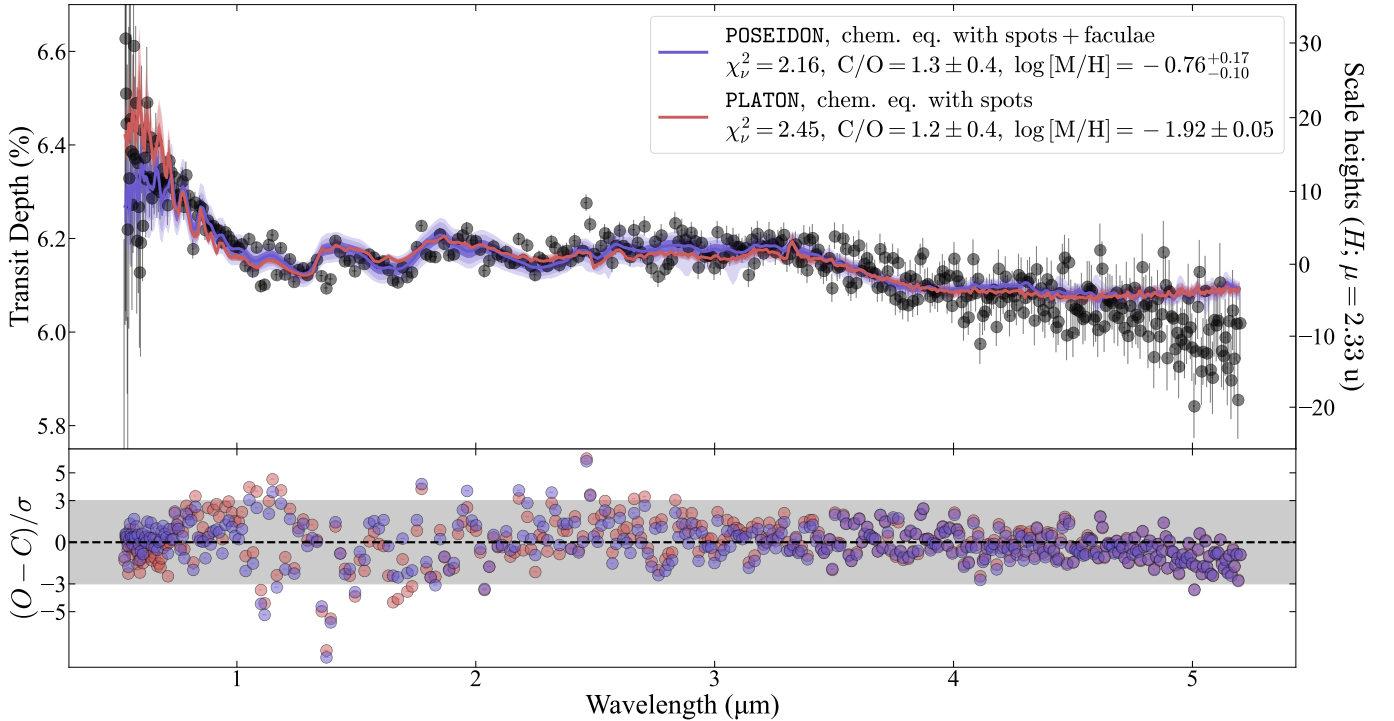


Figure 4. A comparison of retrievals, assuming chemical equilibrium, with the co-added ExoTiC-JEDI spectrum of TOI-5205b using POSEIDON (assuming both spots and faculae) and PLATON (assuming only spots). The top panel presents the co-added spectra (as black circles) with the best fitting models and their respective $1 - 3\sigma$ posteriors. Both retrieval codes approach the lower limit of the grid in metallicity but agree on the retrieved C/O ratio. The bottom panel presents the residuals to the best-fitting solution for each code.

Our fiducial stellar contamination model included three components: a quiescent photosphere, a cooler region

due to spots, and a hotter region due to faculae. For each component, we fit for an effective temperature (T) and a

Table 4. Model parameters for retrievals assuming equilibrium chemistry. Parameters that were not used for a specific model are empty.

Parameter	Units	PLATON, $\chi^2_\nu = 2.45$		POSEIDON, $\chi^2_\nu = 2.16$	
		Prior ^a	Value	Prior	Value
Stellar radius (R_*)	R_\odot	$\mathcal{N}(0.392, 0.015)$	0.396 ± 0.005
Planetary mass (M_p)	M_J	$\mathcal{N}(1.08, 0.06)$	$1.11^{+0.05}_{-0.07}$
Planetary radius (R_p)	R_J	$\mathcal{N}(0.94, 0.04)$	0.94 ± 0.01	$\mathcal{U}(0.80, 1.08)$	0.9335 ± 0.0006
Equilibrium temperature (T_{eq})	K	$\mathcal{U}(371, 1484)$	543^{+138}_{-81}	$\mathcal{U}(300, 1500)$	360 ± 30
Atmospheric metallicity ($[M/H]$)	dex	$\mathcal{U}(-2, 3)$	$-1.92^{+0.11}_{-0.05}$	$\mathcal{U}(-0.9, 3.9)$	$-0.76^{+0.17}_{-0.10}$
Atmospheric carbon-to-oxygen ratio (C/O)	dex	$\mathcal{U}(-3, 2)$	$1.2^{+0.5}_{-0.4}$	$\mathcal{U}(0.3, 1.9)$	1.3 ± 0.4
Spot coverage fraction (f_{spot})	...	$\mathcal{U}(0, 1)$	$0.2^{+0.6}_{-0.1}$	$\mathcal{U}(0, 1)$	$0.31^{+0.06}_{-0.04}$
Spot temperature (T_{spot})	K	$\mathcal{U}(2930, 3430)$	3300^{+100}_{-300}	$\mathcal{U}(2300, 3430)$	3400 ± 20
Spot surface gravity ($\log g_{\text{spot}}$)	dex	$\mathcal{U}(4.34, 5.34)$	$4.48^{+0.08}_{-0.07}$
Faculae coverage fraction (f_{fac})	$\mathcal{U}(0, 0.5)$	$0.027^{+0.008}_{-0.006}$
Faculae temperature (T_{fac})	K	$\mathcal{U}(3430, 4802)$	4228^{+107}_{-84}
Faculae surface gravity ($\log g_{\text{fac}}$)	dex	$\mathcal{U}(4.34, 5.34)$	$4.42^{+0.10}_{-0.06}$
Photosphere temperature (T_{eff})	K	Fixed	3430	$\mathcal{N}(3430, 54)$	3590 ± 20
Photosphere surface gravity ($\log g_{\text{fac}}$)	dex	Fixed	4.84	$\mathcal{U}(4.34, 5.34)$	4.64 ± 0.07
Error multiplicative factor	...	$\mathcal{U}(0.5, 5)$	$1.57^{+0.05}_{-0.06}$

^aNormal priors with a mean of X and standard deviation of Y are denoted as $\mathcal{N}(X, Y)$.

Uniform priors between a lower limit of X and an upper limit of Y are denoted as $\mathcal{U}(X, Y)$.

surface gravity ($\log g$). For spots and faculae, we fit for the fractional area (f_{spot} and f_{fac}) covered by each component and assume that the remaining fractional stellar area ($1 - f_{\text{spot}} - f_{\text{fac}}$) is the quiescent photosphere.

We used the nested sampling Bayesian parameter estimation code `MultiNest` (Feroz et al. 2009), which is accessed within `POSEIDON` via the `PyMultiNest` Python wrapper (Buchner et al. 2014). Our retrievals used 400 live points to sample parameter space with a convergence criterion of $\Delta \ln Z = 5$. A summary of the priors and retrieved parameters derived with both `PLATON` and `POSEIDON` are listed in Table 4 and the results are shown in Figure 4. The `POSEIDON` pipeline provides a better fit to the data when compared to `PLATON` because of the additional flexibility in the TLS effect model that considers multiple heterogeneities with different temperatures and surface gravities from the host star. Both atmospheric retrieval codes recover a consistent atmospheric C/O $\sim 1.2 - 1.3$, however, the atmospheric metallicities consistently approach the edge of the respective grid ($[M/H] \rightarrow -1$ dex for `POSEIDON` and $[M/H] \rightarrow -2$ dex for `PLATON`). Both of these retrievals provided a better fit than our grid results (lower χ^2_ν) but were still qualitatively similar in that both the retrievals and grid fits favored a sub-solar atmospheric metallicity and a super-solar atmospheric C/O ratio.

5.2. Free Chemistry Retrievals

We used `POSEIDON` to investigate the atmospheric properties of TOI-5205b with retrievals allowing for freely varying individual chemical abundances to test for non-equilibrium chemical abundances. We performed this investigation on the co-added transmission spectrum. Similar to the `POSEIDON` retrievals assuming chemical equilibrium (§5.1.2), we used opacities sampled to $R = 20,000$. We included opacities for the following species: H_2O , CH_4 , CO_2 , CO , SO_2 , and H_2S , as well as collision-induced absorption (CIA) from $\text{H}_2\text{-H}_2$, $\text{H}_2\text{-He}$, $\text{H}_2\text{-CH}_4$, $\text{CO}_2\text{-H}_2$, $\text{CO}_2\text{-CO}_2$, and $\text{CO}_2\text{-CH}_4$. Our use of “free chemistry” indicates that the logarithmic mixing ratio of each molecule is included as a free parameter, assuming evenly mixed vertical gas abundances, except for H_2 and He which are assumed to constitute the bulk composition of the atmosphere and are fractionated according to their relative cosmochemical abundances ($N_{\text{He}}/N_{\text{H}_2} = 0.17$).

Our baseline model included 17 free parameters to describe the planet and heterogeneous star (with both spots and faculae), but we investigated sets of nested models with larger and smaller parameter volumes to identify the most critical model components for fitting the co-added spectrum of TOI-5205b. A summary of the free parameters used in our retrievals and their associated priors is provided in the first two columns of Table 5.

Table 5. Atmospheric retrieval priors and posteriors for the M3.1 model without clouds. The abundances are the volume mixing ratios for each species.

Parameters	Priors	Visit 1	Visit 2	Visit 3	Visits co-added
$R_{p, \text{ref}}$	$\mathcal{U}(0.88, 1.19)$	$0.9242^{+0.0020}_{-0.0018}$	$0.9259^{+0.0021}_{-0.0021}$	$0.9343^{+0.0016}_{-0.0021}$	$0.9278^{+0.0012}_{-0.0012}$
T	$\mathcal{U}(200.00, 1500.00)$	874^{+123}_{-59}	850^{+108}_{-47}	769^{+77}_{-110}	795^{+45}_{-65}
$\log \text{CH}_4$	$\mathcal{U}(-12.00, -1.00)$	$-5.39^{+0.25}_{-0.26}$	$-5.20^{+0.26}_{-0.27}$	$-6.27^{+0.28}_{-0.25}$	$-5.53^{+0.19}_{-0.16}$
$\log \text{H}_2\text{O}$	$\mathcal{U}(-12.00, -1.00)$	$-9.5^{+1.7}_{-1.4}$	$-9.5^{+1.6}_{-1.6}$	$-9.6^{+1.6}_{-1.3}$	$-9.7^{+1.3}_{-1.5}$
$\log \text{H}_2\text{S}$	$\mathcal{U}(-12.00, -1.00)$	$-4.51^{+0.37}_{-0.45}$	$-3.86^{+0.34}_{-0.31}$	$-5.5^{+0.8}_{-2.9}$	$-4.32^{+0.21}_{-0.22}$
$\log \text{CO}_2$	$\mathcal{U}(-12.00, -1.00)$	$-10.4^{+1.1}_{-1.1}$	$-9.5^{+1.5}_{-1.7}$	$-10.4^{+1.1}_{-1.0}$	$-10.42^{+1.01}_{-0.98}$
$\log \text{CO}$	$\mathcal{U}(-12.00, -1.00)$	$-9.6^{+1.6}_{-1.6}$	$-9.7^{+1.7}_{-1.4}$	$-9.6^{+1.4}_{-1.5}$	$-10.1^{+1.3}_{-1.1}$
$\log \text{SO}_2$	$\mathcal{U}(-12.00, -1.00)$	$-9.4^{+1.9}_{-1.6}$	$-9.4^{+1.9}_{-1.7}$	$-9.3^{+1.7}_{-1.7}$	$-9.5^{+1.7}_{-1.5}$
f_{spot}	$\mathcal{U}(0.00, 1.00)$	$0.112^{+0.021}_{-0.022}$	$0.123^{+0.025}_{-0.021}$	$0.134^{+0.095}_{-0.035}$	$0.132^{+0.015}_{-0.013}$
f_{fac}	$\mathcal{U}(0.00, 0.50)$	$0.0068^{+0.0082}_{-0.0029}$	$0.0176^{+0.0120}_{-0.0079}$	$0.021^{+0.034}_{-0.013}$	$0.0146^{+0.0053}_{-0.0040}$
T_{spot}	$\mathcal{U}(2300.00, 3430.00)$	2888^{+89}_{-108}	3013^{+104}_{-102}	3250^{+117}_{-119}	3156^{+45}_{-56}
T_{fac}	$\mathcal{U}(3430.00, 4802.00)$	4298^{+285}_{-600}	4054^{+178}_{-218}	3679^{+194}_{-132}	4263^{+132}_{-125}
T_{phot}	$\mathcal{N}(3430.00, 54.00)$	3464^{+58}_{-45}	3548^{+42}_{-48}	3524^{+39}_{-46}	3640^{+26}_{-34}
$\log g_{\text{spot}}$	$\mathcal{U}(4.34, 5.34)$	$4.64^{+0.14}_{-0.15}$	$4.58^{+0.16}_{-0.15}$	$4.46^{+0.13}_{-0.08}$	$4.432^{+0.096}_{-0.063}$
$\log g_{\text{fac}}$	$\mathcal{U}(4.34, 5.34)$	$4.73^{+0.35}_{-0.25}$	$4.55^{+0.26}_{-0.14}$	$4.88^{+0.29}_{-0.33}$	$4.51^{+0.19}_{-0.12}$
$\log g_{\text{phot}}$	$\mathcal{U}(4.34, 5.34)$	$5.05^{+0.17}_{-0.20}$	$5.04^{+0.16}_{-0.17}$	$4.95^{+0.23}_{-0.25}$	$5.06^{+0.14}_{-0.14}$
χ^2_ν	—	1.51	1.25	1.12	2.04
$\ln Z$	—	2373.35	2378.37	2453.69	2469.29

Table 6. Atmospheric retrieval models & model selection results

Name	Model Description	χ^2_ν	$\ln Z$	$\ln B_{3,2}$	Rejected
M1.1	TLS only (1 spot)	2.75	2331.87	141.19	17.0σ
M1.2	TLS (1 spot, free $\log(g)$)	2.68	2342.77	130.29	16.3σ
M1.3	TLS (2 spots)	2.51	2373.13	99.93	14.3σ
M1.4	TLS (2 spots, free $\log(g)$)	2.39	2399.11	73.95	12.3σ
M2.1	Atm only	4.94	1893.40	579.66	$> 30\sigma$
M2.2	Atm + Cloud	4.95	1892.48	580.58	$> 30\sigma$
M2.3	Atm + Haze	4.97	1893.42	579.64	$> 30\sigma$
M2.4	Atm + Cloud + Haze	3.06	2269.37	203.69	20.3σ
M3.1	TLS + Atm	2.04	2469.29	3.77	3.2σ
M3.2	TLS + Atm + Cloud	2.04	2473.06	0.00	—
M3.3	TLS + Atm + Haze	2.06	2469.93	3.13	3.0σ
M3.4	TLS + Atm + Cloud + Haze	2.04	2471.83	1.23	2.2σ

NOTE—The $\ln B$ and $\ln Z$ columns report results for the co-added ExoTiC-JEDI transmission spectrum with the “4-4-3” spot configuration. Nominally, “Atm” refers to a H_2/He atmosphere with H_2O , CH_4 , CO_2 , CO , SO_2 , and H_2S . The Bayes factors listed for each case are with respect to M3.2.

5.2.1. Model comparison and selection

Our retrievals considered (i) stellar contamination from the TLS effect, (ii) atmospheric absorption due to gas opacity, and (iii) absorption and scattering due to an opaque cloud-deck and hazes (using the generalized cloud and haze prescription in [MacDonald & Madhusudhan 2017](#)). We constructed sets of nested models that contained different combinations of the modeling components with their respective free parameters, and quantified the goodness of fit (χ^2_ν) and Bayesian evidence ($\ln Z$). The Bayes Factor (B ; [Trotta 2008](#)), derived from the likelihood (Z) of different models, allowed models to be statistically compared and certain models to be rejected. Detailed analyses of the individual visits are presented in §5.2.2. [Table 6](#) lists the retrieval models that we considered in our initial transmission spectrum analysis and the statistical results of the model comparison.

Our model complexity investigation demonstrates that both stellar contamination and the planetary atmosphere are detected at high confidence ($>20\sigma$ and $>12\sigma$, respectively), while evidence for or against clouds and hazes is minimal ($\sim 3\sigma$). [Table 6](#) shows that the preferred model includes the TLS effect, a planetary atmo-

sphere, and cloud model components (M3.2 in [Table 6](#)). By comparison, retrievals without TLS contamination (M2 series) are very discrepant with the co-added spectrum and are rejected at $>20\sigma$ (i.e., strong detection of TLS). The model with both clouds and hazes (M2.4) is the best model among those without TLS contamination because the hazes produce a slope at short wavelengths,

which is similar but not identical to the contamination from cool spots. Our retrievals with only TLS contamination and no planetary atmosphere (M1 series) are comparatively poor fits to the data and are rejected at $\geq 12\sigma$ (i.e., strong detection of the atmosphere). The most complex TLS model (M1.4), with two heterogeneous components and free surface gravity for the photosphere, spot, and faculae components, is strongly preferred over the simpler TLS models (e.g. M1.4 preferred over M1.3 at $\geq 7.5\sigma$). For the models including both the TLS effect and atmospheres (M3 series), all cases build upon the M1.4 TLS model. In these cases, we find that including clouds in the model improves the Bayesian evidence over the cloud-free case, but incorporating a haze component decreases the evidence and is therefore marginally rejected. However, all models that include the TLS effect and atmosphere provide equally good fits to the data, as evidenced by their consistent χ^2_{ν} values.

5.2.2. Atmospheric retrievals on individual visits

Given the varying structure in each visit spectrum (see Figure 2), we performed retrievals on the individual visits to assess the consistency. We build on the insights from the previous sections and run retrievals using the M3.1 (TLS + Atm) and M3.2 (TLS + Atm + Cloud) model configurations.

Fig Set 5.1 compares the posterior distributions obtained by separately fitting the three visits and the co-added transmission spectrum using retrievals with and without clouds. Figures showing individual results with marginalized 1D posterior constraints labeled are provided as Fig Set 5 in the online journal. For quantitative comparison, Table 8 and Table 5 provide the 1σ retrieval constraints for cloudy and cloud-free retrievals for each transmission spectrum.

Fig Set 5.1 enables a comparison between the retrieval model behavior in the presence of both strong stellar contamination and an atmospheric signal for the individual visit spectra and the co-added spectrum. When clouds are included in the model, significant visit-to-visit variability is seen among the retrieved atmospheric parameters, particularly the atmospheric temperature, cloud-top pressure, and CH_4 (and other gas) abundance. For example, the $\log \text{CH}_4 - \log P_{\text{cloud}}$ covariance is anti-correlated for cloud-top pressures lower than ~ 1 bar, requiring high CH_4 abundances when the clouds are high in the atmosphere (low pressure) and lower CH_4 abundances when the clouds are deep (higher pressure). We note that this cloud-composition degeneracy has been reported in previous atmospheric studies (e.g., Iyer et al. 2016; MacDonald & Madhusudhan 2017; Pinhas et al.

2019). In addition to correlations with gas abundances, the cloud-top pressure is also correlated with the 10 bar planet reference radius and the atmospheric temperature. When the retrieval finds a preference for the clouds to be at relatively low pressures, it also finds the atmosphere to be hot, significantly exceeding the equilibrium temperature of the planet.

Fig Set 5.1 also shows a positive correlation between the reference radius and the star spot temperature. Given the significant stellar contamination present in the transmission spectrum, it is not surprising that slight vertical offsets in transit depths between visits could be explained by either slight offsets to the planet (reference) radius or slightly different characteristics in the star, as probed by the star spots and their effective temperature and area covering fraction. Thus, we propose that slight differences in the TLS contamination and noise properties intrinsic to each visit propagate through the planet reference radius and cloud-top pressure covariances into the other planetary parameters, such as the atmospheric temperature and gas abundances. In this way, retrieval degeneracies between the planet and stellar parameters obscure atmospheric characteristics from being accurately inferred. We emphasize that without multiple visits this would not have been as simple to diagnose.

Considering the full covariances explored by the three visits, some atmospheric characteristics are much more physically plausible than others. The atmospheric temperature reaches > 1000 K in the region of the solution space where the clouds are at high altitudes ($P_{\text{cloud}} \sim 10^{-3}$ bar), such that these solutions are discarded as nonphysical. Based on this analysis, it appears that the cloud parameters may over-fit the spectrum and lead to nonphysical solutions. Combined with the weak preference for clouds in the analysis of the co-added spectrum, we choose to consider cloud-free models for the visit-to-visit analyses. As discussed previously (see §5.2.1), Table 6 shows that including clouds in the model does not improve the goodness-of-fit and that clouds are only weakly favored over the cloud free model. Therefore, we next consider visit-to-visit analyses using the M3.1 “TLS + Atm” model.

When clouds are omitted from the retrieval, we find that the three visits converge to a more consistent atmospheric interpretation. The gas abundances not only agree more closely between the three visits, but they are consistent with the cloudy models when the clouds were found to be deep in the atmosphere (i.e., they agree along the cloud-top pressure covariance). The isothermal temperature (see Table 5) agrees between visits to within 1σ and does not significantly exceed the planet’s

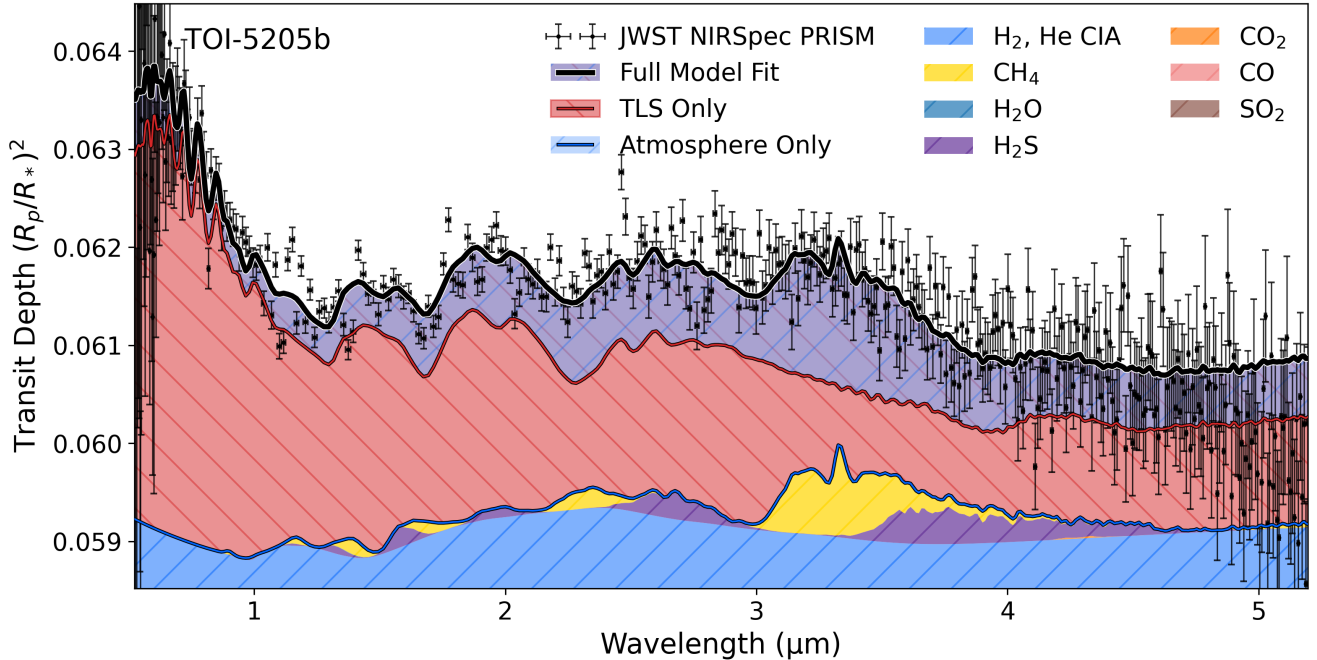


Figure 6. Maximum *a posteriori* retrieved transmission spectrum (black line) with the contributions, derived using POSEIDON, shown from stellar contamination (red line) and atmospheric opacity (blue line). The contributions from individual atmospheric species are shown with various colors (see legend). **Takeaway:** The transmission spectrum of TOI-5205b is characterized by strong stellar contamination throughout much of the 0.6 – 3.5 μm wavelength range, with evident absorption from the planetary atmosphere due to CH_4 and H_2S . All other molecular species are not significantly detected in our retrieval (see Table 5).

equilibrium temperature ($T_{\text{eq}} = 742 \text{ K}$), as was found with the cloudy models. Therefore, we favor the cloud-free results (M3.1), which suggests that clouds, if present in an isothermal atmosphere, are likely deep at pressures $\gtrsim 0.5 \text{ bar}$ (see Fig Set 5.4) where the spectrum is not significantly affected by them.

5.2.3. Atmospheric retrievals on the co-added transmission spectrum

Figure 6 compares the median model posteriors to the co-added transmission spectrum, along with the contributions from the stellar and planetary components to visualize their individual impact on the observations. The stellar contamination component (red line) is calculated to show how the transmission spectrum would appear if the planet possessed a gray transmission spectrum with a radius aligned with the y-axis lower limit (the retrieved 10 bar reference radius). Similarly, the planetary component (blue line) is calculated to visualize how the transmission spectrum would appear if TOI-5205 were inactive and did not contaminate the spectrum.

Overall, the transmission spectrum of TOI-5205b is highly contaminated by a heterogeneous stellar disk. Stellar contamination increases the transit depth by nearly 0.005 ($\sim 8\%$ increase) in the optical and ~ 0.001 at 5 μm ($\sim 2\%$ increase). Despite stellar contamination, substantial atmospheric features remain identifiable in

the spectrum, primarily due to CH_4 and H_2S which are not found in stellar spots. In the co-added transmission spectrum, we detect CH_4 at 9.2σ and H_2S at 5.2σ confidence. In addition, we found independent evidence for CH_4 and H_2S in each visit, with CH_4 detected at 5.9σ in Visit 1, 7.4σ in Visit 2, and 3.9σ in Visit 3, and H_2S detected at 2.6σ in Visit 1, 4.4σ in Visit 2, and 1.7σ in Visit 3. An additional case with NH_3 (not shown) added to the POSEIDON free retrieval yielded a weak 2.0σ detection over the M3.1 model that omitted NH_3 , with a 1σ VMR constraint of $-6.64^{+0.35}_{-0.73} \text{ dex}$ (see more details in E.4).

6. STELLAR METALLICITY

Knowledge of the stellar metallicity enables comparisons between other exoplanetary systems and the Solar System (e.g., Welbanks et al. 2019; Sun et al. 2024). The metallicity of TOI-5205 was assumed to be solar ($[\text{M}/\text{H}] = 0$) in Kanodia et al. (2023) based on the predictions from various photometric relationships. To verify the metallicity, we analyzed an archival 0.8–2.4 μm SpeX spectrum (Rayner et al. 2003) of TOI-5205 from the NASA Infrared Telescope Facility Data Archive at IRSA (Program ID 2022B-049, PI: B. Rackham). The data were processed using the IDL Spextool pipeline (Cushing et al. 2004) and corrected for telluric absorption using the xtellcor routine (Vacca et al. 2003). The

spectrum was then shifted to the vacuum rest frame of the star via cross-correlation with a template star spectrum HD 36395. We measured the K-band metallicity using empirical relationships between line indices and metallicity for M dwarfs in wide-binary systems with an FGK companion with a well-measured metallicity (Mann et al. 2013; Rojas-Ayala et al. 2012). This yielded an $[\text{Fe}/\text{H}]$ of 0.56 ± 0.10 .

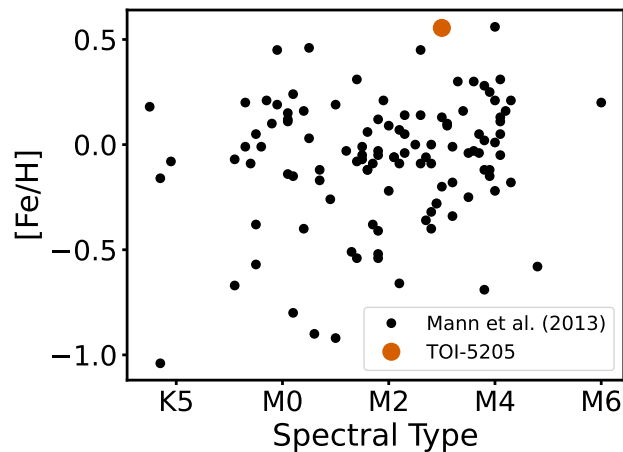


Figure 7. Comparison of the metallicity calibration sample from Mann et al. (2013) (black points) to our measured metallicity of TOI-5205 (red point). The metallicities are shown plotted against host star spectral type. Our measured metallicity is at the upper limit of the calibration sample.

We caution that our measured metallicity is at the upper limit of the metallicity range in the calibration sample used in Mann et al. (2013) (see Figure 7). We chose to adopt the empirical metallicity relationships derived from moderate-resolution K-band infrared spectra over both photometric relationships (e.g., Bonfils et al. 2005; Schlaufman & Laughlin 2010; Neves et al. 2012) and those from high-resolution red-wavelength spectra (e.g., Yee et al. 2017). Photometric metallicities are calibrated on spectroscopically derived metallicities and may be susceptible to training set biases (e.g., Dittmann et al. 2016; Hardegree-Ullman et al. 2020; Anderson et al. 2021). Determining the stellar metallicity from high-resolution spectra with template matching methods (e.g., SpecMatch-Emp; Yee et al. 2017) relies on comparison with a grid of spectra in T_{eff} , $\log g$, and $[\text{Fe}/\text{H}]$ space. This may be unreliable because of degeneracies between stellar parameters, particularly for M dwarfs with many atomic and molecular lines. The empirical relationships we adopt are derived from measured companion star metallicities and calibrated on several line indices to a precision of ~ 0.1 dex. As such, despite the uncertainties associated with our relatively high mea-

surement for TOI-5205, it likely does have a super-solar metallicity. We adopt this metallicity for the star and note that this measurement could be refined in the future with a higher S/N spectrum, as the archival spectrum measured a $S/N \approx 60$ at 2.2 μm .

7. BULK METALLICITY

Characterizing the interiors of giant planets is a crucial step in improving our understanding of their formation history (Guillot et al. 2006; Johansen & Lambrechts 2017; Hasegawa et al. 2018; Hasegawa & Swain 2024). A key property of a giant planet is the bulk metallicity (or bulk heavy element mass). This property, however, must be inferred indirectly from mass-radius measurements (Miller & Fortney 2011; Thorngren et al. 2016). The measured atmospheric metallicity of TOI-5205b is a crucial additional constraint for the planet’s interior and lifts part of the degeneracy concerning its composition and the distribution of heavy elements within the planet (e.g., Thorngren & Fortney 2019; Müller & Helled 2023a; Burrows et al. 2007; Müller et al. 2020a).

To infer the heavy element content of TOI-5205b, we used the `planetsynth` evolution models that account for stellar irradiation and atmospheric composition (Müller & Helled 2021). The evolution models used a 50 – 50 H_2O - SiO_2 (water-rock) mixture for the heavy elements (More et al. 1988), and a proto-solar hydrogen-helium mixture (Chabrier et al. 2019). We employed a common Monte-Carlo approach (e.g., Müller & Helled 2023b) in which the observations were used as priors, sample planets were drawn, and their thermal evolution was modeled to find the heavy element mass that fit the observed radius. Gaussian priors were used for the mass, radius, and stellar irradiation. Since the host-star age is largely unknown (Kanodia et al. 2023), we used a uniform prior between 2 and 10 Gyr. For the atmospheric metallicity (see §4), the inferred values approached the edge of their respective grids, and their posterior distributions were asymmetric. Therefore, we used a uniform prior for $\log [M/\text{H}]$ from -1.0 to -0.3 to ensure the samples were within the model limits.

The posterior distribution of the bulk metallicity estimated from 10^6 planet samples is shown in Figure 8. We also depict the region where the bulk metallicity equals the atmospheric metallicity. The inferred bulk metallicity and heavy element mass were $Z_{\text{planet}} = 0.17 \pm 0.07$ and $M_z = 57 \pm 25 M_{\oplus}$, respectively. The large errors were mainly driven by the radius and age uncertainties. For comparison, interior models of Jupiter infer a heavy element mass of about 20 – 30 M_{\oplus} (see Helled & Howard 2024, for a review). Interestingly, the high bulk metallicity of TOI-5205b challenges the finding that giant plan-

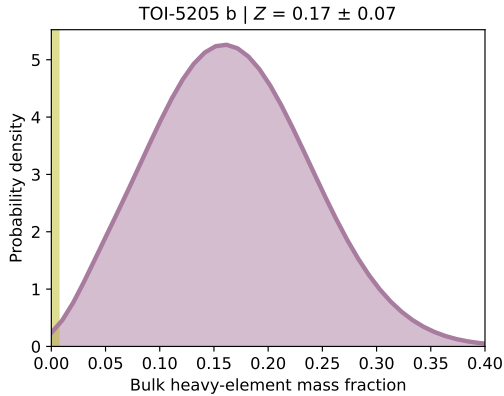


Figure 8. Posterior distribution of the bulk metallicity (Z_{planet}) inferred with thermal evolution models. The shaded olive region denotes the atmospheric metallicity. **Takeaway:** The inferred bulk metallicity, much higher than the atmospheric metallicity, is incompatible with a homogeneously mixed planet.

ets around M-dwarf stars are metal-poor compared to those around FGK stars (Müller & Helled 2024a).

Figure 9 shows the cooling curves of TOI-5205b for two scenarios: (i) models that use the range of inferred bulk metallicities (purple line and shaded region) and (ii) one that has a bulk metallicity equal to the median atmospheric metallicity (dashed olive line). The cooling curve for the latter case clearly shows that the observed radius ($R_p = 0.94 \pm 0.04 R_J$ derived from the white light curve, see Table 2) cannot be matched if the planet had a sub-stellar bulk metallicity. This implies that TOI-5205b is not fully mixed and that the heavy element mass fraction is higher in the interior. Recent observations of Jupiter with Juno and Galileo have called into question the distribution of heavy elements in its interior (Debras & Chabrier 2019; Howard et al. 2023; Müller & Helled 2024b), but similar inferences regarding the extent to which atmospheric metallicity is linked to the planetary bulk composition for exoplanets have not yet been determined.

We note that in addition to the formal error from the Monte-Carlo inference, there are other uncertainties related to the model details, such as equations of state, atmospheric models, energy transport, and composition gradients (Baraffe et al. 2008; Kurokawa & Inutsuka 2015; Poser et al. 2019; Howard & Guillot 2023). In particular, the inferred bulk composition can be influenced by the assumed chemical composition of the heavy elements. The `planetsynth` models used a 50-50 water-rock mixture for the heavy elements and, to test the sensitivity of the inferred bulk metallicity to our choice of heavy element materials, we calculated additional evolution models using the modified version of the

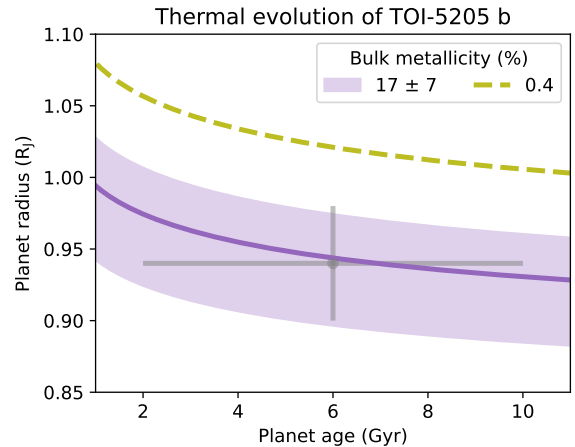


Figure 9. Thermal evolution of TOI-5205b assuming either that the bulk metallicity equals the inferred value and its uncertainty (purple) or the median atmospheric metallicity (dashed olive). The gray error bars show the measurement values and their uncertainties. Note that, unlike the radius, we consider each planetary age shown as equally likely. **Takeaway:** The cooling curves demonstrate that the planet must be metal-rich and inhomogeneous.

stellar evolution code Modules for Experiments in Stellar Astrophysics (MESA; Paxton et al. 2011, 2013, 2015, 2018, 2019; Jermyn et al. 2023) from Müller & Helled (2024b). For these models, we adopted a pure rock equation of state for the heavy elements and attempted to fit the mean observed radius at the median stellar age. The inferred bulk metallicity was $Z_{\text{planet}} \sim 0.12$ and remained larger than the observed atmospheric metallicity ($\lesssim 1\%$). Overall, we conclude that the model uncertainties due to the choice of heavy element materials are unlikely to be responsible for this super-solar bulk metallicity.

8. DISCUSSION

8.1. TOI-5205b does not have a haze or cloud-dominated atmosphere

Espinoza et al. (2019) investigated the TLS effect as another plausible source for generating a large spectral slope in the transmission spectra. In the case of WASP-19b, Espinoza et al. (2019) reported that unocculted star spots could explain the anomalously large scattering slope. The recovered spot and faculae fractions from M3.1 ($f_{\text{spot}} = 0.132^{+0.015}_{-0.013}$ and $f_{\text{fac}} = 0.0146^{+0.0053}_{-0.0040}$) suggest that the unocculted surface of TOI-5205b has a small, but non-negligible, percentage of spots and a negligible percentage of faculae, which is consistent with spot coverage fractions for other mid-M dwarfs (Almeida et al. 2022; Mori et al. 2024). Therefore, the observed features (particularly the spectral slope at bluer wavelengths) are most likely dominated by spots. How-

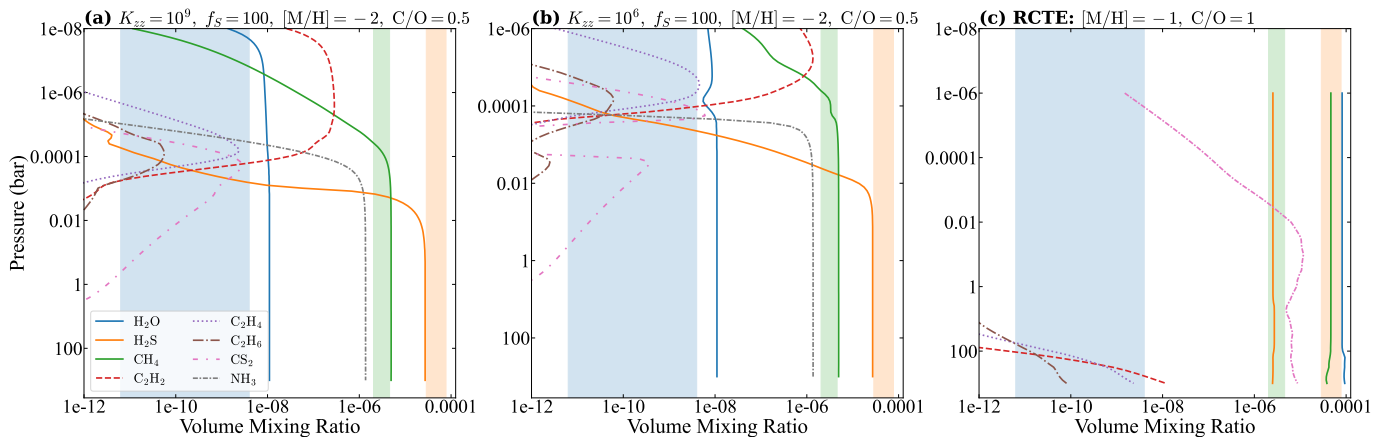


Figure 10. The volume mixing ratios of the most abundant hydrocarbons, H₂O, and H₂S from the best-fitting models in §4.2 for (a) $\log K_{zz} = 9$ (b) $\log K_{zz} = 6$, and (c) RCTE. The $\pm 1\sigma$ VMRs retrieved, assuming free chemistry, in §5.2.3 using POSEIDON are denoted by the shaded regions for H₂O (blue), CH₄ (green), and H₂S (orange).

ever, the high degree of TLS contamination precludes a detailed constraint on any minor contributions from hazes and clouds, if any, to the observed transmission spectra of TOI-5205b (see Table 6).

We have assumed that the TLS effect is the source of the observed spectral slopes in the transmission spectra of TOI-5205b based on the presence of spot-crossing events and results from our atmosphere models (see Figure 2). However, we acknowledge that photochemical hazes and/or clouds may also introduce a spectral slope where the observed transit depth increases towards bluer wavelengths (e.g., Sing et al. 2016; Sedaghati et al. 2017; May et al. 2018). Haze formation is expected to become efficient for cool exoplanets at temperatures $T_{\text{eq}} < 1000$ K (e.g., Kawashima & Ikoma 2019; Gao et al. 2021). The spectral index is $\gamma = -4$ (Lecavelier Des Etangs et al. 2008) in the case of nominal Rayleigh scattering caused by small aerosol particles. If the spectral slope observed in the spectrum of TOI-5205b were solely due to hazes, this would require enhanced scattering (“super-Rayleigh” scattering in Ohno & Kawashima 2020) that is much larger than values observed for hot Jupiters. The best-fitting haze and cloud model (M3.4 in Table 6) for the co-added spectrum required a scattering slope of $\gamma = -17.0 \pm 0.4$ and a Rayleigh enhancement factor relative to H₂ of $\log a = 7.9 \pm 0.1$. For comparison, the median values for an identical haze and cloud model derived from a population of hot Jupiters observed with HST (e.g., Pinhas et al. 2019; Welbanks et al. 2019) were $\gamma \lesssim -5$ and $\log a \sim 4 - 5$. The observed slope for TOI-5205b (~ 10) was similar to a few other planets that displayed even larger scattering slopes (with a similar haze and cloud prescription), such as WASP-19b ($\gamma \sim -26$; Sedaghati et al. 2017) and HATS-8b ($\gamma \sim -35$ May et al. 2018).

Ohno & Kawashima (2020) investigated microphysical models of hazes and demonstrated that, under certain conditions (preferentially when $T_{\text{eq}} = 1000 - 1500$ K or for efficient eddy mixing when the diffusion coefficient is $\log K_{zz} \gtrsim 9$), photochemical hazes can enhance the spectral slope by factors of 2 – 4. The scattering slope from model M3.4 exceeds the maximum scattering slope investigated by (Ohno & Kawashima 2020) ($-16 \leq \gamma \leq 0$), suggesting only extreme values of $\log K_{zz} > 10$ could generate the slope observed in TOI-5205b. Pinhas & Madhusudhan (2017) investigated the impact of mineral clouds (e.g., sulfide and chloride clouds) on the transmission spectra. KCl, Na₂S, and ZnS are the only known major mineral cloud species with condensation curves that cross the equilibrium temperature of TOI-5205b (based on Virga; Batalha et al. 2020; Rooney et al. 2022). These cloud species are unable to produce a scattering slope $\gamma < -8$ even if the cloud scale height is assumed to be identical to the atmospheric scale height. This suggests that neither mineral clouds nor hazes alone can reproduce the observed spectral slope in the transmission spectrum of TOI-5205b.

We note that hydrocarbon aerosols, as opposed to silicate clouds and aerosols, are expected to be the dominant aerosol composition for giant exoplanets with $T_{\text{eq}} < 950$ K (Gao et al. 2020) in part because the primary carbon reservoir changes from CO to CH₄ (e.g., Lodders & Fegley 2002; Liang et al. 2004; Fortney et al. 2020), which can photodissociate and is a known source of hydrocarbon hazes in the Solar System (e.g., Hörst 2017; Mandt K. et al. 2023; Zhang 2024; Gao & Ohno 2024). In the context of warm gas giants, such as TOI-5205b, various studies (Line et al. 2010, 2011; Venot et al. 2015; Molaverdikhani et al. 2019) have shown that photochemistry could destroy simple species (such as CH₄) and produce more complex hydrocarbons, like

acetylene (C_2H_2) and benzene (C_6H_6), that may be important precursor molecules for haze (e.g., Morley et al. 2015; Venot et al. 2020; Tsai et al. 2021). We use the best-fitting VULCAN models (see §4.2) to investigate the inventory of hydrocarbon species that may be present in the atmosphere and could form photochemical hazes. In the VULCAN model, all hydrocarbons, except CH_4 , are present at volume mixing ratios (VMRs) that may be too low to robustly recover in the presence of CH_4 when using NIRSpec PRISM (e.g., like the warm Jupiter Kepler-30 c in Gasman et al. 2022). Furthermore, such low VMRs ($\log X < -8$ for all hydrocarbons except CH_4 and C_2H_2 , see Figure 10) could limit the formation rate of polycyclic aromatic hydrocarbons, such as benzene (C_6H_6), which are major precursors of more complex haze species (e.g., Tsai et al. 2021), suggesting that extensive hydrocarbon haze formation may not occur on TOI-5205b. This is consistent with the POSEIDON free retrievals that do not favor models exclusively containing hazes or clouds and which show inconsistencies in the atmospheric chemistry between visits when clouds or hazes are included.

8.2. TOI-5205b appears to have an atmosphere with a low metallicity and high C/O ratio

The retrievals assuming chemical equilibrium consistently approached (i) the lower limits of the grid with respect to metallicity ($\log [M/H]_{\text{PLATON}} \geq -2$ and $\log [M/H]_{\text{POSEIDON}} \geq -1$) and (ii) the upper limit of the grid with respect to the C/O ratio ($\log C/O \leq 2$). These results indicate a sub-solar atmospheric metallicity and a super-solar C/O ratio. Figure 11 displays the posteriors of all retrievals on the co-added spectrum (both assuming free chemistry and equilibrium chemistry) along with the implicit priors calculated for our free chemistry retrievals (see Table 5). The atmospheric [M/H] and C/O was derived from the POSEIDON free retrieval posteriors using the retrieved VMRs of all molecular species in the models (e.g., MacDonald & Madhusudhan 2019). The limitations of the chemical equilibrium grids created an artificial boundary in the posterior distributions for [M/H] and C/O. This restriction was relaxed in our free chemistry retrievals (§5.2.3), where the posteriors of the cloud-free model (M3.1) favored $\log [M/H] = -2.59 \pm 0.65$ and $\log C/O = 2.85 \pm 2.21$ (at 3σ). Our retrievals including clouds (M3.2) gave approximately the same constraint on the C/O ratio, but had much higher gas abundances and, therefore, favored a metallicity consistent with solar composition $\log [M/H] = 0.07^{+0.42}_{-3.10}$ (at 3σ). Despite having more flexibility than the chemical equilibrium grids, the broad log-uniform priors on the molecular abundances in the

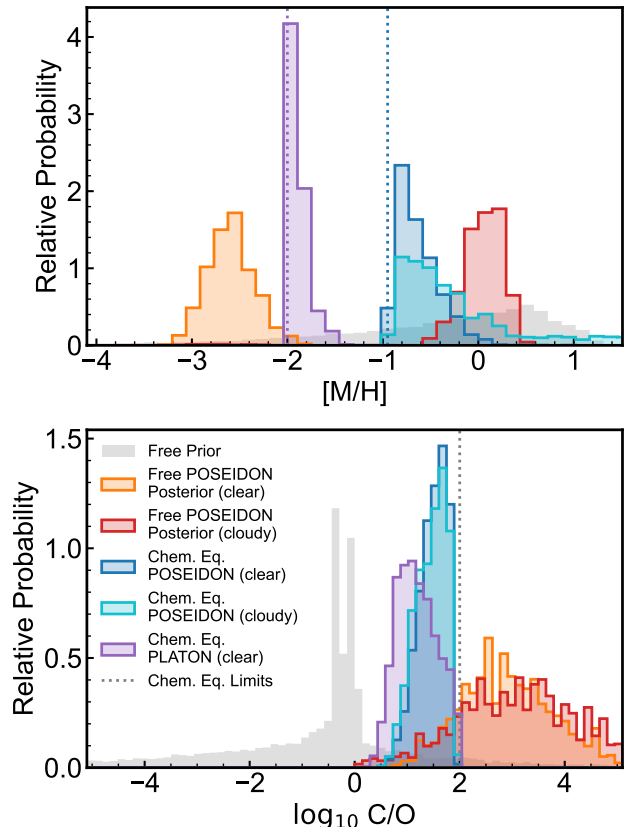


Figure 11. The posterior distributions for the co-added TOI-5205b spectrum from retrievals with PLATON and POSEIDON and the implicit prior distributions for the atmospheric chemistry calculated for the free retrieval with POSEIDON. **Top:** The posteriors for the atmospheric metallicity, [M/H]. **Bottom:** The posterior distributions for the C/O ratio. In each panel, the limits to the chemical equilibrium grids are denoted with dotted lines. **Takeaway:** All chemical equilibrium retrievals pushed the limits of their respective grids, but the free retrievals showed that the metallicity, while likely sub-solar, remained dependent on the unconstrained presence of clouds. The C/O ratio is consistently super-solar and insensitive to the presence of clouds.

free retrievals (see Table 5) propagated into complex shapes in [M/H] and C/O that were not flat in Figure 11. Although these non-flat priors clearly do not dominate the [M/H] and C/O posteriors, they may contribute to the lower limit on [M/H] and the upper limit on C/O as opposed to these constraints being strictly from the data.

The discrepancy in atmospheric metallicity exhibited between our clear and cloudy POSEIDON free retrievals renders it challenging to pin down a firm metallicity constraint, however a sub-solar metallicity is most likely. Although the free cloudy retrieval provides a plausible fit to the spectrum that is consistent with solar metallicity within 1σ ($\log [M/H] = 0.07^{+0.19}_{-0.22}$), as discussed in

§5.2.2, this model exploited degeneracies between several free parameters to produce atmospheric solutions that appeared nonphysically hot and discrepant between our three separate visits. From the covariances in [Figure Set 5.1 – Overview](#), the region of parameter space where the cloudy retrievals offer the highest metallicity correspond to those with the lowest pressure cloud-top and the hottest atmosphere. Furthermore, the extended metallicity lower limit (down to -3.03 at 3σ) seen in these cloudy results bridges the metallicity gap seen in [Figure 11](#) to our low metallicity cloud free results. This suggests that the clouds may indeed be deep in the atmosphere. It is also possible that intermediate cloud-top pressure solutions with intermediate metallicity values would be preferred if not for complications caused by retrieval degeneracies, stellar contamination, and the interplay of the two.

In the free chemistry retrieval, only CH_4 and H_2S are significantly detected (see M3.1 in §5.2.3). The abundances for these molecules retrieved from the model without clouds are comparable to the VMRs from the best-fitting VULCAN models with enhanced S abundance, regardless of K_{zz} , but are very discrepant with the abundances derived assuming chemical equilibrium and solar elemental ratios. For comparison, the retrieved VMRs for M3.1 using POSEIDON are $\log[\text{CH}_4] = -5.53_{-0.16}^{+0.19}$ and $\log[\text{H}_2\text{S}] = -4.32_{-0.22}^{+0.21}$ while the VMRs from the best-fitting VULCAN model that accounts for disequilibrium processes (with $[\text{M}/\text{H}] = -2.0$ and $f_S = 100$) reach values of $\log[\text{CH}_4] = -5.31$ and $\log[\text{H}_2\text{S}] = -4.57$. These VMRs agree with to within 2σ .

Water (H_2O) is expected to be readily detected in the atmosphere of warm gas giants (e.g., [Fortney et al. 2020](#)). In the case of TOI-5205b, the low retrieved VMR of H_2O ($\log[\text{H}_2\text{O}] = -9.7_{-1.5}^{+1.3}$) is partly due to modeling uncertainties associated with the TLS effect. [Moran et al. \(2023\)](#) caution that heterogeneities on the surface of M dwarfs may significantly impact the transmission spectrum and the retrieved water abundance when there is stellar contamination. [Figure 6](#) displays the contamination spectrum derived with POSEIDON, which contributes the most to the spectral features between $1-3.5$ μm . This is the same region that is most sensitive to water features in the NIRSpec/PRISM bandpass (e.g., [Fortney et al. 2020](#)). This degeneracy between $\log[\text{H}_2\text{O}]$ and stellar contamination suggests that the recovered water abundance should be interpreted as a lower limit as some spectral features associated with water may be inadvertently attributed to stellar contamination. The free chemistry retrieval ultimately did not robustly detect any oxygen-bearing molecule (H_2O , CO , CO_2 , or SO_2).

The detection of H_2S and not SO_2 is consistent with a high C/O, low-metallicity atmosphere. H_2S may be a primary sulfur reservoir for cool gas giants and its detectability is strongly dependent on the abundance of sulfur and mostly independent of the temperature or the C/O ratio (e.g., [Zahnle et al. 2009](#); [Wang et al. 2017](#); [Polman et al. 2023](#); [Mukherjee et al. 2024](#)). SO_2 , however, is preferentially detected in atmospheres that are oxygen-rich (low C/O) with high-metallicity as it is primarily formed by the photodissociation of H_2O ([Tsai et al. 2023](#)). For a high C/O ratio atmosphere of a cool gas giant, the detectability of H_2S with NIRSpec/PRISM will depend on the presence of other molecules (due to its lower absorption cross-section, see [Polman et al. 2023](#)). The contribution to the transmission spectrum from H_2S in regions ≤ 3 μm overlaps with the stellar contamination spectrum and so any abundances derived from these regions could be degenerate with stellar surface inhomogeneities (similar to H_2O). [Polman et al. \(2023\)](#) also predict a peak in the contribution from H_2S around ~ 3.8 μm for a warm gas giant and that corresponds to the significant contribution between $3.5-4.5$ μm in [Figure 6](#) observed for TOI-5205b.

8.3. The interior of TOI-5205b

Our results demonstrate that TOI-5205b is rather metal-rich in its bulk and is not fully mixed. The planetary metallicity is $Z_{\text{planet}} = 0.17 \pm 0.07$ ($\sim 17\%$), which is intriguing because the host star is an M dwarf that is less massive than the Sun ($M_\star = 0.394 \pm 0.011 M_\odot$) and the low-mass of the star should be associated with a less massive protoplanetary disk and less available solids (e.g., [Laughlin et al. 2004](#)). While formation and evolution models clearly demonstrate that the atmosphere could be enriched due to heavy element accretion ([Mousis et al. 2009](#); [Shibata & Ikoma 2019](#); [Shibata et al. 2020](#); [Müller & Helled 2024b](#)), our measured low atmospheric metallicity requires either little pollution or for most of it to have settled. In addition, primordial composition gradients are expected to become (at least partially) eroded, polluting the envelope from below ([Vazan et al. 2018](#); [Müller et al. 2020b](#); [Knierim & Helled 2024](#)). Our inferred bulk metallicity being inconsistent with a fully mixed planet could hint that there was no significant enrichment with material from the deep interior. This would require the planet to form very cold or mixing to be inhibited.

While the apparent discrepancy between the atmospheric and bulk metallicity appears surprising, we note that the region where the atmospheric metallicity is measured is only at very low pressures and, therefore, unlikely to represent the bulk or even the full atmo-

spheric metallicity. Future measurements of the atmospheric metallicities of giant planets around low-mass stars, including from this survey, will provide a more statistical view of the metallicities and heavy element distributions of this enigmatic population (Kanodia et al. 2024).

8.4. Implications for formation

The sub-solar atmospheric metallicity of TOI-5205b combined with its high atmospheric C/O ratio currently appears to be unique (e.g., Kempton & Knutson 2024). The atmosphere of a giant planet is predicted to have a sub-solar metallicity if, during runaway gas accretion, heavy elements in the form of pebbles or planetesimals are not accreted or if the accreted gas is metal-poor. This depends on the planet’s formation process, its location in the disk, and its migration history (Shibata et al. 2020; Turrini et al. 2021; Pacetti et al. 2022). We note that TOI-5205b has a bulk heavy element mass of about $55M_{\oplus}$, which is rather high given that it orbits an M dwarf star where less heavy elements should be available during the early stages of planet formation (Andrews et al. 2013; Pascucci et al. 2016). The inferred high bulk metallicity and low atmospheric metallicity of TOI-5205b hint that most (if not all) of the available heavy elements accreted by the planet were deposited in the deep interior during its formation.

The high C/O ratio measured in the atmosphere could be explained if the planet accreted its gas in a region where carbon was abundant due to the evaporation of methane-rich pebbles (Schneider & Bitsch 2021; Mah et al. 2023). Recent JWST/MIRI observations of the inner regions of mid-to-late M-dwarf protoplanetary disks (Tabone et al. 2023; Arabhavi et al. 2024; Long et al. 2024) are finding carbon-rich disks with abundant hydrocarbons in the gas phase, weak water emission, and high C/O ratios.⁷ It is important to note, however, that the C/O ratio can be influenced by factors beyond the planet’s initial formation location. Late-stage accretion of carbon-rich planetesimals can increase the atmospheric C/O ratio, even if it initially formed in a region with a lower gas-phase C/O ratio (Öberg et al. 2011). Similarly, processes like atmospheric escape or dredge-up of core material due to convective mixing can alter the observable C/O ratio after the planet has formed, albeit such processes would also increase the atmospheric metallicity (Müller et al. 2020b; Kempton & Knutson 2024).

As a result, using the atmospheric C/O ratio as a tracer for formation should be done cautiously, since pebble evaporation, disk chemistry, planetary migration, accretion and mixing history, and late pollution of the atmosphere can affect the atmospheric C/O ratio (Schneider & Bitsch 2021; Turrini et al. 2021). Since most of the sulfur in a protoplanetary disk is locked in solids, the enhanced sulfur in the atmosphere of TOI-5205b may suggest that the planet had undergone extensive migration and accreted significant amounts of planetesimals into its envelope (Turrini et al. 2021). However, to better constrain the formation history of a giant planet, measurements of other elemental ratios (e.g., C/N, N/O, S/N) combined with a reliable measurement of the host-star abundances are required (Turrini et al. 2021; Pacetti et al. 2022). Finally, additional measurements of the C/O ratios and atmospheric metallicity in giant planets orbiting M dwarfs would put the atmospheric composition of TOI-5205b in perspective.

8.5. Current limitations and future improvements

The treatment of stellar contamination in both the light curves and the transmission spectra is a limitation of this work. The data show strong evidence for stellar activity (see Figure 1) that is evolving with time (e.g., different spot configurations, spectral slopes, and spectral baselines). The TLS effect is a recurring problem for recent M dwarf atmospheric studies (e.g., Lim et al. 2023; Moran et al. 2023; May et al. 2023; Fournier-Tondreau et al. 2024) and the observations of TOI-5205b, along with other planets in our survey, are a benchmark data set to investigate further improvements for data analysis in the presence of stellar contamination. We attempted to correct for stellar activity by (i) deriving transmission spectra using a spot-crossing model and (ii) including a stellar contamination model in our atmospheric retrievals (e.g., Rackham et al. 2018). However, we made certain assumptions in our modeling that can be improved upon in future work, such as (i) relaxing the assumption that the contrast is fixed and accounting for rotational effects in the light curve model (e.g., Kipping 2012; Luger et al. 2021; Morris 2022) or (ii) attempting a multi-epoch transmission spectra retrieval with a fixed planetary atmosphere model and variable stellar contamination spectra unique to each observation.

A persistent issue with atmospheric retrievals for planets orbiting M dwarfs is that the photospheric models for these stars currently impose limitations on the reliability of the calculated contamination spectra (e.g., Lim et al. 2023; Radica et al. 2024; TRAPPIST-1 JWST Community Initiative et al. 2024). The contamination spec-

⁷ Though exceptions like the molecule-rich Sz 114 disk exist (Xie et al. 2023).

tra calculated in atmospheric retrievals are based on 1D spectral models (PHOENIX in this work) and, given the lack of model fidelity for M dwarfs (e.g., [Rajpurohit et al. 2018](#)), this imposes a limit to the accuracy of these corrections. These interpolated stellar models are in stark contrast to the relatively complex, high-dimensional 1D atmospheric models used for the planet, despite the fact that the contaminating TLS signal exceeded that of the planet atmosphere for TOI-5205. [Rackham et al. \(2023\)](#) note that reliably correcting stellar contamination, in both photometry and transmission spectra, requires various theoretical improvements to model features that may impact the spectra (e.g., small-scale and spot-like magnetic heterogeneities). Our work here further motivates such improvements.

Recent efforts to model surface inhomogeneities have emphasized the need to account for magnetohydrodynamic effects to reliably model spots and faculae (e.g., [Witzke et al. 2022](#); [Rackham & de Wit 2024](#)). One-dimensional radiative-equilibrium models are unable to reproduce the spectral features and profiles that are predicted through comprehensive three-dimensional radiative magnetohydrodynamic simulations of spotted stars, and this can result in significant error for the contamination spectra of M dwarfs (e.g., [Norris et al. 2023](#); [Smitha et al. 2024](#)). The limb-darkening derived from 1D spectra may also impose limitations on the modeling of the photometry (see [Appendix C](#)) and there are active efforts to account for magnetohydrodynamic effects in the generation of stellar atmosphere models (e.g., [Kostogryz et al. 2024](#); [Witzke et al. 2024](#)). While there may be empirical improvements to the stellar contamination model using higher-resolution observations of the host star that are contemporaneous with the transmission spectra (e.g., [Berardo et al. 2024](#); [Waalkes et al. 2024](#)), such a dataset does not exist for the GEMS JWST survey.

We also adopted an isothermal pressure-temperature profile for its simplicity (i.e., limited number of additional free parameters) in our complex atmospheric models. We note that previous studies have shown that the simple assumption of an isothermal pressure-temperature profile may bias the retrieved chemical abundances to lower values (e.g., [Welbanks & Madhusudhan 2019](#)). In addition, there may be potential degeneracies between the stellar contamination model and the atmospheric chemistry as a result of imperfect TLS modeling (e.g., using PHOENIX model spectra) that could affect the retrieved abundances.

Observing TOI-5205b at redder wavelengths would also mitigate the impact of TLS on the spectra ([Seager & Shapiro 2024](#)). Observations of a warm Jupiter

with MIRI may provide valuable constraints on the presence of more complex hydrocarbons (e.g., [Gasman et al. 2022](#)), microphysical cloud models (e.g., [Kiefer et al. 2024](#)), additional nitrogen chemistry ([Welbanks et al. 2024](#)), and additional haze precursors (e.g., [Mukherjee et al. 2024](#)). We note that the data obtained from this GEMS JWST survey are exclusively transmission spectra. TOI-5205b is a favorable target for emission spectroscopy ([Kanodia et al. 2023](#)) which may provide additional constraints on the atmospheric chemistry ([Mukherjee et al. 2024](#)) while having minimal effects from stellar activity.

9. CONCLUSION

We have presented the first transmission spectra of TOI-5205b, a warm Jupiter orbiting an M dwarf. We reduced the data with two reduction pipelines ([Eureka!](#) and [ExoTiC-JEDI](#)) and derived consistent transmission spectra using a model that included spot-crossing events. Although there is significant stellar contamination in the transmission spectra, both retrievals assuming equilibrium chemistry and allowing free chemistry infer that the atmosphere of TOI-5205b has a sub-solar metallicity ($\log [M/H] \lesssim -2.5$) and a super-solar carbon-to-oxygen ratio ($\log [C/O] \gtrsim 1$), which results in no robust detections of oxygen-bearing molecules in the atmosphere. Retrievals assuming free chemistry provide a $> 5\sigma$ detection of both methane ($\log [CH_4] = -5.53^{+0.19}_{-0.16}$) and hydrogen sulfide ($\log [H_2S] = -4.32^{+0.21}_{-0.22}$) in the atmosphere of TOI-5205b at abundances that are within 2σ from the expected values when accounting for disequilibrium processes and sulfur enhancement. We do not robustly detect water with the NIRSpec/PRISM data, most likely due to significant stellar contamination. From the planet mass and radius, we estimate a bulk metallicity of $Z_{\text{planet}} = 0.17 \pm 0.07$, which is in stark contrast to the metal-poor atmosphere we observe. The high bulk and low atmospheric metallicity suggest that TOI-5205b is not fully mixed, similar to the giant planets in the solar system. TOI-5205b is one of seven planets in our GEMS JWST survey (GO 3171) — *Red Dwarfs and the Seven Giants: First Insights Into the Atmospheres of Giant Exoplanets around M dwarf Stars* ([Kanodia et al. 2023](#)) — that will provide a sample of well-characterized warm Jupiter atmospheres that will (i) provide atmospheric and bulk metallicities to place TOI-5205b in greater context and (ii) allow for a comparison with hot Jupiters and Solar System gas giants to investigate potential constraints on the formation of GEMS.

ACKNOWLEDGMENTS

We thank Adriana Kuehnel and Zafar Rustamkulov for assistance in reducing JWST data as part of the GEMS JWST survey. We thank Michael Zhang and Ryan MacDonald for assistance with the PLATON and POSEIDON codes, respectively.

This work is based on observations made with the NASA/ESA/CSA James Webb Space Telescope. The data were obtained from MAST at STScI, which is operated by the Association of Universities for Research in Astronomy, Inc., under NASA contract NAS 5-03127 for JWST. These observations are associated with program #3171. Support for program #3171 was provided by NASA through a grant from the Space Telescope Science Institute, which is operated by the Association of Universities for Research in Astronomy, Inc., under NASA contract NAS 5-03127.

The JWST data presented in this paper were obtained from MAST at STScI. The specific observations analyzed can be accessed via DOI: 10.17909/29st-dz13. Support for MAST for non-HST data is provided by the NASA Office of Space Science via grant NNX09AF08G and by other grants and contracts. This research has used the NASA/IPAC Infrared Science Archive, which is funded by the National Aeronautics and Space Administration and operated by the California Institute of Technology.

CIC and DRL acknowledge support by NASA Headquarters through an appointment to the NASA Postdoctoral Program at the Goddard Space Flight Cen-

ter, administered by ORAU through a contract with NASA. DRL also acknowledges support from NASA under award number 80GSFC24M0006.

Resources supporting this work were provided by the (i) NASA High-End Computing (HEC) Program through the NASA Center for Climate Simulation (NCCS) at Goddard Space Flight Center, (ii) Pennsylvania State University’s Institute for Computational and Data Sciences’ (ICDS) Roar supercomputer, and (iii) Carnegie Science Earth and Planets Laboratory. This content is solely the responsibility of the authors and does not necessarily represent the views of the NCCS, ICDS, or Carnegie Science.

Facilities: JWST, IRSA, IRTF

Software: `astroquery` (Ginsburg et al. 2019), `astropy` (Astropy Collaboration et al. 2018), `dynesty` (Speagle 2020), `Eureka!` (Bell et al. 2022), `ExoTiC-JEDI` (Alderson et al. 2022), `ExoTiC-LD` (Grant & Wakeford 2024), `jwst` (Bushouse et al. 2023), `juliet` (Espinoza et al. 2019), `lightkurve` (Lightkurve Collaboration et al. 2018), `matplotlib` (Hunter 2007), `numpy` (van der Walt et al. 2011), `pandas` (McKinney 2010), `planetsynth` (Müller & Helled 2021), `PLATON` (Zhang et al. 2019), `POSEIDON` (MacDonald & Madhusudhan 2017), `scipy` (Virtanen et al. 2020), `spotrod` (Béky et al. 2014),

REFERENCES

- Acuña, L., Kreidberg, L., Zhai, M., & Mollière, P. 2024, GASTLI: An Open-Source Coupled Interior-Atmosphere Model to Unveil Gas Giant Composition, doi: 10.48550/arXiv.2406.10032
- Akeson, R. L., Chen, X., Ciardi, D., et al. 2013, PASP, 125, 989, doi: 10.1086/672273
- Alderson, L., Grant, D., & Wakeford, H. 2022, Exo-TiC/ExoTiC-JEDI: v0.1-beta-release, v0.1, Zenodo, doi: 10.5281/zenodo.7185855
- Alderson, L., Wakeford, H. R., Alam, M. K., et al. 2023, Nature, 614, 664, doi: 10.1038/s41586-022-05591-3
- Almenara, J. M., Bonfils, X., Forveille, T., et al. 2022, A&A, 667, L11, doi: 10.1051/0004-6361/202244791
- Anderson, S. G., Dittmann, J. A., Ballard, S., & Bedell, M. 2021, AJ, 161, 203, doi: 10.3847/1538-3881/abe70b
- Andrews, S. M., Rosenfeld, K. A., Kraus, A. L., & Wilner, D. J. 2013, ApJ, 771, 129, doi: 10.1088/0004-637X/771/2/129
- Arabhazi, A. M., Kamp, I., Henning, T., et al. 2024, Science, 384, 1086, doi: 10.1126/science.adi8147
- Asplund, M., Amarsi, A. M., & Grevesse, N. 2021, A&A, 653, A141, doi: 10.1051/0004-6361/202140445
- Astropy Collaboration, Price-Whelan, A. M., Sipőcz, B. M., et al. 2018, AJ, 156, 123, doi: 10.3847/1538-3881/aabc4f
- Atreya, S. K., Crida, A., Guillot, T., et al. 2018, The Origin and Evolution of Saturn, with Exoplanet Perspective, 5–43, doi: 10.1017/9781316227220.002
- Baraffe, I., Chabrier, G., & Barman, T. 2008, A&A, 482, 315, doi: 10.1051/0004-6361:20079321
- Batalha, N., Freedman, R., Gharib-Nezhad, E., & Lupu, R. 2022, Resampled Opacity Database for PICASO, 2.0, Zenodo, doi: 10.5281/zenodo.6928501
- Batalha, N., Rooney, C., & Mukherjee, S. 2020, natashabatalha/virga: Initial Release, v0.0, Zenodo, doi: 10.5281/zenodo.3759888
- Batalha, N. E., Marley, M. S., Lewis, N. K., & Fortney, J. J. 2019, ApJ, 878, 70, doi: 10.3847/1538-4357/ab1b51

- Baxter, C., Désert, J.-M., Tsai, S.-M., et al. 2021, *Astronomy and Astrophysics*, 648, A127, doi: [10.1051/0004-6361/202039708](https://doi.org/10.1051/0004-6361/202039708)
- Béky, B., Kipping, D. M., & Holman, M. J. 2014, *MNRAS*, 442, 3686, doi: [10.1093/mnras/stu1061](https://doi.org/10.1093/mnras/stu1061)
- Bell, T., Ahrer, E.-M., Brande, J., et al. 2022, *The Journal of Open Source Software*, 7, 4503, doi: [10.21105/joss.04503](https://doi.org/10.21105/joss.04503)
- Benneke, B., Roy, P.-A., Coulombe, L.-P., et al. 2024, arXiv e-prints, arXiv:2403.03325, doi: [10.48550/arXiv.2403.03325](https://doi.org/10.48550/arXiv.2403.03325)
- Berardo, D., de Wit, J., & Rackham, B. V. 2024, *ApJL*, 961, L18, doi: [10.3847/2041-8213/ad1b5b](https://doi.org/10.3847/2041-8213/ad1b5b)
- Berdugina, S. V. 2005, *Living Reviews in Solar Physics*, 2, 8, doi: [10.12942/lrsp-2005-8](https://doi.org/10.12942/lrsp-2005-8)
- Birkmann, S. M., Ferruit, P., Giardino, G., et al. 2022, *A&A*, 661, A83, doi: [10.1051/0004-6361/202142592](https://doi.org/10.1051/0004-6361/202142592)
- Bloot, S., Miguel, Y., Bazot, M., & Howard, S. 2023, *MNRAS*, 523, 6282, doi: [10.1093/mnras/stad1873](https://doi.org/10.1093/mnras/stad1873)
- Bodenheimer, P., Hubickyj, O., & Lissauer, J. J. 2000, *Icarus*, 143, 2, doi: [10.1006/icar.1999.6246](https://doi.org/10.1006/icar.1999.6246)
- Bonfils, X., Delfosse, X., Udry, S., et al. 2005, *A&A*, 442, 635, doi: [10.1051/0004-6361:20053046](https://doi.org/10.1051/0004-6361:20053046)
- Brasser, R., Matsumura, S., Ida, S., Mojzsis, S. J., & Werner, S. C. 2016, *The Astrophysical Journal*, 821, 75, doi: [10.3847/0004-637X/821/2/7510.48550/arXiv.1603.01009](https://doi.org/10.3847/0004-637X/821/2/7510.48550/arXiv.1603.01009)
- Buchner, J., Georgakakis, A., Nandra, K., et al. 2014, *A&A*, 564, A125, doi: [10.1051/0004-6361/201322971](https://doi.org/10.1051/0004-6361/201322971)
- Burn, R., Schlecker, M., Mordasini, C., et al. 2021, *A&A*, 656, A72, doi: [10.1051/0004-6361/202140390](https://doi.org/10.1051/0004-6361/202140390)
- Burrows, A., Hubeny, I., Budaj, J., & Hubbard, W. B. 2007, *ApJ*, 661, 502, doi: [10.1086/514326](https://doi.org/10.1086/514326)
- Bushouse, H., Eisenhamer, J., Dencheva, N., et al. 2023, *JWST Calibration Pipeline*, 1.11.4, Zenodo, doi: [10.5281/zenodo.8247246](https://doi.org/10.5281/zenodo.8247246)
- Cañas, C. I., Kanodia, S., Bender, C. F., et al. 2022, *The Astronomical Journal*, 164, 50, doi: [10.3847/1538-3881/ac7804](https://doi.org/10.3847/1538-3881/ac7804)
- Cañas, C. I., Kanodia, S., Libby-Roberts, J., et al. 2023, *The Astronomical Journal*, 166, 30, doi: [10.3847/1538-3881/acdac7](https://doi.org/10.3847/1538-3881/acdac7)
- Chabrier, G., Mazevet, S., & Soubiran, F. 2019, *ApJ*, 872, 51, doi: [10.3847/1538-4357/aaf99f](https://doi.org/10.3847/1538-4357/aaf99f)
- Cushing, M. C., Vacca, W. D., & Rayner, J. T. 2004, *PASP*, 116, 362, doi: [10.1086/382907](https://doi.org/10.1086/382907)
- Dawson, R. I., & Johnson, J. A. 2018, *Annual Review of Astronomy and Astrophysics*, 56, 175, doi: [10.1146/annurev-astro-081817-051853](https://doi.org/10.1146/annurev-astro-081817-051853)
- Debras, F., & Chabrier, G. 2019, *ApJ*, 872, 100, doi: [10.3847/1538-4357/aaff65](https://doi.org/10.3847/1538-4357/aaff65)
- Delamer, M., Kanodia, S., Cañas, C. I., et al. 2024, *The Astrophysical Journal*, 962, L22, doi: [10.3847/2041-8213/ad1a19](https://doi.org/10.3847/2041-8213/ad1a19)
- Dittmann, J. A., Irwin, J. M., Charbonneau, D., & Newton, E. R. 2016, *ApJ*, 818, 153, doi: [10.3847/0004-637X/818/2/153](https://doi.org/10.3847/0004-637X/818/2/153)
- Edwards, B., Changeat, Q., Tsiaras, A., et al. 2023, *Characterising a World Within the Hot Neptune Desert: Transit Observations of LTT 9779 b with HST WFC3*, arXiv, doi: [10.48550/arXiv.2306.13645](https://doi.org/10.48550/arXiv.2306.13645)
- Espinoza, N., Rackham, B. V., Jordán, A., et al. 2019, *MNRAS*, 482, 2065, doi: [10.1093/mnras/sty2691](https://doi.org/10.1093/mnras/sty2691)
- Espinoza, N., Úbeda, L., Birkmann, S. M., et al. 2023, *PASP*, 135, 018002, doi: [10.1088/1538-3873/aca3d3](https://doi.org/10.1088/1538-3873/aca3d3)
- Feroz, F., Hobson, M. P., & Bridges, M. 2009, *MNRAS*, 398, 1601, doi: [10.1111/j.1365-2966.2009.14548.x](https://doi.org/10.1111/j.1365-2966.2009.14548.x)
- Fortney, J. J., Dawson, R. I., & Komacek, T. D. 2021, *Journal of Geophysical Research (Planets)*, 126, e06629, doi: [10.1029/2020JE006629](https://doi.org/10.1029/2020JE006629)
- Fortney, J. J., Marley, M. S., & Barnes, J. W. 2007, *ApJ*, 659, 1661, doi: [10.1086/512120](https://doi.org/10.1086/512120)
- Fortney, J. J., Mordasini, C., Nettelmann, N., et al. 2013, *ApJ*, 775, 80, doi: [10.1088/0004-637X/775/1/80](https://doi.org/10.1088/0004-637X/775/1/80)
- Fortney, J. J., Visscher, C., Marley, M. S., et al. 2020, *AJ*, 160, 288, doi: [10.3847/1538-3881/abc5bd](https://doi.org/10.3847/1538-3881/abc5bd)
- Fournier-Tondreau, M., MacDonald, R. J., Radica, M., et al. 2024, *MNRAS*, 528, 3354, doi: [10.1093/mnras/stad3813](https://doi.org/10.1093/mnras/stad3813)
- France, K., Loyd, R. O. P., Youngblood, A., et al. 2016, *ApJ*, 820, 89, doi: [10.3847/0004-637X/820/2/89](https://doi.org/10.3847/0004-637X/820/2/89)
- Freedman, R. S., Marley, M. S., & Lodders, K. 2008, *ApJS*, 174, 504, doi: [10.1086/521793](https://doi.org/10.1086/521793)
- Gao, P., & Ohno, K. 2024, arXiv e-prints, arXiv:2411.12031, doi: [10.48550/arXiv.2411.12031](https://doi.org/10.48550/arXiv.2411.12031)
- Gao, P., Wakeford, H. R., Moran, S. E., & Parmentier, V. 2021, *Journal of Geophysical Research (Planets)*, 126, e06655, doi: [10.1029/2020JE006655](https://doi.org/10.1029/2020JE006655)
- Gao, P., Thorngren, D. P., Lee, E. K. H., et al. 2020, *Nature Astronomy*, 4, 951, doi: [10.1038/s41550-020-1114-3](https://doi.org/10.1038/s41550-020-1114-3)
- Gasman, D., Min, M., & Chubb, K. L. 2022, *A&A*, 659, A114, doi: [10.1051/0004-6361/202141468](https://doi.org/10.1051/0004-6361/202141468)
- Gharib-Nezhad, E., Iyer, A. R., Line, M. R., et al. 2021, *ApJS*, 254, 34, doi: [10.3847/1538-4365/abf504](https://doi.org/10.3847/1538-4365/abf504)
- Ginsburg, A., Sipőcz, B. M., Brasseur, C. E., et al. 2019, *AJ*, 157, 98, doi: [10.3847/1538-3881/aafc33](https://doi.org/10.3847/1538-3881/aafc33)

- Goukenleuque, C., Bézard, B., & Lellouch, E. 2000, in *Astronomical Society of the Pacific Conference Series*, Vol. 212, *From Giant Planets to Cool Stars*, ed. C. A. Griffith & M. S. Marley, 242
- Grant, D., & Wakeford, H. R. 2024, *Journal of Open Source Software*, 9, 6816, doi: [10.21105/joss.06816](https://doi.org/10.21105/joss.06816)
- Guillot, T. 2010, *A&A*, 520, A27, doi: [10.1051/0004-6361/200913396](https://doi.org/10.1051/0004-6361/200913396)
- Guillot, T., Fletcher, L. N., Helled, R., et al. 2023, in *Astronomical Society of the Pacific Conference Series*, Vol. 534, *Protostars and Planets VII*, ed. S. Inutsuka, Y. Aikawa, T. Muto, K. Tomida, & M. Tamura, 947
- Guillot, T., & Gautier, D. 2015, in *Treatise on Geophysics (Second Edition)*, second edition edn., ed. G. Schubert (Oxford: Elsevier), 529–557, doi: <https://doi.org/10.1016/B978-0-444-53802-4.00176-7>
- Guillot, T., Santos, N. C., Pont, F., et al. 2006, *A&A*, 453, L21, doi: [10.1051/0004-6361:20065476](https://doi.org/10.1051/0004-6361:20065476)
- Han, T., & Brandt, T. D. 2023, *AJ*, 165, 71, doi: [10.3847/1538-3881/acaaa7](https://doi.org/10.3847/1538-3881/acaaa7)
- Hardegree-Ullman, K. K., Zink, J. K., Christiansen, J. L., et al. 2020, *ApJS*, 247, 28, doi: [10.3847/1538-4365/ab7230](https://doi.org/10.3847/1538-4365/ab7230)
- Hartman, J. D., Bayliss, D., Brahm, R., et al. 2015, *The Astronomical Journal*, 149, 166, doi: [10.1088/0004-6256/149/5/166](https://doi.org/10.1088/0004-6256/149/5/166)
- Hasegawa, Y., Bryden, G., Ikoma, M., Vasisht, G., & Swain, M. 2018, *ApJ*, 865, 32, doi: [10.3847/1538-4357/aad912](https://doi.org/10.3847/1538-4357/aad912)
- Hasegawa, Y., & Swain, M. R. 2024, arXiv e-prints, arXiv:2409.06670, doi: [10.48550/arXiv.2409.06670](https://doi.org/10.48550/arXiv.2409.06670)
- Helled, R., & Howard, S. 2024, arXiv e-prints, arXiv:2407.05853, doi: [10.48550/arXiv.2407.05853](https://doi.org/10.48550/arXiv.2407.05853)
- Herbst, K., Papaioannou, A., Airapetian, V. S., & Atri, D. 2021, *ApJ*, 907, 89, doi: [10.3847/1538-4357/abcc04](https://doi.org/10.3847/1538-4357/abcc04)
- Holmberg, M., & Madhusudhan, N. 2024, *A&A*, 683, L2, doi: [10.1051/0004-6361/202348238](https://doi.org/10.1051/0004-6361/202348238)
- Horne, K. 1986, *Publications of the Astronomical Society of the Pacific*, 98, 609, doi: [10.1086/131801](https://doi.org/10.1086/131801)
- Hörst, S. M. 2017, *Journal of Geophysical Research (Planets)*, 122, 432, doi: [10.1002/2016JE005240](https://doi.org/10.1002/2016JE005240)
- Howard, S., & Guillot, T. 2023, *A&A*, 672, L1, doi: [10.1051/0004-6361/202244851](https://doi.org/10.1051/0004-6361/202244851)
- Howard, S., Guillot, T., Markham, S., et al. 2023, *A&A*, 680, L2, doi: [10.1051/0004-6361/202348129](https://doi.org/10.1051/0004-6361/202348129)
- Huehnerhoff, J., Ketzbeck, W., Bradley, A., et al. 2016, in *Society of Photo-Optical Instrumentation Engineers (SPIE) Conference Series*, Vol. 9908, *Ground-based and Airborne Instrumentation for Astronomy VI*, ed. C. J. Evans, L. Simard, & H. Takami, 99085H, doi: [10.1117/12.2234214](https://doi.org/10.1117/12.2234214)
- Hunter, J. D. 2007, *Computing In Science & Engineering*, 9, 90, doi: [10.1109/MCSE.2007.55](https://doi.org/10.1109/MCSE.2007.55)
- Husser, T. O., Wende-von Berg, S., Dreizler, S., et al. 2013, *A&A*, 553, A6, doi: [10.1051/0004-6361/201219058](https://doi.org/10.1051/0004-6361/201219058)
- Ikoma, M., Nakazawa, K., & Emori, H. 2000, *ApJ*, 537, 1013, doi: [10.1086/309050](https://doi.org/10.1086/309050)
- Iyer, A. R., Swain, M. R., Zellem, R. T., et al. 2016, *ApJ*, 823, 109, doi: [10.3847/0004-637X/823/2/109](https://doi.org/10.3847/0004-637X/823/2/109)
- Jackson, J. M., Dawson, R. I., Quarles, B., & Dong, J. 2022, *Statistical Analysis of the Dearth of Super-eccentric Jupiters in the Kepler Sample*, arXiv, doi: [10.48550/arXiv.2212.07546](https://doi.org/10.48550/arXiv.2212.07546)
- Jermyn, A. S., Bauer, E. B., Schwab, J., et al. 2023, *ApJS*, 265, 15, doi: [10.3847/1538-4365/acae8d](https://doi.org/10.3847/1538-4365/acae8d)
- Johansen, A., & Lambrechts, M. 2017, *Annual Review of Earth and Planetary Sciences*, 45, 359, doi: [10.1146/annurev-earth-063016-020226](https://doi.org/10.1146/annurev-earth-063016-020226)
- Johnson, J. A., Gazak, J. Z., Apps, K., et al. 2012, *AJ*, 143, 111, doi: [10.1088/0004-6256/143/5/111](https://doi.org/10.1088/0004-6256/143/5/111)
- Jordán, A., Hartman, J. D., Bayliss, D., et al. 2022, *The Astronomical Journal*, 163, 125, doi: [10.3847/1538-3881/ac4a77](https://doi.org/10.3847/1538-3881/ac4a77)
- Kanodia, S., Libby-Roberts, J., Cañas, C. I., et al. 2022, *The Astronomical Journal*, 164, 81, doi: [10.3847/1538-3881/ac7c20](https://doi.org/10.3847/1538-3881/ac7c20)
- Kanodia, S., Mahadevan, S., Libby-Roberts, J., et al. 2023, *AJ*, 165, 120, doi: [10.3847/1538-3881/acabce](https://doi.org/10.3847/1538-3881/acabce)
- Kanodia, S., Canas, C., Libby-Roberts, J., et al. 2023, *Red Dwarfs and the Seven Giants: First Insights into the Atmospheres of Giant Exoplanets around M-dwarf Stars*, JWST Proposal. Cycle 2, ID. #3171
- Kanodia, S., Cañas, C. I., Mahadevan, S., et al. 2024, *The Astronomical Journal*, 167, 161, doi: [10.3847/1538-3881/ad27cb](https://doi.org/10.3847/1538-3881/ad27cb)
- Kawashima, Y., & Ikoma, M. 2019, *ApJ*, 884, 98, doi: [10.3847/1538-4357/ab442a](https://doi.org/10.3847/1538-4357/ab442a)
- Kempton, E. M. R., & Knutson, H. A. 2024, *Reviews in Mineralogy and Geochemistry*, 90, 411, doi: [10.2138/rmg.2024.90.12](https://doi.org/10.2138/rmg.2024.90.12)
- Kiefer, S., Bach-Møller, N., Samra, D., et al. 2024, arXiv e-prints, arXiv:2410.17716, doi: [10.48550/arXiv.2410.17716](https://doi.org/10.48550/arXiv.2410.17716)
- Kipping, D. M. 2012, *MNRAS*, 427, 2487, doi: [10.1111/j.1365-2966.2012.22124.x](https://doi.org/10.1111/j.1365-2966.2012.22124.x)
- . 2013, *MNRAS*, 435, 2152, doi: [10.1093/mnras/stt1435](https://doi.org/10.1093/mnras/stt1435)
- Knierim, H., & Helled, R. 2024, arXiv e-prints, arXiv:2407.09341, doi: [10.48550/arXiv.2407.09341](https://doi.org/10.48550/arXiv.2407.09341)
- Kostogryz, N. M., Witzke, V., Shapiro, A. I., et al. 2022, *A&A*, 666, A60, doi: [10.1051/0004-6361/202243722](https://doi.org/10.1051/0004-6361/202243722)

- Kostogryz, N. M., Shapiro, A. I., Witzke, V., et al. 2024, *Nature Astronomy*, 8, 929, doi: [10.1038/s41550-024-02252-5](https://doi.org/10.1038/s41550-024-02252-5)
- Kurokawa, H., & Inutsuka, S.-i. 2015, *ApJ*, 815, 78, doi: [10.1088/0004-637X/815/1/78](https://doi.org/10.1088/0004-637X/815/1/78)
- Kurucz, R. 1993, Robert Kurucz CD-ROM, 13
- Kurucz, R. L. 1970, SAO Special Report, 309
- Laughlin, G., Bodenheimer, P., & Adams, F. C. 2004, *ApJL*, 612, L73, doi: [10.1086/424384](https://doi.org/10.1086/424384)
- Lecavelier Des Etangs, A., Pont, F., Vidal-Madjar, A., & Sing, D. 2008, *A&A*, 481, L83, doi: [10.1051/0004-6361/200809388](https://doi.org/10.1051/0004-6361/200809388)
- Liang, M.-C., Seager, S., Parkinson, C. D., Lee, A. Y. T., & Yung, Y. L. 2004, *ApJL*, 605, L61, doi: [10.1086/392509](https://doi.org/10.1086/392509)
- Libby-Roberts, J. E., Schutte, M., Hebb, L., et al. 2023, arXiv e-prints, arXiv:2302.04757, doi: [10.48550/arXiv.2302.04757](https://doi.org/10.48550/arXiv.2302.04757)
- Lightkurve Collaboration, Cardoso, J. V. d. M. a., Hedges, C., et al. 2018, Lightkurve: Kepler and TESS time series analysis in Python. <http://ascl.net/1812.013>
- Lim, O., Benneke, B., Doyon, R., et al. 2023, *ApJL*, 955, L22, doi: [10.3847/2041-8213/acf7c4](https://doi.org/10.3847/2041-8213/acf7c4)
- Line, M. R., Liang, M. C., & Yung, Y. L. 2010, *ApJ*, 717, 496, doi: [10.1088/0004-637X/717/1/496](https://doi.org/10.1088/0004-637X/717/1/496)
- Line, M. R., Vasisht, G., Chen, P., Angerhausen, D., & Yung, Y. L. 2011, *ApJ*, 738, 32, doi: [10.1088/0004-637X/738/1/32](https://doi.org/10.1088/0004-637X/738/1/32)
- Lodders, K., & Fegley, B. 2002, *Icarus*, 155, 393, doi: [10.1006/icar.2001.6740](https://doi.org/10.1006/icar.2001.6740)
- Long, F., Pascucci, I., Houge, A., et al. 2024, arXiv e-prints, arXiv:2412.05535. <https://arxiv.org/abs/2412.05535>
- Loyd, R. O. P., France, K., Youngblood, A., et al. 2016, *ApJ*, 824, 102, doi: [10.3847/0004-637X/824/2/102](https://doi.org/10.3847/0004-637X/824/2/102)
- Luger, R., Foreman-Mackey, D., & Hedges, C. 2021, *The Journal of Open Source Software*, 6, 3071, doi: [10.21105/joss.03071](https://doi.org/10.21105/joss.03071)
- Lupu, R., Freedman, R., Gharib-Nezhad, E., Visscher, C., & Molliere, P. 2023, Correlated k coefficients for H2-He atmospheres; 196 spectral windows and 1460 pressure-temperature points, Zenodo, doi: [10.5281/zenodo.7542068](https://doi.org/10.5281/zenodo.7542068)
- MacDonald, R. J. 2023, *Journal of Open Source Software*, 8, 4873, doi: [10.21105/joss.04873](https://doi.org/10.21105/joss.04873)
- MacDonald, R. J., & Madhusudhan, N. 2017, *MNRAS*, 469, 1979, doi: [10.1093/mnras/stx804](https://doi.org/10.1093/mnras/stx804)
- . 2019, *MNRAS*, 486, 1292, doi: [10.1093/mnras/stz789](https://doi.org/10.1093/mnras/stz789)
- Madhusudhan, N. 2018, in *Handbook of Exoplanets*, ed. H. J. Deeg & J. A. Belmonte, 104, doi: [10.1007/978-3-319-55333-7_104](https://doi.org/10.1007/978-3-319-55333-7_104)
- Magic, Z., Chiavassa, A., Collet, R., & Asplund, M. 2015, *Astronomy & Astrophysics*, 573, A90
- Mah, J., Bitsch, B., Pascucci, I., & Henning, T. 2023, *A&A*, 677, L7, doi: [10.1051/0004-6361/202347169](https://doi.org/10.1051/0004-6361/202347169)
- Mandt K., E., Luspay-Kuti, A., A., C., -L., J. K., & P, G. 2023, arXiv e-prints, arXiv:2311.17235, doi: [10.48550/arXiv.2311.17235](https://doi.org/10.48550/arXiv.2311.17235)
- Mann, A. W., Brewer, J. M., Gaidos, E., Lépine, S., & Hilton, E. J. 2013, *AJ*, 145, 52, doi: [10.1088/0004-6256/145/2/52](https://doi.org/10.1088/0004-6256/145/2/52)
- Marley, M. S., Saumon, D., Visscher, C., et al. 2021, *ApJ*, 920, 85, doi: [10.3847/1538-4357/ac141d](https://doi.org/10.3847/1538-4357/ac141d)
- May, E. M., Gardner, T., Rauscher, E., & Monnier, J. D. 2018, arXiv e-prints, arXiv:1809.10211, doi: [10.48550/arXiv.1809.10211](https://doi.org/10.48550/arXiv.1809.10211)
- May, E. M., MacDonald, R. J., Bennett, K. A., et al. 2023, *ApJL*, 959, L9, doi: [10.3847/2041-8213/ad054f](https://doi.org/10.3847/2041-8213/ad054f)
- Mayor, M., & Queloz, D. 1995, *Nature*, 378, 355, doi: [10.1038/378355a0](https://doi.org/10.1038/378355a0)
- McKinney, W. 2010, in *Proceedings of the 9th Python in Science Conference*, ed. S. van der Walt & J. Millman, 51 – 56
- Miller, N., & Fortney, J. J. 2011, *ApJL*, 736, L29, doi: [10.1088/2041-8205/736/2/L29](https://doi.org/10.1088/2041-8205/736/2/L29)
- Molaverdikhani, K., Henning, T., & Mollière, P. 2019, *ApJ*, 883, 194, doi: [10.3847/1538-4357/ab3e30](https://doi.org/10.3847/1538-4357/ab3e30)
- Mollière, P., Molyarova, T., Bitsch, B., et al. 2022, *The Astrophysical Journal*, 934, 74, doi: [10.3847/1538-4357/ac6a56](https://doi.org/10.3847/1538-4357/ac6a56)
- Morales, J. C., Mustill, A. J., Ribas, I., et al. 2019, *Science*, 365, 1441, doi: [10.1126/science.aax3198](https://doi.org/10.1126/science.aax3198)
- Moran, S. E., Stevenson, K. B., Sing, D. K., et al. 2023, *ApJL*, 948, L11, doi: [10.3847/2041-8213/accb9c](https://doi.org/10.3847/2041-8213/accb9c)
- Mordasini, C., Klahr, H., Alibert, Y., Miller, N., & Henning, T. 2014, *A&A*, 566, A141, doi: [10.1051/0004-6361/201321479](https://doi.org/10.1051/0004-6361/201321479)
- More, R. M., Warren, K. H., Young, D. A., & Zimmerman, G. B. 1988, *Physics of Fluids*, 31, 3059, doi: [10.1063/1.866963](https://doi.org/10.1063/1.866963)
- Mori, M., Ikuta, K., Fukui, A., et al. 2024, *MNRAS*, 530, 167, doi: [10.1093/mnras/stae841](https://doi.org/10.1093/mnras/stae841)
- Morley, C. V., Fortney, J. J., Marley, M. S., et al. 2015, *ApJ*, 815, 110, doi: [10.1088/0004-637X/815/2/110](https://doi.org/10.1088/0004-637X/815/2/110)
- Morris, B. M. 2022, fleck: Fast starspot rotational modulation light curves, *Astrophysics Source Code Library*, record ascl:2203.009

- Moseley, S. H., Arendt, R. G., Fixsen, D. J., et al. 2010, in Society of Photo-Optical Instrumentation Engineers (SPIE) Conference Series, Vol. 7742, High Energy, Optical, and Infrared Detectors for Astronomy IV, ed. A. D. Holland & D. A. Dorn, 77421B, doi: [10.1117/12.866773](https://doi.org/10.1117/12.866773)
- Mousis, O., Marboeuf, U., Lunine, J. I., et al. 2009, *ApJ*, 696, 1348, doi: [10.1088/0004-637X/696/2/1348](https://doi.org/10.1088/0004-637X/696/2/1348)
- Movshovitz, N., Bodenheimer, P., Podolak, M., & Lissauer, J. J. 2010, *Icarus*, 209, 616, doi: [10.1016/j.icarus.2010.06.009](https://doi.org/10.1016/j.icarus.2010.06.009)
- Mukherjee, S., Batalha, N. E., Fortney, J. J., & Marley, M. S. 2023, *ApJ*, 942, 71, doi: [10.3847/1538-4357/ac9f48](https://doi.org/10.3847/1538-4357/ac9f48)
- Mukherjee, S., Fortney, J. J., Wogan, N. F., Sing, D. K., & Ohno, K. 2024, arXiv e-prints, arXiv:2410.17169, doi: [10.48550/arXiv.2410.17169](https://doi.org/10.48550/arXiv.2410.17169)
- Mulders, G. D., Drazkowska, J., van der Marel, N., Ciesla, F. J., & Pascucci, I. 2021, *ApJ*, 920, L1, doi: [10.3847/2041-8213/ac2947](https://doi.org/10.3847/2041-8213/ac2947)
- Müller, S., Ben-Yami, M., & Helled, R. 2020a, *ApJ*, 903, 147, doi: [10.3847/1538-4357/abba19](https://doi.org/10.3847/1538-4357/abba19)
- Müller, S., & Helled, R. 2021, *Monthly Notices of the Royal Astronomical Society*, 507, 2094, doi: [10.1093/mnras/stab2250](https://doi.org/10.1093/mnras/stab2250)
- Müller, S., & Helled, R. 2023a, *A&A*, 669, A24, doi: [10.1051/0004-6361/202244827](https://doi.org/10.1051/0004-6361/202244827)
- . 2023b, *Frontiers in Astronomy and Space Sciences*, 10, 1179000, doi: [10.3389/fspas.2023.1179000](https://doi.org/10.3389/fspas.2023.1179000)
- . 2024a, arXiv e-prints, arXiv:2411.16197, doi: [10.48550/arXiv.2411.16197](https://doi.org/10.48550/arXiv.2411.16197)
- . 2024b, *ApJ*, 967, 7, doi: [10.3847/1538-4357/ad3738](https://doi.org/10.3847/1538-4357/ad3738)
- Müller, S., Helled, R., & Cumming, A. 2020b, *A&A*, 638, A121, doi: [10.1051/0004-6361/201937376](https://doi.org/10.1051/0004-6361/201937376)
- Neves, V., Bonfils, X., Santos, N. C., et al. 2012, *A&A*, 538, A25, doi: [10.1051/0004-6361/201118115](https://doi.org/10.1051/0004-6361/201118115)
- Norris, C. M., Unruh, Y. C., Witzke, V., et al. 2023, *MNRAS*, 524, 1139, doi: [10.1093/mnras/stad1738](https://doi.org/10.1093/mnras/stad1738)
- Öberg, K. I., Murray-Clay, R., & Bergin, E. A. 2011, *ApJL*, 743, L16, doi: [10.1088/2041-8205/743/1/L16](https://doi.org/10.1088/2041-8205/743/1/L16)
- Ohno, K., & Fortney, J. J. 2023a, *ApJ*, 946, 18, doi: [10.3847/1538-4357/acafed](https://doi.org/10.3847/1538-4357/acafed)
- . 2023b, *ApJ*, 956, 125, doi: [10.3847/1538-4357/ace531](https://doi.org/10.3847/1538-4357/ace531)
- Ohno, K., & Kawashima, Y. 2020, *ApJL*, 895, L47, doi: [10.3847/2041-8213/ab93d7](https://doi.org/10.3847/2041-8213/ab93d7)
- Pacetti, E., Turrini, D., Schisano, E., et al. 2022, *ApJ*, 937, 36, doi: [10.3847/1538-4357/ac8b11](https://doi.org/10.3847/1538-4357/ac8b11)
- Pascucci, I., Testi, L., Herczeg, G. J., et al. 2016, *The Astrophysical Journal*, 831, 125, doi: [10.3847/0004-637X/831/2/125](https://doi.org/10.3847/0004-637X/831/2/125)
- Paxton, B., Bildsten, L., Dotter, A., et al. 2011, *ApJS*, 192, 3, doi: [10.1088/0067-0049/192/1/3](https://doi.org/10.1088/0067-0049/192/1/3)
- Paxton, B., Cantiello, M., Arras, P., et al. 2013, *ApJS*, 208, 4, doi: [10.1088/0067-0049/208/1/4](https://doi.org/10.1088/0067-0049/208/1/4)
- Paxton, B., Marchant, P., Schwab, J., et al. 2015, *ApJS*, 220, 15, doi: [10.1088/0067-0049/220/1/15](https://doi.org/10.1088/0067-0049/220/1/15)
- Paxton, B., Schwab, J., Bauer, E. B., et al. 2018, *ApJS*, 234, 34, doi: [10.3847/1538-4365/aaa5a8](https://doi.org/10.3847/1538-4365/aaa5a8)
- Paxton, B., Smolec, R., Schwab, J., et al. 2019, *ApJS*, 243, 10, doi: [10.3847/1538-4365/ab2241](https://doi.org/10.3847/1538-4365/ab2241)
- Perrin, M. D., Lallo, M., Telfer, R., et al. 2024, OTE Science Performance Memo 3: Detection and Correction of a Uniquely Large Mirror Shift during Cycle 2, Technical Report JWST-STScI-008650, 12 pages
- Pinhas, A., & Madhusudhan, N. 2017, *MNRAS*, 471, 4355, doi: [10.1093/mnras/stx1849](https://doi.org/10.1093/mnras/stx1849)
- Pinhas, A., Madhusudhan, N., Gandhi, S., & MacDonald, R. 2019, *MNRAS*, 482, 1485, doi: [10.1093/mnras/sty2544](https://doi.org/10.1093/mnras/sty2544)
- Polman, J., Waters, L. B. F. M., Min, M., Miguel, Y., & Khorshid, N. 2023, *A&A*, 670, A161, doi: [10.1051/0004-6361/202244647](https://doi.org/10.1051/0004-6361/202244647)
- Poser, A. J., Nettelmann, N., & Redmer, R. 2019, *Atmosphere*, 10, 664, doi: [10.3390/atmos10110664](https://doi.org/10.3390/atmos10110664)
- Quirrenbach, A., Passegger, V. M., Trifonov, T., et al. 2022, *A&A*, 663, A48, doi: [10.1051/0004-6361/202142915](https://doi.org/10.1051/0004-6361/202142915)
- Rackham, B., Espinoza, N., Apai, D., et al. 2017, *ApJ*, 834, 151, doi: [10.3847/1538-4357/aa4f6c](https://doi.org/10.3847/1538-4357/aa4f6c)
- Rackham, B. V., Apai, D., & Giampapa, M. S. 2018, *ApJ*, 853, 122, doi: [10.3847/1538-4357/aaa08c](https://doi.org/10.3847/1538-4357/aaa08c)
- Rackham, B. V., & de Wit, J. 2024, *AJ*, 168, 82, doi: [10.3847/1538-3881/ad5833](https://doi.org/10.3847/1538-3881/ad5833)
- Rackham, B. V., Espinoza, N., Berdyugina, S. V., et al. 2023, *RAS Techniques and Instruments*, 2, 148, doi: [10.1093/rasti/rzad009](https://doi.org/10.1093/rasti/rzad009)
- Radica, M., Piaulet-Ghorayeb, C., Taylor, J., et al. 2024, arXiv e-prints, arXiv:2409.19333, doi: [10.48550/arXiv.2409.19333](https://doi.org/10.48550/arXiv.2409.19333)
- Rajpurohit, A. S., Allard, F., Rajpurohit, S., et al. 2018, *A&A*, 620, A180, doi: [10.1051/0004-6361/201833500](https://doi.org/10.1051/0004-6361/201833500)
- Raymond, S. N., O'Brien, D. P., Morbidelli, A., & Kaib, N. A. 2009, *Icarus*, 203, 644, doi: [10.1016/j.icarus.2009.05.016](https://doi.org/10.1016/j.icarus.2009.05.016)
[10.48550/arXiv.0905.3750](https://doi.org/10.48550/arXiv.0905.3750)
- Rayner, J. T., Toomey, D. W., Onaka, P. M., et al. 2003, *PASP*, 115, 362, doi: [10.1086/367745](https://doi.org/10.1086/367745)
- Rice, M., Wang, S., & Laughlin, G. 2022, *Origins of Hot Jupiters from the Stellar Obliquity Distribution*
- Rojas-Ayala, B., Covey, K. R., Muirhead, P. S., & Lloyd, J. P. 2012, *ApJ*, 748, 93, doi: [10.1088/0004-637X/748/2/93](https://doi.org/10.1088/0004-637X/748/2/93)

- Rooney, C. M., Batalha, N. E., Gao, P., & Marley, M. S. 2022, *ApJ*, 925, 33, doi: [10.3847/1538-4357/ac307a](https://doi.org/10.3847/1538-4357/ac307a)
- Rustamkulov, Z., Sing, D. K., Mukherjee, S., et al. 2023, *Nature*, 614, 659, doi: [10.1038/s41586-022-05677-y](https://doi.org/10.1038/s41586-022-05677-y)
- Schlaufman, K. C., & Laughlin, G. 2010, *A&A*, 519, A105, doi: [10.1051/0004-6361/201015016](https://doi.org/10.1051/0004-6361/201015016)
- Schneider, A. D., & Bitsch, B. 2021, *A&A*, 654, A71, doi: [10.1051/0004-6361/202039640](https://doi.org/10.1051/0004-6361/202039640)
- Seager, S., & Shapiro, A. I. 2024, *ApJ*, 970, 155, doi: [10.3847/1538-4357/ad509a](https://doi.org/10.3847/1538-4357/ad509a)
- Sedaghati, E., Boffin, H. M. J., MacDonald, R. J., et al. 2017, *Nature*, 549, 238, doi: [10.1038/nature23651](https://doi.org/10.1038/nature23651)
- Shibata, S., Helled, R., & Ikoma, M. 2020, *A&A*, 633, A33, doi: [10.1051/0004-6361/201936700](https://doi.org/10.1051/0004-6361/201936700)
- Shibata, S., & Ikoma, M. 2019, *MNRAS*, 487, 4510, doi: [10.1093/mnras/stz1629](https://doi.org/10.1093/mnras/stz1629)
- Sing, D. K., Fortney, J. J., Nikolov, N., et al. 2016, *Nature*, 529, 59, doi: [10.1038/nature16068](https://doi.org/10.1038/nature16068)
- Sing, D. K., Rustamkulov, Z., Thorngren, D. P., et al. 2024, *Nature*, 630, 831, doi: [10.1038/s41586-024-07395-z](https://doi.org/10.1038/s41586-024-07395-z)
- Smitha, H. N., Shapiro, A. I., Witzke, V., et al. 2024, arXiv e-prints, arXiv:2411.14056, doi: [10.48550/arXiv.2411.14056](https://doi.org/10.48550/arXiv.2411.14056)
- Speagle, J. S. 2020, *MNRAS*, 493, 3132, doi: [10.1093/mnras/staa278](https://doi.org/10.1093/mnras/staa278)
- Stock, J. W., Kitzmann, D., Patzer, A. B. C., & Sedlmayr, E. 2018, *MNRAS*, 479, 865, doi: [10.1093/mnras/sty1531](https://doi.org/10.1093/mnras/sty1531)
- STScI Development Team. 2013, pynphot: Synthetic photometry software package, Astrophysics Source Code Library, record ascl:1303.023
- Sun, Q., Wang, S. X., Welbanks, L., Teske, J., & Buchner, J. 2024, *AJ*, 167, 167, doi: [10.3847/1538-3881/ad298d](https://doi.org/10.3847/1538-3881/ad298d)
- Swain, M. R., Hasegawa, Y., Thorngren, D. P., & Roudier, G. M. 2024, *SSRv*, 220, 61, doi: [10.1007/s11214-024-01098-7](https://doi.org/10.1007/s11214-024-01098-7)
- Tabone, B., Bettoni, G., van Dishoeck, E. F., et al. 2023, *Nature Astronomy*, 7, 805, doi: [10.1038/s41550-023-01965-3](https://doi.org/10.1038/s41550-023-01965-3)
- Thorngren, D., & Fortney, J. J. 2019, *The Astrophysical Journal*, 874, L31, doi: [10.3847/2041-8213/ab1137](https://doi.org/10.3847/2041-8213/ab1137)
- Thorngren, D. P., Fortney, J. J., Murray-Clay, R. A., & Lopez, E. D. 2016, *The Astrophysical Journal*, 831, 64, doi: [10.3847/0004-637X/831/1/64](https://doi.org/10.3847/0004-637X/831/1/64)
- TRAPPIST-1 JWST Community Initiative, de Wit, J., Doyon, R., et al. 2024, *Nature Astronomy*, 8, 810, doi: [10.1038/s41550-024-02298-5](https://doi.org/10.1038/s41550-024-02298-5)
- Trotta, R. 2008, *Contemporary Physics*, 49, 71, doi: [10.1080/00107510802066753](https://doi.org/10.1080/00107510802066753)
- Tsai, S.-M., Lyons, J. R., Grosheintz, L., et al. 2017, *Astrophys. J. Suppl. Ser.*, 228, 1, doi: [10.3847/1538-4365/228/2/20](https://doi.org/10.3847/1538-4365/228/2/20)
- Tsai, S.-M., Malik, M., Kitzmann, D., et al. 2021, *The Astrophysical Journal*, 923, 264, doi: [10.3847/1538-4357/ac29bc](https://doi.org/10.3847/1538-4357/ac29bc)
- Tsai, S.-M., Lee, E. K. H., Powell, D., et al. 2023, *Nature*, 617, 483, doi: [10.1038/s41586-023-05902-2](https://doi.org/10.1038/s41586-023-05902-2)
- Turrini, D., Schisano, E., Fonte, S., et al. 2021, *ApJ*, 909, 40, doi: [10.3847/1538-4357/abd6e5](https://doi.org/10.3847/1538-4357/abd6e5)
- Vacca, W. D., Cushing, M. C., & Rayner, J. T. 2003, *PASP*, 115, 389, doi: [10.1086/346193](https://doi.org/10.1086/346193)
- van der Walt, S., Colbert, S. C., & Varoquaux, G. 2011, *Computing in Science and Engineering*, 13, 22, doi: [10.1109/MCSE.2011.37](https://doi.org/10.1109/MCSE.2011.37)
- Vazan, A., Helled, R., & Guillot, T. 2018, *A&A*, 610, L14, doi: [10.1051/0004-6361/201732522](https://doi.org/10.1051/0004-6361/201732522)
- Venot, O., Hébrard, E., Agúndez, M., Decin, L., & Bounaceur, R. 2015, *A&A*, 577, A33, doi: [10.1051/0004-6361/201425311](https://doi.org/10.1051/0004-6361/201425311)
- Venot, O., Parmentier, V., Blečić, J., et al. 2020, *ApJ*, 890, 176, doi: [10.3847/1538-4357/ab6a94](https://doi.org/10.3847/1538-4357/ab6a94)
- Virtanen, P., Gommers, R., Oliphant, T. E., et al. 2020, *Nature Methods*, 17, 261, doi: [10.1038/s41592-019-0686-2](https://doi.org/10.1038/s41592-019-0686-2)
- Waalkes, W. C., Berta-Thompson, Z. K., Newton, E. R., et al. 2024, *ApJ*, 962, 97, doi: [10.3847/1538-4357/ad0bed](https://doi.org/10.3847/1538-4357/ad0bed)
- Wang, D., Miguel, Y., & Lunine, J. 2017, *ApJ*, 850, 199, doi: [10.3847/1538-4357/aa978e](https://doi.org/10.3847/1538-4357/aa978e)
- Welbanks, L., & Madhusudhan, N. 2019, *AJ*, 157, 206, doi: [10.3847/1538-3881/ab14de](https://doi.org/10.3847/1538-3881/ab14de)
- Welbanks, L., Madhusudhan, N., Allard, N. F., et al. 2019, *ApJ*, 887, L20, doi: [10.3847/2041-8213/ab5a89](https://doi.org/10.3847/2041-8213/ab5a89)
- Welbanks, L., Bell, T. J., Beatty, T. G., et al. 2024, *Nature*, 630, 836, doi: [10.1038/s41586-024-07514-w](https://doi.org/10.1038/s41586-024-07514-w)
- Winn, J. N. 2010, in *Exoplanets*, ed. S. Seager, 55–77, doi: [10.48550/arXiv.1001.2010](https://doi.org/10.48550/arXiv.1001.2010)
- Witzke, V., Shapiro, A. I., Kostogryz, N. M., et al. 2022, *ApJL*, 941, L35, doi: [10.3847/2041-8213/aca671](https://doi.org/10.3847/2041-8213/aca671)
- . 2024, *A&A*, 681, A81, doi: [10.1051/0004-6361/202346099](https://doi.org/10.1051/0004-6361/202346099)
- Wu, D.-H., Rice, M., & Wang, S. 2023, *AJ*, 165, 171, doi: [10.3847/1538-3881/acbf3f](https://doi.org/10.3847/1538-3881/acbf3f)
- Xie, C., Pascucci, I., Long, F., et al. 2023, *ApJL*, 959, L25, doi: [10.3847/2041-8213/ad0ed9](https://doi.org/10.3847/2041-8213/ad0ed9)
- Yee, S. W., Petigura, E. A., & von Braun, K. 2017, *ApJ*, 836, 77, doi: [10.3847/1538-4357/836/1/77](https://doi.org/10.3847/1538-4357/836/1/77)
- Youngblood, A., France, K., Loyd, R. O. P., et al. 2016, *ApJ*, 824, 101, doi: [10.3847/0004-637X/824/2/101](https://doi.org/10.3847/0004-637X/824/2/101)

Zahnle, K., Marley, M. S., Freedman, R. S., Lodders, K., &

Fortney, J. J. 2009, *ApJL*, 701, L20,

doi: [10.1088/0004-637X/701/1/L20](https://doi.org/10.1088/0004-637X/701/1/L20)

Zhang, M., Chachan, Y., Kempton, E. M. R., & Knutson,
H. A. 2019, *PASP*, 131, 034501,

doi: [10.1088/1538-3873/aaf5ad](https://doi.org/10.1088/1538-3873/aaf5ad)

Zhang, M., Chachan, Y., Kempton, E. M. R., Knutson,

H. A., & Chang, W. H. 2020, *ApJ*, 899, 27,

doi: [10.3847/1538-4357/aba1e6](https://doi.org/10.3847/1538-4357/aba1e6)

Zhang, X. 2024, arXiv e-prints, arXiv:2410.04595,

doi: [10.48550/arXiv.2410.04595](https://doi.org/10.48550/arXiv.2410.04595)

Fig. Set 5. Retrieval Results for individual visits

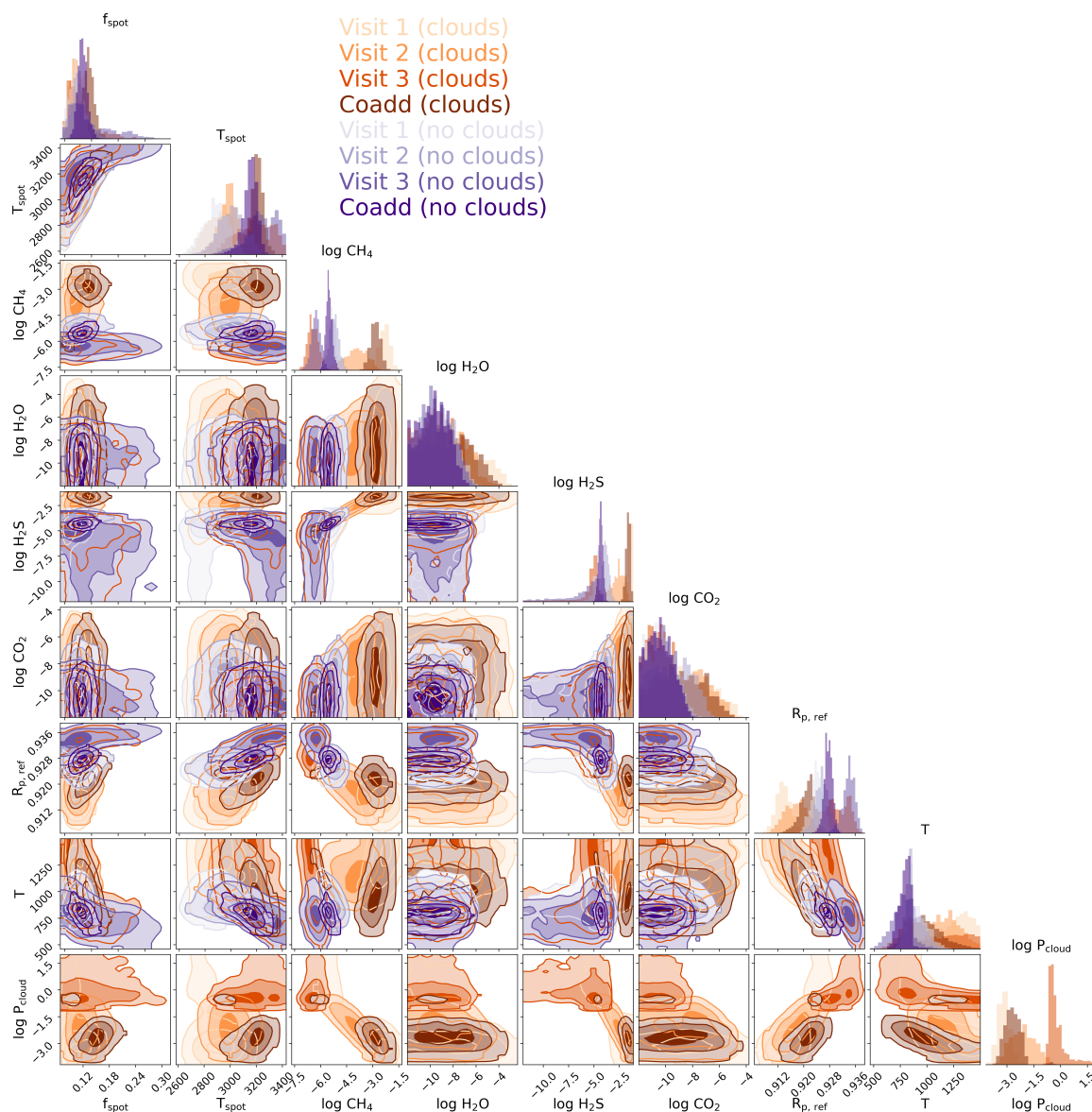


Fig. Set 5.1 – Overview. Posterior probability distributions (1- and 2-D) for a subset of retrieval parameters showing constraints obtained from different visits and simulations with and without clouds (colors). When clouds are included in the retrieval, significant visit-to-visit variability is seen among the retrieved atmospheric parameters, particularly temperature, cloud-top pressure, and the CH_4 abundance. When clouds are neglected, the three visits converge to a consistent atmospheric interpretation. *Individual visit analyses do not reveal the full extent of the correlations that exist between retrieval parameters. Comparing multiple visits illuminates the covariances along which the visits appear discrepant.* The complete figure set (9 images, for the 8 individual figures plus one combined figure) is available in the online journal.

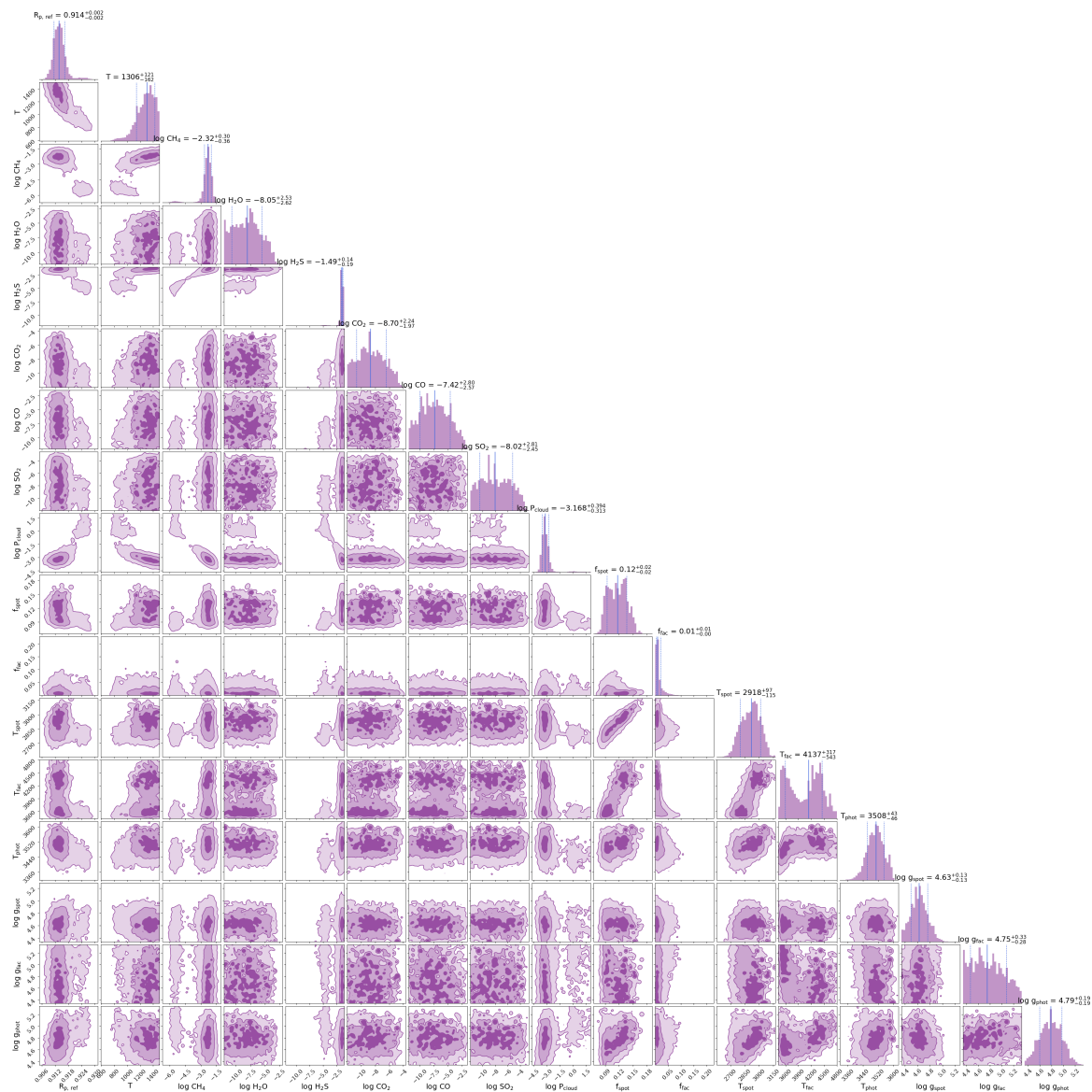


Fig. Set 5.2 – Visit 1 (clouds). Retrieval results for Visit 1 with clouds (as shown in Fig. Set 5.1).

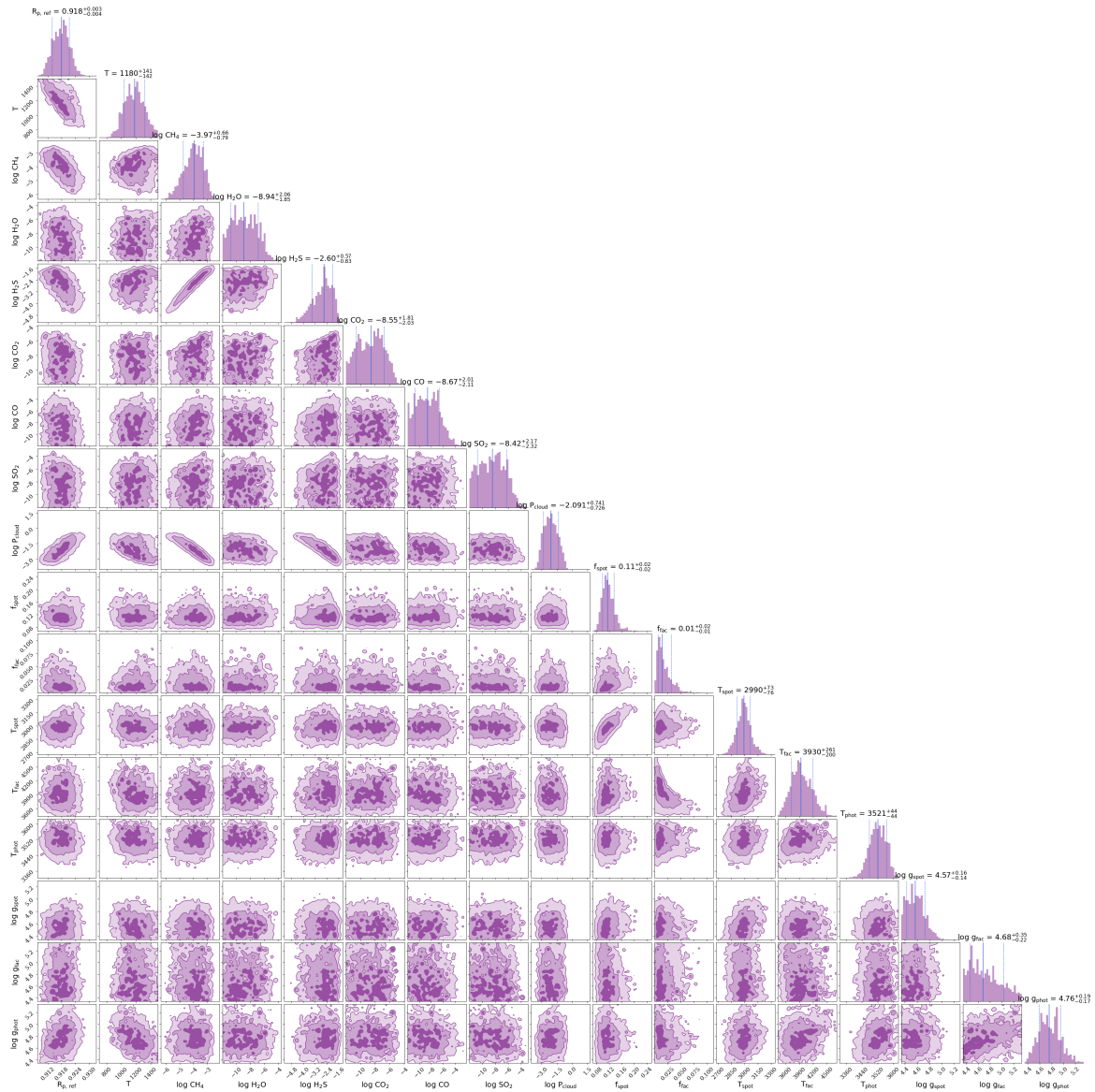


Fig. Set 5.3 – Visit 2 (clouds). Retrieval results for Visit 2 with clouds (as shown in Fig. Set 5.1).

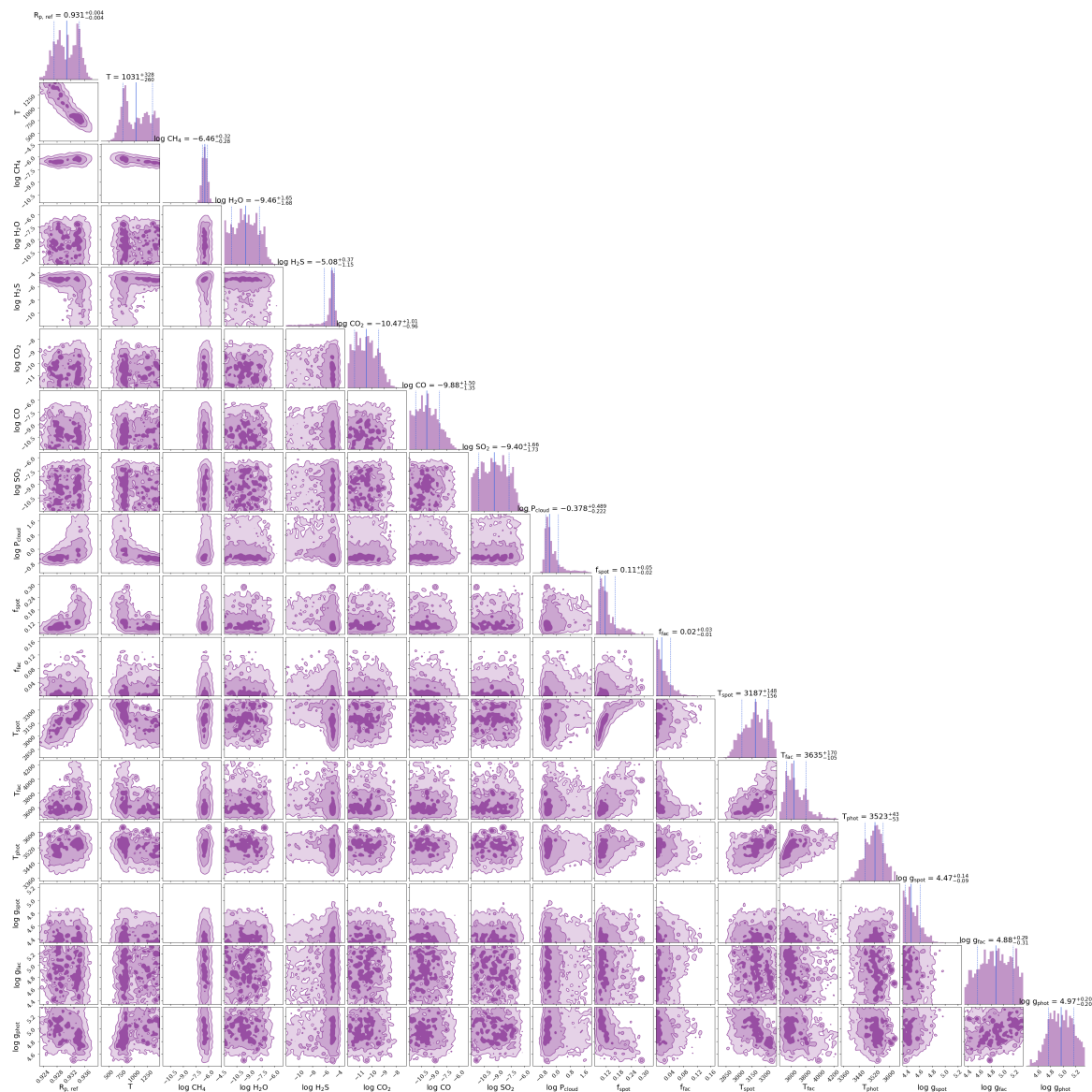


Fig. Set 5.4 – Visit 3 (clouds). Retrieval results for Visit 3 with clouds (as shown in Fig. Set 5.1).

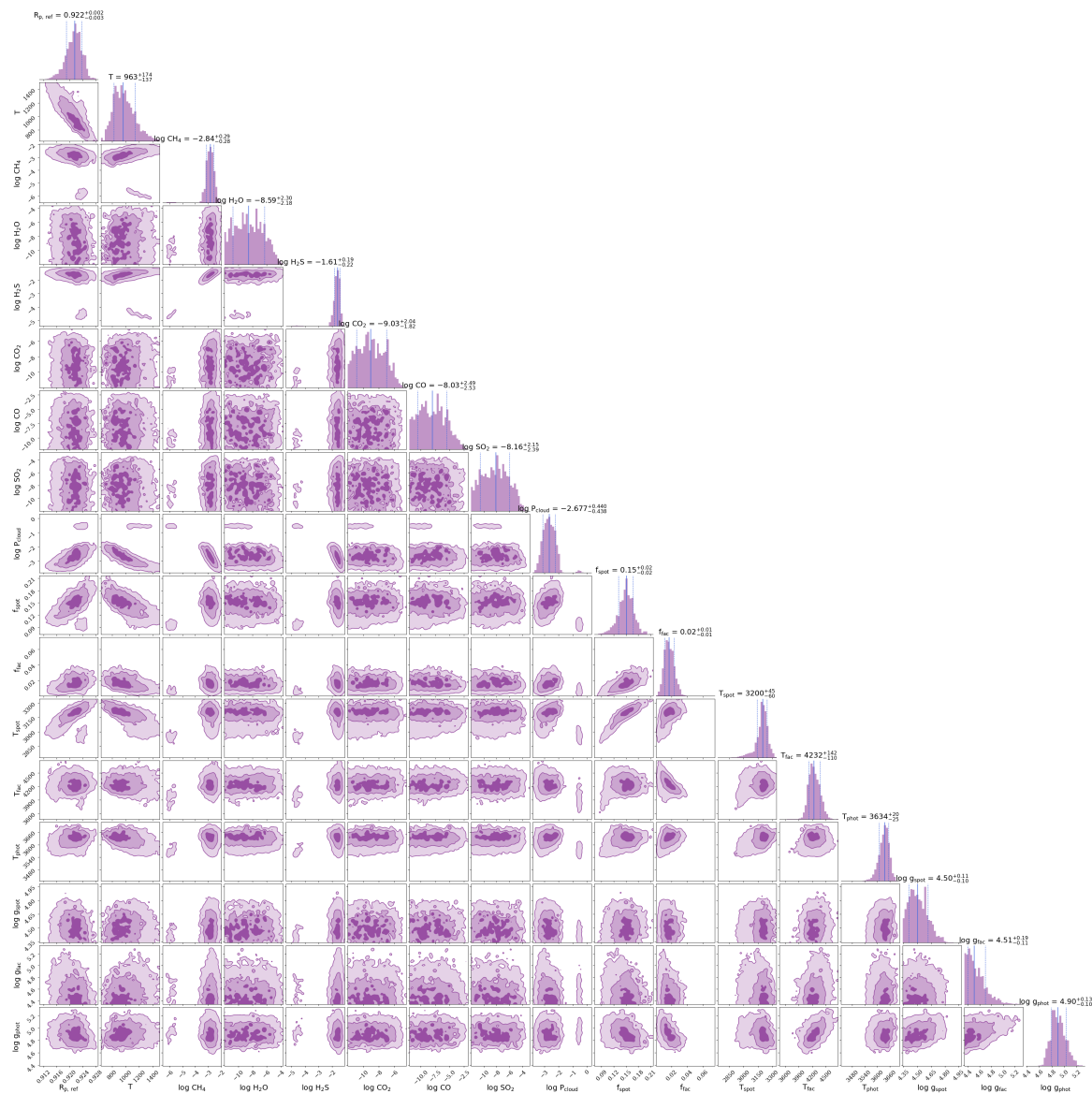


Fig. Set 5.5 – Visit Coadd (clouds). Retrieval results for the Visit co-added spectrum with clouds (as shown in Fig. Set 5.1).

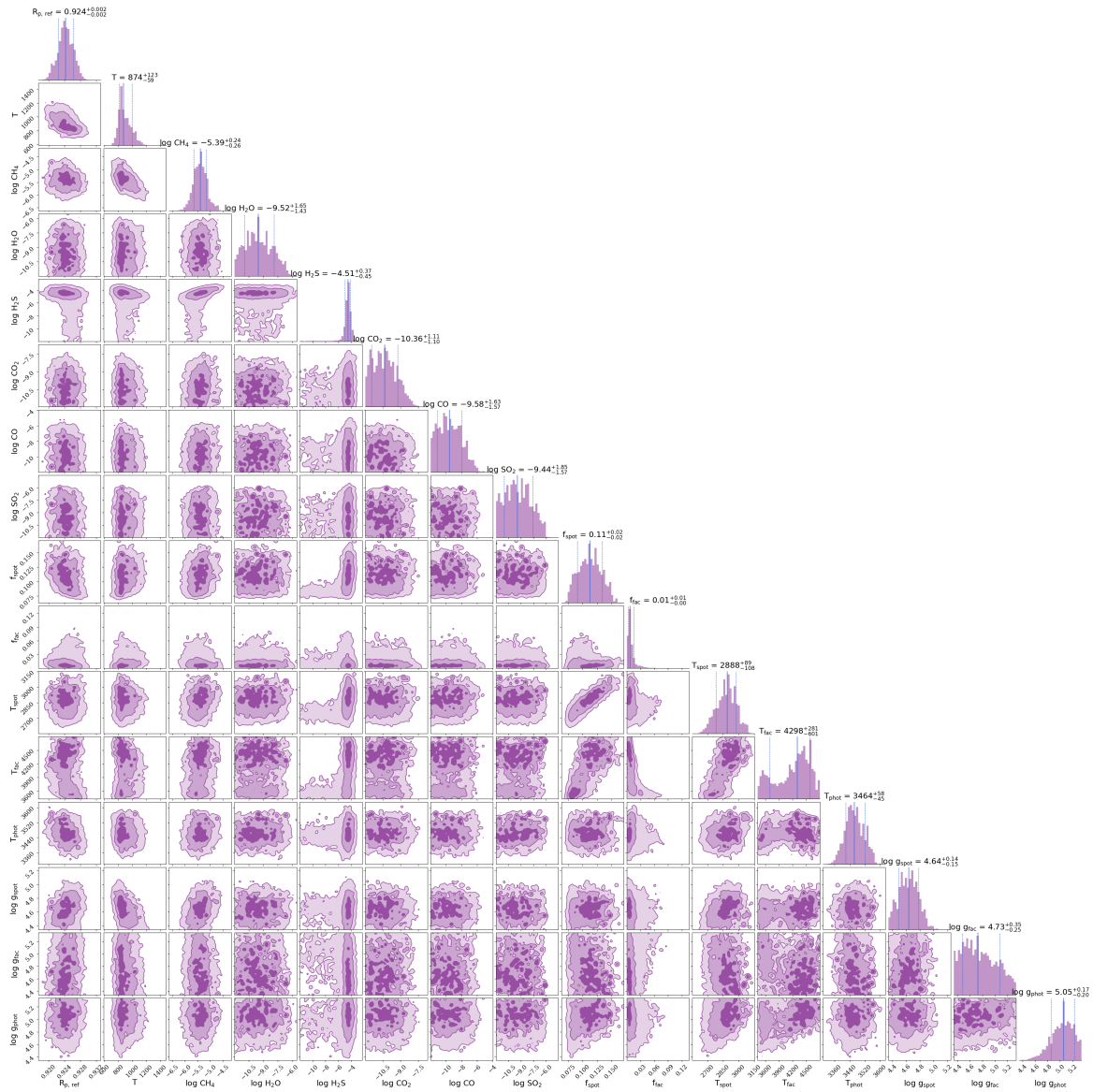


Fig. Set 5.6 – Visit 1 (no clouds). Retrieval results for Visit 1 without clouds (as shown in Fig. Set 5.1).

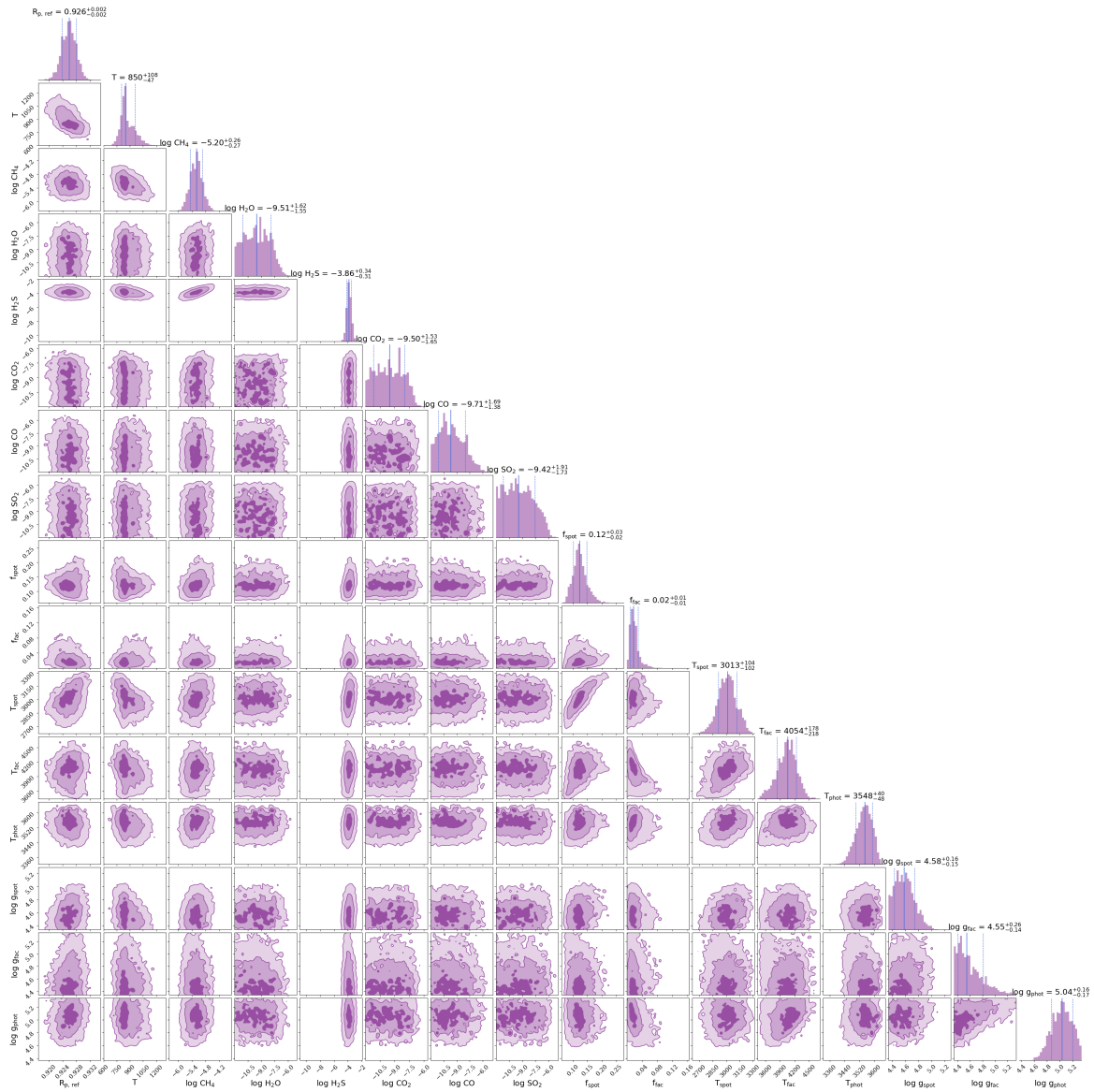


Fig. Set 5.7 – Visit 2 (no clouds). Retrieval results for Visit 2 without clouds (as shown in Fig. Set 5.1).

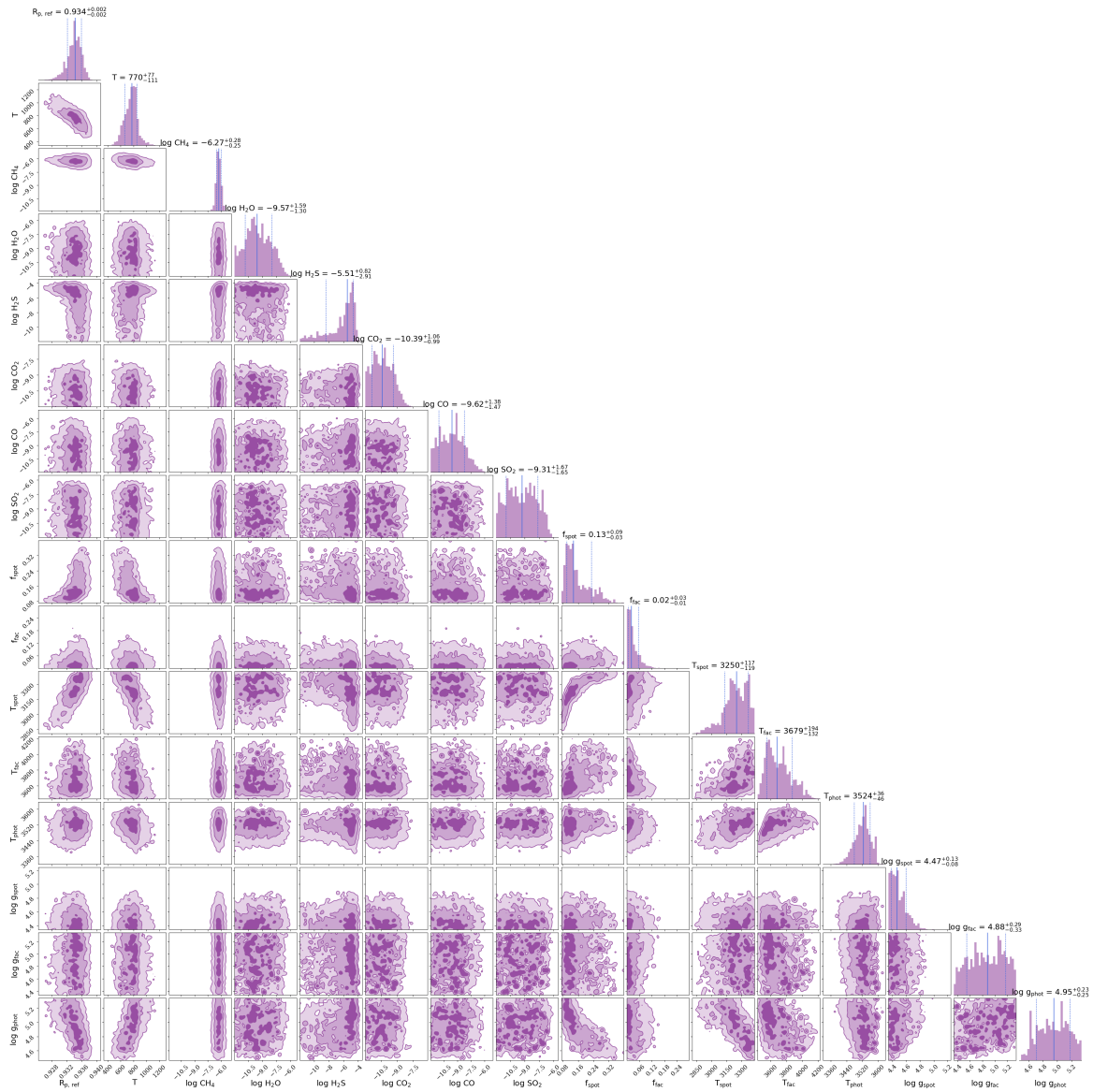


Fig. Set 5.8 – Visit 3 (no clouds). Retrieval results for Visit 3 without clouds (as shown in Fig. Set 5.1).

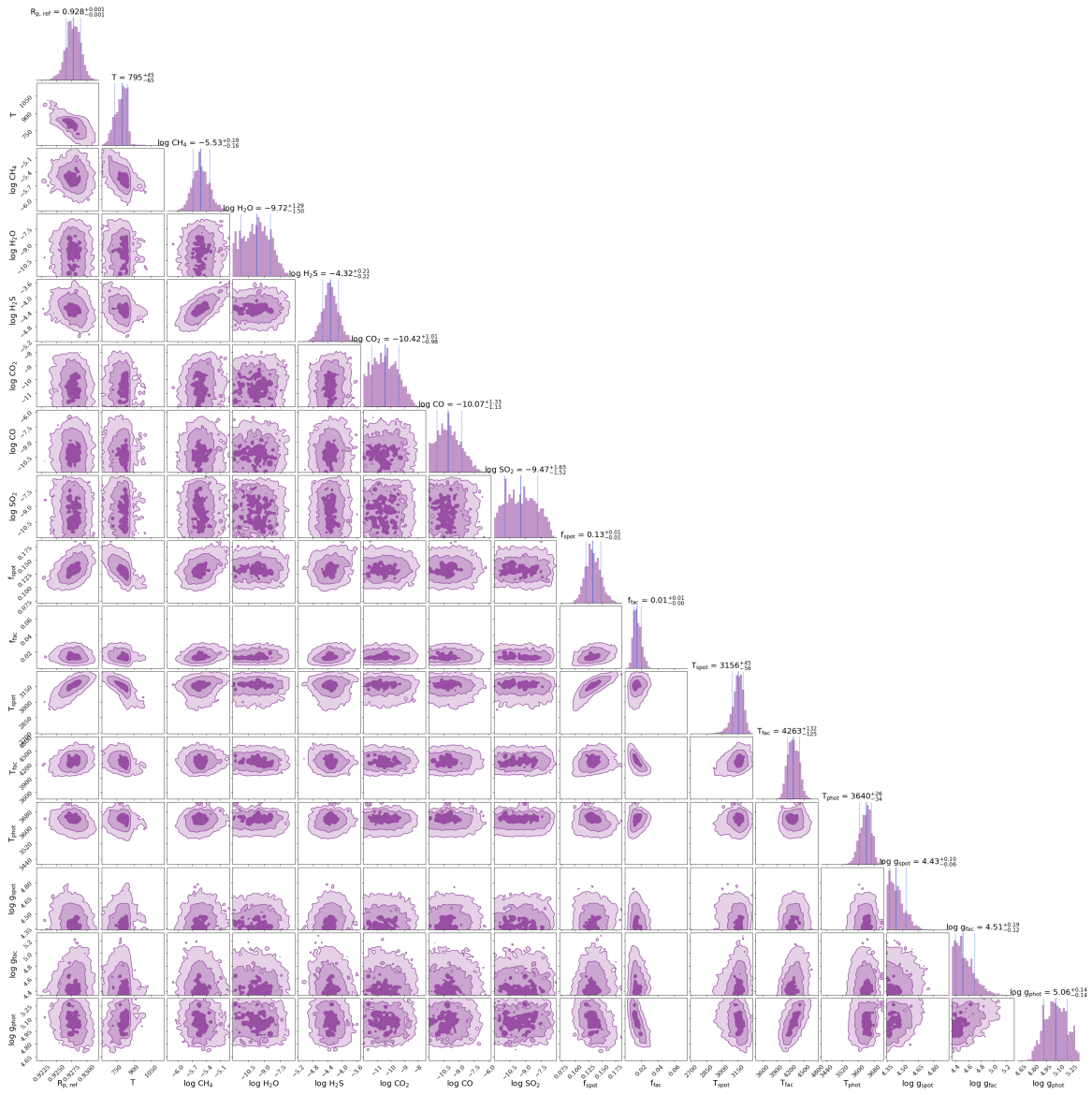


Fig. Set 5.9 – Visit Coadd (no clouds). Retrieval results for the Visit co-added spectrum without clouds (as shown in Fig. Set 5.1).

APPENDIX

A. JWST DATA REDUCTION

A.1. *ExoTiC-JEDI*

We reduced the uncalibrated data files (`*uncal.fits`) downloaded from the Barbara A. Mikulski Archive for Space Telescopes (MAST)⁸ using the Exoplanet Timeseries Characterisation – JWST Extraction and Diagnostics Investigator pipeline (*ExoTiC-JEDI*) and followed the procedure described by [Alderson et al. \(2023\)](#). The first two stages of *ExoTiC-JEDI* are wrappers to the `jwst` pipeline (v1.12.5 with CRDSv11.17.4) and adhere to the default detector and spectroscopic processing steps with minor adjustments. Stage 1 of the reduction skipped both the `superbias` and `jump` step. Stage 2 of the reduction included only the following steps: (i) `assign_wcs`, (ii) `extract_2d`, (iii) `srctype`, and (iv) `wavecorr`. Before ramp-fitting in Stage 1, *ExoTiC-JEDI* “destripped” the group-level images to correct for any correlated noise that may be introduced by the detector readout system (“1/f noise”; [Moseley et al. 2010](#); [Birkmann et al. 2022](#); [Rustamkulov et al. 2023](#)). The custom destripping step masked all pixels within 10 times the full-width-at-half-maximum (FWHM, ~ 1.1 pixels) from the trace center along the dispersion axis for all groups within an integration and subtracted the median values of non-masked pixels in each column for each group.

Before extracting the spectra, we used the data-quality flags to identify any pixels flagged as bad, saturated, dead, hot, low quantum efficiency or no gain value and replaced these with the median value of the surrounding 5 pixels on either side along the row. We similarly replaced pixels that were either 5σ outliers from the median of the surrounding 20 pixels in each row or 10σ outliers from the median of that pixel in the surrounding 10 integrations.

ExoTiC-JEDI determined the trace position by fitting a Gaussian to each column of an integration and fitting a constant value to the trace centers and FWHMs (allowing for a box aperture). This simple aperture extended to three times the FWHM of the spectral trace for a full aperture width of 7 pixels. *ExoTiC-JEDI* corrected for any remaining $1/f$ and background noise by subtracting the median of the region in each column after masking all pixels 5 FWHMs from the edge of the aperture region (the top and bottom 6 rows). The 1D spectra were extracted following the steps outlined in [Horne \(1986\)](#) and realigned for positional shifts that were determined via cross-correlation. The outliers in each light curve were removed with a 4σ -outlier rejection step.

A.2. *Eureka!*

We used the publicly available *Eureka!* pipeline, version v0.10, to analyze the Stage 0 uncalibrated data (`*uncal.fits`). *Eureka!* employs the JWST Science Calibration Pipeline (`jwst` v1.12.5; [Bushouse et al. 2023](#)) to perform the reduction of the uncalibrated files. *Eureka!* Stages 1 and 2 are wrappers for the `jwst` pipeline modules `calwebb_detector1`⁹ and `calwebb_spec2`¹⁰, which perform detector-level and spectroscopic processing, respectively. *Eureka!* Stage 1 normally performs reference pixel correction, but the NRS1 SUB512 detector region used by the NIRSpec PRISM mode does not contain reference pixels. We therefore ran *Eureka!*’s custom Row-by-row, Odd-Even By Amplifier (ROEBA) routine to correct systematic noise, using 7 rows along both the top and the bottom of the detector as reference pixels. We also employed the top and bottom 7 rows of the SUB512 subarray to perform group-level background subtraction. For Stage 1, we skipped the `jump` step (designed to find and flag outliers that are usually due to cosmic rays) because it has proven problematic for observations with low numbers of groups (e.g., [Rustamkulov et al. 2023](#)). Additionally, we found that a hot pixel in column 295 resulted in biased flux levels for the corresponding wavelength during stellar spectral extraction. To correct this problem, we created a new custom mask by flagging this pixel as “DO_NOT_USE” in a modified version of the Calibration References Data System (CRDSv11.17.4) `jwst_nirspec_mask_0074.fits` file.

For Stage 2, we followed the recommendation of the Early Release Science team and skipped the `flat_field` step because it removes regions of the spectral trace (e.g., [Alderson et al. 2023](#)). We also skipped the `photom` step that converts data from units of count rate to flux density in MegaJanskies (MJy), which is not necessary for the ensuing data analysis steps in exoplanet transit TSO observations.

⁸ <https://mast.stsci.edu/portal/Mashup/Clients/Mast/Portal.html>

⁹ https://jwst-pipeline.readthedocs.io/en/latest/jwst/pipeline/calwebb_detector1.html

¹⁰ https://jwst-pipeline.readthedocs.io/en/latest/jwst/pipeline/calwebb_spec2.html

Eureka! Stage 3 performs background subtraction and optimal spectral extraction (Horne 1986) on the Stage 2 outputs, producing a time series of 1D stellar spectra for use in light curve fitting (Appendix D). We adopted a spectral half-widths of 3 pixels in our final analyses, since we found this half-width minimized scatter in our white light curve fits. Our Stage 3 background region included pixels along the top and bottom of the SUB512 subarray, greater than 7 pixels from the center of the 2D stellar spectrum. In our optimal extraction, we created a normalized spatial profile by using the median of all data frames, and we clipped outliers greater than $10\text{-}\sigma$ (step 7 of Horne 1986). We used **Eureka!** to extract spectra from columns 30 – 491 ($\sim 0.520 - 5.579 \mu\text{m}$).

We used **Eureka!** Stages 4 to generate the spectroscopic light curves by binning the time series of 1D stellar spectra output from Stage 3 along the wavelength axis. We generated spectroscopic light curves at the native resolution of NIRSPEC PRISM, producing one light curve for each column on the detector.

B. DISCREPANCY WITH THE PUBLISHED RADIUS

Kanodia et al. (2023) measured the radius ratio of TOI-5205b as $R_{\text{ARCTIC}}/R_{\star} = 0.2720^{+0.0039}_{-0.0043}$ using ground-based data obtained with the Astrophysical Research Consortium (ARC) Telescope Imaging Camera on the 3.5m telescope at the Apache Point Observatory (ARCTIC; Huehnerhoff et al. 2016). This is deeper ($\Delta(R_p/R_{\star}) = 0.0245$) than the transit depth recovered with JWST ($R_{\text{JWST}}/R_{\star} = 0.2475^{+0.0003}_{-0.0002}$). To investigate this discrepancy, we extracted all available TESS photometry (through Sector 82) using an effective point spread function to correct for contamination from on-sky companions with `tg1c` (Han & Brandt 2023). A comparison of the photometry is shown in Figure 12, illustrating that JWST has the best precision and the smallest transit depth of all the photometry ($\sim 1\%$ shallower).

Han & Brandt (2023) note there exist limitations to the dilution-correction for point-spread function photometry from TESS due to the incomplete nature of the Gaia DR3 catalog such that the PSF-derived photometry may not match the true depth of the transit, but the `tg1c` photometry is still consistent with the JWST depth at the $1-2\sigma$ level. The ground-based data from ARCTIC have limited baselines either due to poor weather conditions or dusk that could impact the measured transit depth. We investigated whether this depth difference could be due to unocculted spots and modeled the ground-based ARCTIC Sloan i' transit using the modified `juliet` code described in Appendix D. For this fit, we used the posterior values for the orbital parameters from Table 2 ($P, T_0, a/R_{\star}, R_p/R_{\star}, b$) as priors and retained the uninformed spot priors. The fit requires an unocculted spot with a flux ratio of $f_{\text{spot,ARCTIC}} = 0.62 \pm 0.01$ (corresponding temperature of $T_{\text{spot,ARCTIC}} = 3170 \pm 50$ K). This spot would have to be present for both the ground-based transits from ARCTIC (separated by 72 days but with identical depths) while remaining outside the transit chord and subsequently disappearing before the JWST observations. This scenario is unlikely due to the significant surface evolution observed in the three consecutive JWST transits (see Figure 1), which suggested that a specific spot configuration is unlikely to be long-lived. Furthermore, this high flux ratio is inconsistent with the observed spot contrasts and the predictions for other mid-M dwarfs (e.g., Mori et al. 2024). Even with the change in spot configuration seen in the JWST data, the transit depths across the three visits are remarkably consistent. We do not assume that this change in depth between JWST and ARCTIC is astrophysical in nature, and instead attribute the discrepancy to uncorrected systematics in the ARCTIC photometry (due to weather, airmass, or other sky conditions). These systematics cannot be robustly characterized or corrected with the existing out-of-transit baseline and subsequently lead to an apparently inflated radius. The importance of a proper baseline to correct for systematic trends and derive an unbiased depth has been noted for other planetary systems (e.g., Libby-Roberts et al. 2023). For this work, we adopt the radius derived using the JWST data.

C. A COMPARISON OF GRID-BASED LIMB-DARKENING COEFFICIENTS

We used `ExoTiC-LD` (Grant & Wakeford 2024) to investigate the impact of different limb-darkening coefficients for the quadratic limb-darkening law. We investigated most options available with `ExoTiC-LD`, including limb-darkening coefficients derived with the (i) PHOENIX stellar library (henceforth, PHOENIX; Husser et al. 2013), (ii) ATLAS9 stellar library (henceforth, Kurucz; Kurucz 1970, 1993), (iii) MPS-ATLAS stellar library (henceforth, MPS1/2; Kostogryz et al. 2022), and (iv) the STAGGER grid of three-dimensional hydrodynamic model atmospheres (henceforth, STAGGER; Magic et al. 2015). While the comparison includes the STAGGER grid (Magic et al. 2015), the nearest STAGGER grid point in `ExoTiC-LD` had an effective temperature of $T_{\text{eff}} = 4500$ K, which is > 1000 K hotter than the observed $T_{\text{eff}} = 3430$ K for TOI-5205. We also note that the MPS1/2 and Kurucz grids have lower limits of $T_{\text{eff}} = 3500$ K. For this comparison, we produced another set of spectra in which the limb-darkening coefficients were free parameters that were sampled via uninformed priors following Kipping (2013). All spectra were produced

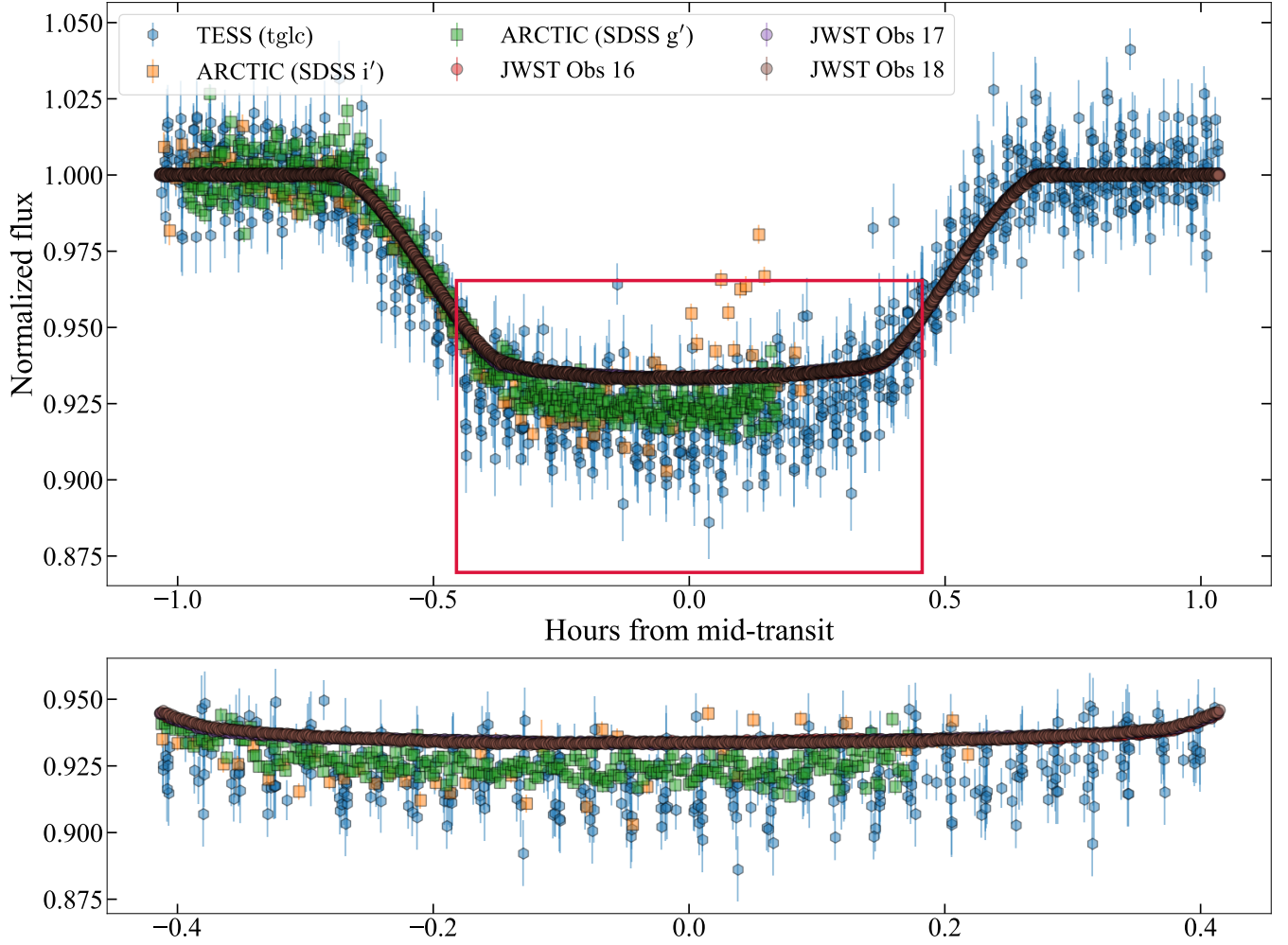


Figure 12. **Top:** A comparison of published ARCTIC photometry from [Kanodia et al. \(2023\)](#) with the photometry derived in this work. **Bottom:** A zoom into the region indicated by a rectangle on the top panel. Both panels display the phase-folded photometry for ARCTIC transits from [Kanodia et al. \(2023\)](#), the TESS data derived using a point-spread function to attempt to correct for dilution, and the JWST data. All ARCTIC transits and all TESS transits (before and after JWST observations) are deeper than the white light curves from JWST.

using the best-fitting orbital parameters from [Table 2](#) and ignoring spot crossing events. A comparison of the spectra for the ExoTiC-JEDI reductions is presented in [Fig. Set. 13](#). There is a significant discrepancy in transit depth in the region $\leq 2.5 \mu\text{m}$ when the limb-darkening coefficients were fixed to values from the grids. The spectra derived using the PHOENIX limb-darkening coefficients are most similar to the spectra where we fit the coefficients. Other stellar grids showed differences at the $1 - 2\sigma$ level until $\sim 4 \mu\text{m}$. Given the limitations in (i) temperature coverage of the MPS1/2, Kurucz, and STAGGER grids, (ii) large disagreement between grids, and (iii) mismatch between the PHOENIX spectra in the mid-infrared for mid-M dwarfs (e.g., [Rajpurohit et al. 2018](#)), we use spectra where the limb-darkening coefficients are sampled following [Kipping \(2013\)](#) for all data analyzed in the body of this manuscript.

Fig. Set 13. A comparison of limb-darkening coefficients for the quadratic limb-darkening law.

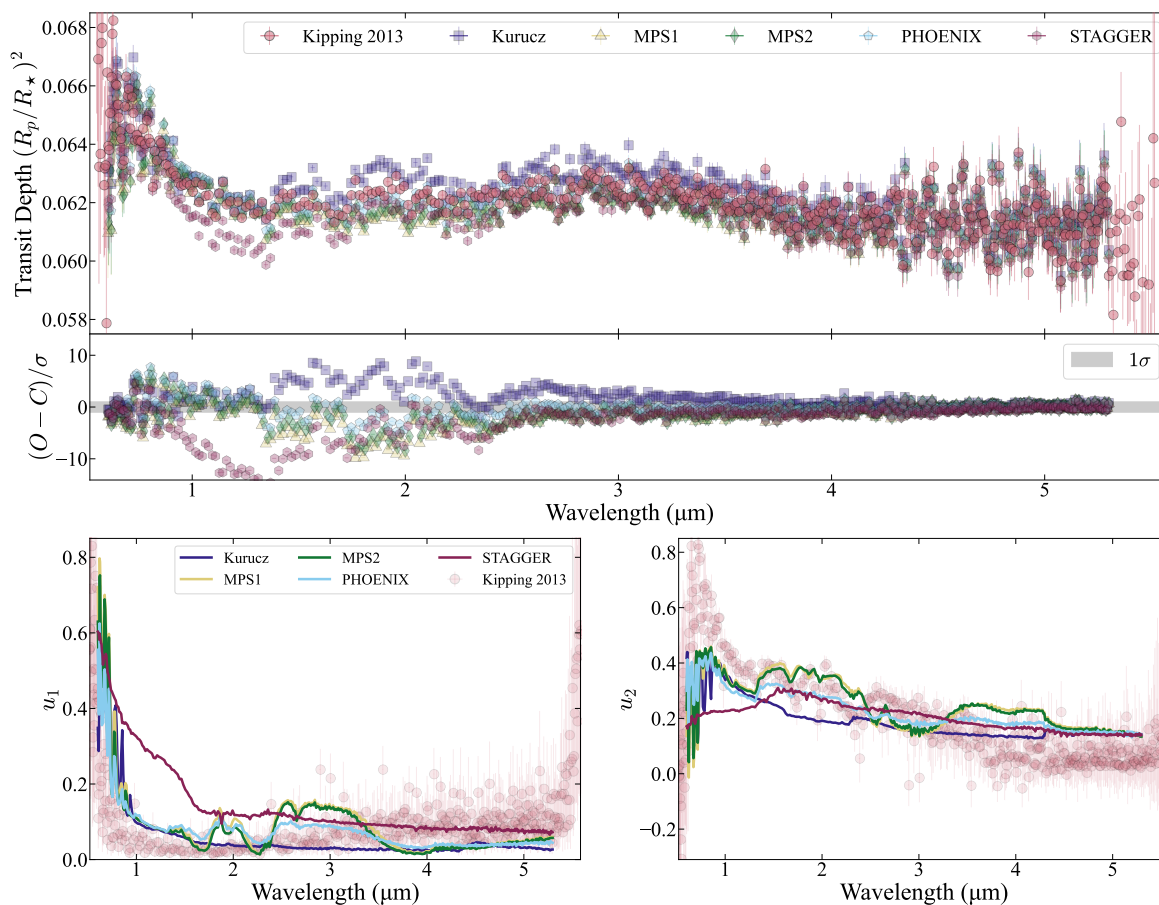


Fig. Set 13.1 – Obs. 16. **Top:** TOI-5205b transmission spectra for observation 16 derived using either fixed quadratic limb-darkening coefficients from ExoTiC-LD or fitting for the limb-darkening parameters following the parametrization from [Kipping \(2013\)](#). Spectra are labeled according to the limb-darkening coefficient grid. The spectrum where limb-darkening coefficients are free parameters has wider wavelength coverage due to the limited wavelength coverage of ExoTiC-LD. **Middle:** The residuals with respect to the model with free limb-darkening coefficients (labeled “Kipping 2013”). The residuals are divided by the observed error of each spectra. The $\pm 1\sigma$ region is shaded for reference. **Bottom:** The limb-darkening coefficients, u_1 and u_2 , for a quadratic limb-darkening law that were used to generate the spectra in the top panel.

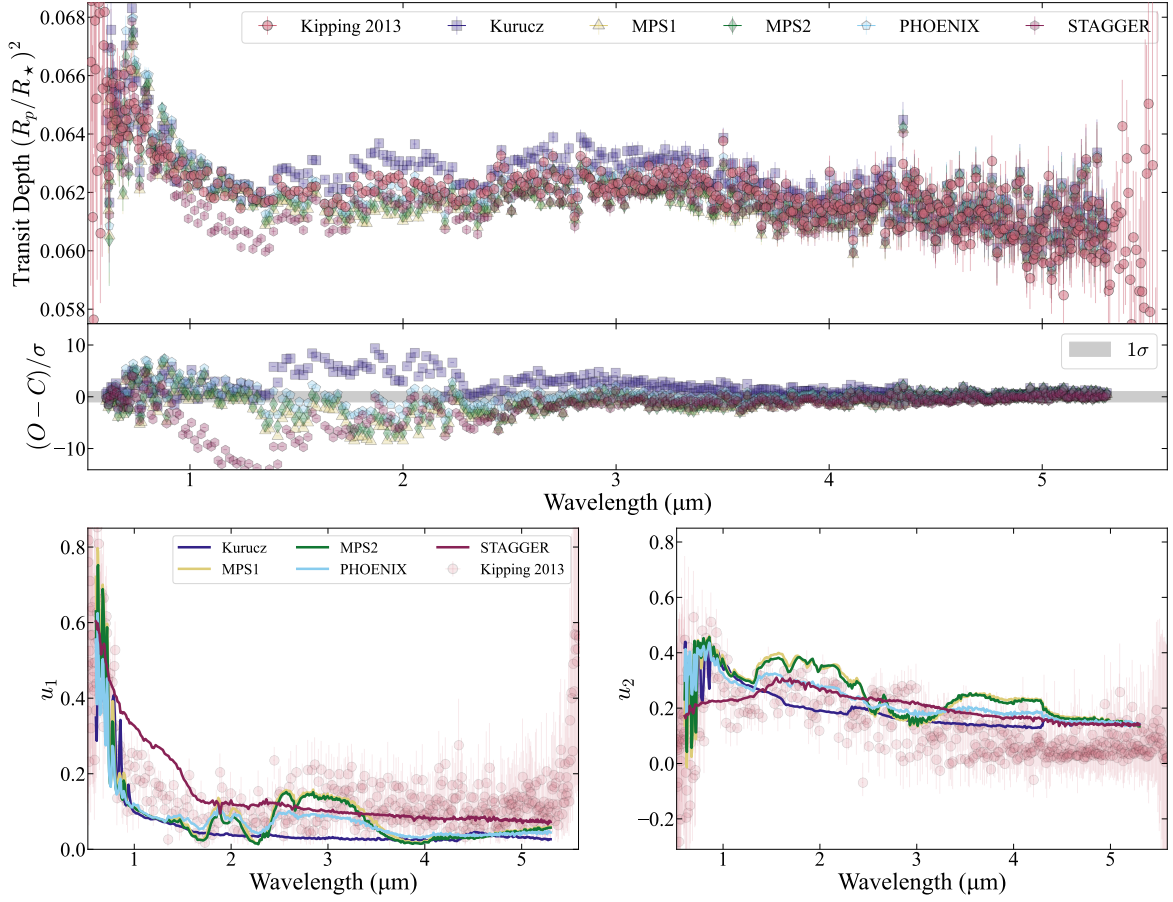


Fig. Set 13.2 – Obs. 17. Top: TOI-5205b transmission spectra for observation 17 derived using either fixed quadratic limb-darkening coefficients from `ExoTiC-LD` or fitting for the limb-darkening parameters following the parametrization from [Kipping \(2013\)](#). Spectra are labeled according to the limb-darkening coefficient grid. The spectrum where limb-darkening coefficients are free parameters has wider wavelength coverage due to the limited wavelength coverage of `ExoTiC-LD`. **Middle:** The residuals with respect to the model with free limb-darkening coefficients (labeled “Kipping 2013”). The residuals are divided by the observed error of each spectra. The $\pm 1\sigma$ region is shaded for reference. **Bottom:** The limb-darkening coefficients, u_1 and u_2 , for a quadratic limb-darkening law that were used to generate the spectra in the top panel.

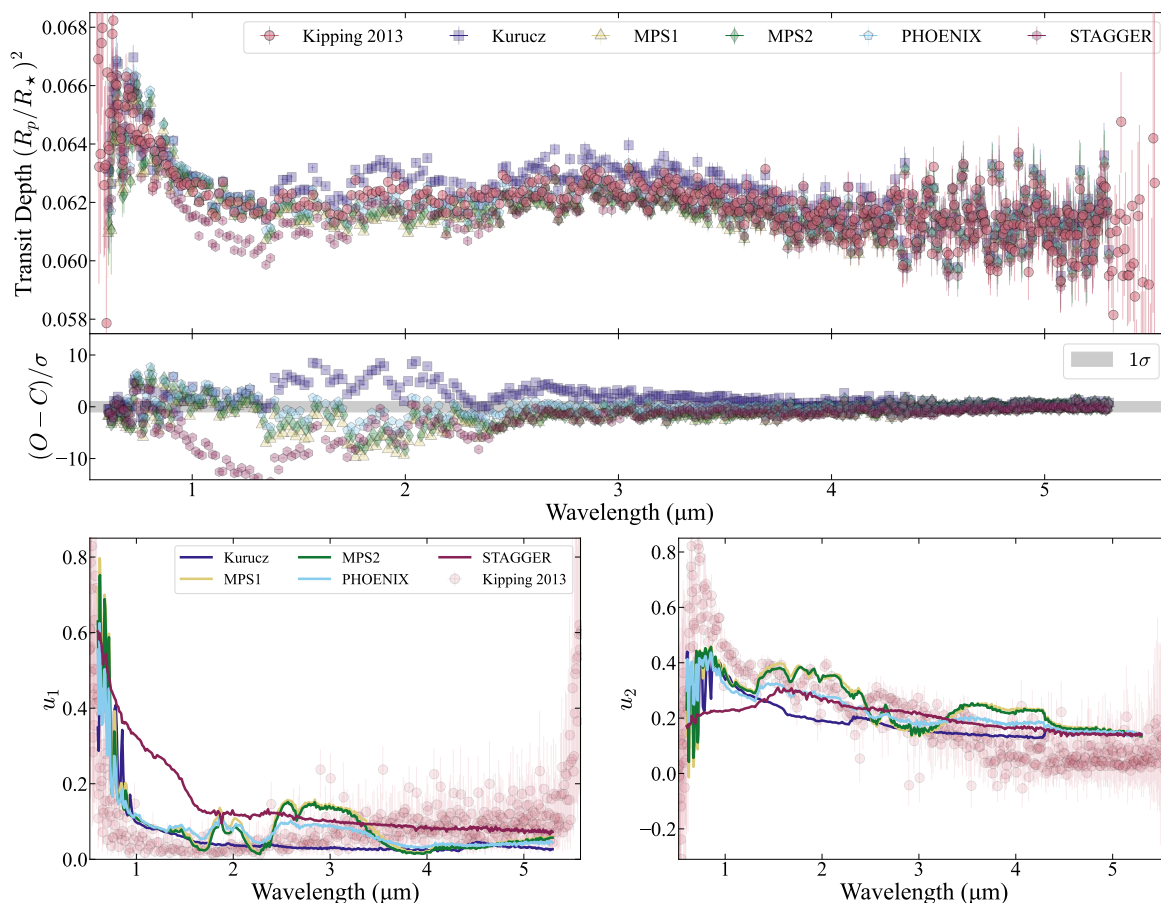


Fig. Set 13.3 – Obs. 18. **Top:** TOI-5205b transmission spectra for observation 18 derived using either fixed quadratic limb-darkening coefficients from `ExoTiC-LD` or fitting for the limb-darkening parameters following the parametrization from [Kipping \(2013\)](#). Spectra are labeled according to the limb-darkening coefficient grid. The spectrum where limb-darkening coefficients are free parameters has wider wavelength coverage due to the limited wavelength coverage of `ExoTiC-LD`. **Middle:** The residuals with respect to the model with free limb-darkening coefficients (labeled “Kipping 2013”). The residuals are divided by the observed error of each spectra. The $\pm 1\sigma$ region is shaded for reference. **Bottom:** The limb-darkening coefficients, u_1 and u_2 , for a quadratic limb-darkening law that were used to generate the spectra in the top panel.

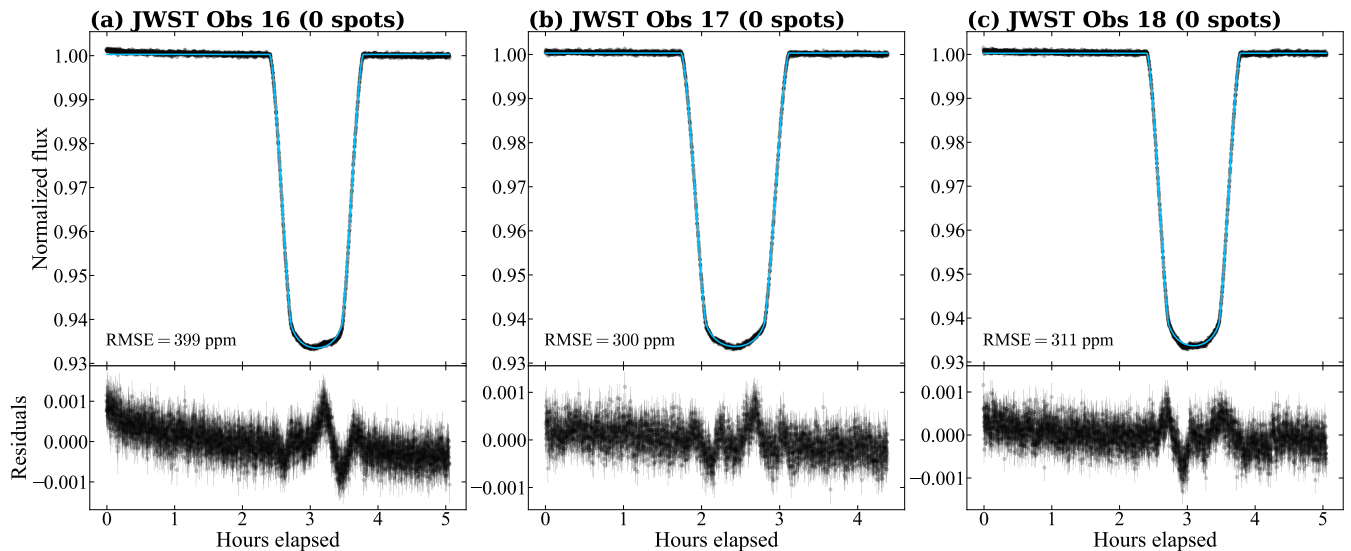


Figure 14. Similar to figure [Figure 1](#) except the model includes no spots. The best-fitting model is indicated by the solid line with residuals to the fit indicated in the bottom row.

D. LIGHT CURVE FITTING

D.1. Spot crossing event model

Spots were modeled using `spotrod`¹¹ (Béky et al. 2014) and treated as projected circles on a spherical surface that were individually parameterized by four parameters: the (i) spot flux ratio, f_{spot} , which represents the ratio of the integrated flux of the spot compared to the stellar photosphere in a given wavelength bin ($f_{\text{spot}} = 1$ represents the photosphere), (ii) spot radius, r_{spot} , which is size of the spot in units of stellar radii, and (iii) two positional parameters, x_{spot} and y_{spot} , which describe the center of the spot in stellar radii using a projected planetary coordinate system (Winn 2010).

D.2. White light curve fits

To determine an optimal configuration, we jointly fit the white light curves from the ExoTiC-JEDI reduction using all combinations of spots (between 1 – 4) for each visit. We binned the white light curves (5s cadence) for these fits to decrease the computational time. Each fit applied (i) a uniform prior on the spot flux ratio ($0 \leq f_{\text{spot}} \leq 1$) which was shared between all three transits, (ii) a uniform prior on the radius ($0 \leq r_{\text{spot}} \leq 0.5$) that was different for each spot, (iii) and spot position that varied for each spot and was randomly sampled from a unit disk.

We sampled the parameter space using the dynamic nested sampler `dynesty` (Speagle 2020) using 5000 live points and a convergence criterion of $\Delta \ln Z = 0.01$. The models with different spot configurations were then compared using the Bayesian evidence (B). We adopted the configuration with 4 spots in visit 1, 4 spots in visit 2, and 3 spots in visit 3 as it maximized the evidence when compared to configurations with fewer spots. The spot parameters, along with their priors, for the adopted configuration are listed in [Table 7](#).

For reference, we show the best-fitting model with no spot crossing events in [Figure 14](#), showing significant in-transit residuals. We note that the adopted spot configuration resulted in unocculted spots and retained residual structure in the residuals for visit 3. This is a result of assuming a fixed spot flux ratio for all three transits. We investigated the impact of a unique spot flux ratio for each visit (2 additional free parameters to the white light curve models) and note that while the residuals no longer showed a strong feature in transit, the differences in the resulting spectrum for our third visit were within 1σ of the adopted configuration.

The fit to the white light curve revealed spots with a high-flux ratio ($f_{\text{spot}} = 0.925 \pm 0.003$) and a spot temperature ($T_{\text{spot}} = 3350 \pm 50$ K), which is ~ 100 K cooler than the photosphere. Although the sample of mid-M dwarfs with known spot temperatures is limited, it is expected that the spot contrast decreases with decreasing stellar temperature (e.g., Berdyugina 2005). A flux ratio of ~ 0.9 is consistent with the temperature differential between spotted and

¹¹ <https://github.com/bencebeky/spotrod>

ambient temperatures for other mid-M dwarfs (e.g., [Herbst et al. 2021](#); [Almenara et al. 2022](#); [Waalkes et al. 2024](#); [Mori et al. 2024](#)).

D.3. Spectroscopic light curve fits

We fixed the orbital parameters P , T_0 , e , ω , and i from [Table 2](#) along with the spot configuration to the values from [Table 7](#) that were derived from our white light curve fit. The light curve for each spectral channel had eight free parameters, including the (i) radius ratio (R_p/R_\star), (ii) parameterized coefficients for a quadratic limb-darkening law (q_1 , q_2), (iii) coefficients for a second-order polynomial as a function of time to model the out-of-transit baseline, (iv) spot flux ratio (f_{spot}), and (v) a multiplicative factor to the uncertainties for each channel. We sampled the parameter space using the dynamic nested sampler *dynesty* with 1000 live points and a convergence criterion of $\Delta \ln Z = 0.1$. A few channels for all visits of the ExoTiC-JEDI reduction are shown in [Figure 15](#) and the transit depths as a function of wavelength (i.e., the transmission spectra) for both the ExoTiC-JEDI and *Eureka!* reductions are shown in [Figure 2](#).

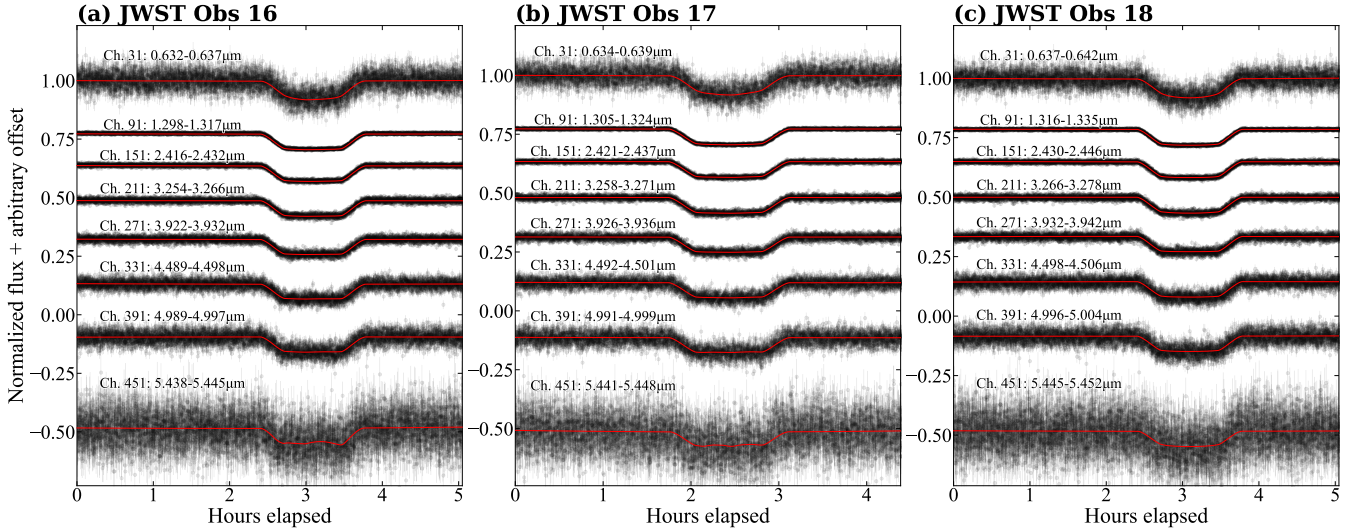


Figure 15. Panels (a)-(c) show NIRSpect PRISM light curves from a few channels, after binning to 1 min for clarity. The best-fitting model for each channel is indicated by the solid line and adopts the spot configuration (position and size) from the white light curve fit (shown in [Figure 1](#)).

Table 7. System parameters for TOI-5205

Name	Prior ^a	Value	Source
Obs. 16 spot parameters ^a :			
Spot contrast ^b (f_{spot})	$\mathcal{U}(0, 1)$	0.925 ± 0.003	This work
$U_{16,1}$	$\mathcal{U}(0, 1)$	0.64 ± 0.02	This work
$V_{16,1}$	$\mathcal{U}(0, 1)$	0.771 ± 0.001	This work
$r_{\text{spot},16,1}$	$\mathcal{U}(0, 0.5)$	0.48 ± 0.01	This work
$U_{16,2}$	$\mathcal{U}(0, 1)$	0.322 ± 0.009	This work
$V_{16,2}$	$\mathcal{U}(0, 1)$	0.580 ± 0.005	This work
$r_{\text{spot},16,2}$	$\mathcal{U}(0, 0.5)$	$0.144^{+0.008}_{-0.006}$	This work
$U_{16,3}$	$\mathcal{U}(0, 1)$	0.95 ± 0.01	This work
$V_{16,3}$	$\mathcal{U}(0, 1)$	$0.0009^{+0.0012}_{-0.0007}$	This work
$r_{\text{spot},16,3}$	$\mathcal{U}(0, 0.5)$	0.41 ± 0.01	This work
$U_{16,4}$	$\mathcal{U}(0, 1)$	$0.33^{+0.03}_{-0.04}$	This work

Table 7 continued

Table 7 (continued)

Name	Prior ^a	Value	Source
$V_{16,4}$	$\mathcal{U}(0, 1)$	0.32 ± 0.02	This work
$r_{\text{spot},16,4}$	$\mathcal{U}(0, 0.5)$	0.42 ± 0.02	This work
Obs. 17 spot parameters:			
$U_{17,1}$	$\mathcal{U}(0, 1)$	0.55 ± 0.01	This work
$V_{17,1}$	$\mathcal{U}(0, 1)$	0.810 ± 0.002	This work
$r_{\text{spot},17,1}$	$\mathcal{U}(0, 0.5)$	0.25 ± 0.01	This work
$U_{17,2}$	$\mathcal{U}(0, 1)$	0.57 ± 0.03	This work
$V_{17,2}$	$\mathcal{U}(0, 1)$	0.07 ± 0.02	This work
$r_{\text{spot},17,2}$	$\mathcal{U}(0, 0.5)$	$0.41^{+0.03}_{-0.02}$	This work
$U_{17,3}$	$\mathcal{U}(0, 1)$	0.29 ± 0.01	This work
$V_{17,3}$	$\mathcal{U}(0, 1)$	0.685 ± 0.002	This work
$r_{\text{spot},17,3}$	$\mathcal{U}(0, 0.5)$	$0.102^{+0.004}_{-0.003}$	This work
$U_{17,4}$	$\mathcal{U}(0, 1)$	$0.68^{+0.03}_{-0.02}$	This work
$V_{17,4}$	$\mathcal{U}(0, 1)$	$0.854^{+0.006}_{-0.007}$	This work
$r_{\text{spot},17,4}$	$\mathcal{U}(0, 0.5)$	0.13 ± 0.03	This work
Obs. 18 spot parameters:			
$U_{18,1}$	$\mathcal{U}(0, 1)$	0.79 ± 0.04	This work
$V_{18,1}$	$\mathcal{U}(0, 1)$	0.23 ± 0.02	This work
$r_{\text{spot},18,1}$	$\mathcal{U}(0, 0.5)$	$0.19^{+0.03}_{-0.02}$	This work
$U_{18,2}$	$\mathcal{U}(0, 1)$	0.51 ± 0.02	This work
$V_{18,2}$	$\mathcal{U}(0, 1)$	0.529 ± 0.004	This work
$r_{\text{spot},18,2}$	$\mathcal{U}(0, 0.5)$	0.10 ± 0.01	This work
$U_{18,3}$	$\mathcal{U}(0, 1)$	$0.40^{+0.04}_{-0.05}$	This work
$V_{18,3}$	$\mathcal{U}(0, 1)$	0.25 ± 0.02	This work
$r_{\text{spot},18,3}$	$\mathcal{U}(0, 0.5)$	0.10 ± 0.02	This work

^aFor all spots, the center is randomly sampled from a unit disk using the dimensionless parameters U and V , where the inputs to `spotrod` are calculated as $X = \sqrt{U} \cos(2\pi V)$ and $Y = \sqrt{U} \sin(2\pi V)$.

^bAll spots share the same flux ratio such that we fit for an average spot flux ratio that does not change throughout our three consecutive visits.

E. RETRIEVAL SUPPORTING MATERIALS

E.1. Retrieval Tables

Table 8 and Table 5 provide quantitative results for the cloudy and clear retrievals on the individual visit spectra and the co-added spectrum. The abundances ($\log X$) are the volume mixing ratios for each species.

E.2. Retrieval Fit Residuals

Fig. Set 15 shows the cloud free M3.1 retrieval model fit to the co-added TOI-5205b transmission spectrum with 1 and 2σ credibility envelopes (upper panel) and residuals between the median fit and the data (lower panel). There is an excessive number of poorly fit data points between $1 - 3 \mu\text{m}$ that are present in all three visits. This spectral region drives our $\chi^2_\nu > 1$ and may be due to underestimated uncertainties or insufficient stellar spectral models that cannot completely reproduce

the contaminated transmission spectrum of TOI-5205b. Our model fits also systematically overestimate the transit depths at the reddest wavelengths $\lambda > 4.8 \mu\text{m}$. This could be due to the spot crossings or TLS contamination, which still have an impact beyond $4 \mu\text{m}$, or potentially due to nightside emission from the planet during transit, which can decrease transit depths relative to models without contamination.

Table 8. Atmospheric retrieval priors and posteriors for the M3.2 model with clouds (VMR)

Parameters	Priors	Visit 1	Visit 2	Visit 3	Visits Co-added
$R_{p, \text{ref}}$	$\mathcal{U}(0.88, 1.19)$	$0.9138^{+0.0025}_{-0.0023}$	$0.9179^{+0.0035}_{-0.0039}$	$0.9308^{+0.0036}_{-0.0037}$	$0.9215^{+0.0021}_{-0.0026}$
T	$\mathcal{U}(200.00, 1500.00)$	1306^{+121}_{-162}	1180^{+141}_{-142}	1030^{+328}_{-259}	963^{+174}_{-137}
$\log \text{CH}_4$	$\mathcal{U}(-12.00, -1.00)$	$-2.32^{+0.30}_{-0.36}$	$-3.97^{+0.66}_{-0.79}$	$-6.46^{+0.32}_{-0.28}$	$-2.84^{+0.29}_{-0.28}$
$\log \text{H}_2\text{O}$	$\mathcal{U}(-12.00, -1.00)$	$-8.1^{+2.5}_{-2.6}$	$-8.9^{+2.1}_{-1.8}$	$-9.5^{+1.7}_{-1.7}$	$-8.6^{+2.3}_{-2.2}$
$\log \text{H}_2\text{S}$	$\mathcal{U}(-12.00, -1.00)$	$-1.49^{+0.14}_{-0.19}$	$-2.60^{+0.57}_{-0.83}$	$-5.08^{+0.37}_{-1.15}$	$-1.62^{+0.19}_{-0.22}$
$\log \text{CO}_2$	$\mathcal{U}(-12.00, -1.00)$	$-8.7^{+2.2}_{-2.0}$	$-8.6^{+1.8}_{-2.0}$	$-10.47^{+1.01}_{-0.96}$	$-9.0^{+2.0}_{-1.8}$
$\log \text{CO}$	$\mathcal{U}(-12.00, -1.00)$	$-7.4^{+2.8}_{-2.6}$	$-8.7^{+2.0}_{-2.1}$	$-9.9^{+1.5}_{-1.4}$	$-8.0^{+2.5}_{-2.5}$
$\log \text{SO}_2$	$\mathcal{U}(-12.00, -1.00)$	$-8.0^{+2.8}_{-2.4}$	$-8.4^{+2.2}_{-2.3}$	$-9.4^{+1.7}_{-1.7}$	$-8.2^{+2.2}_{-2.4}$
$\log P_{\text{cloud}}$	$\mathcal{U}(-6.00, 2.00)$	$-3.17^{+0.39}_{-0.31}$	$-2.09^{+0.74}_{-0.73}$	$-0.38^{+0.49}_{-0.22}$	$-2.68^{+0.44}_{-0.44}$
f_{spot}	$\mathcal{U}(0.00, 1.00)$	$0.117^{+0.020}_{-0.023}$	$0.114^{+0.021}_{-0.016}$	$0.115^{+0.048}_{-0.022}$	$0.151^{+0.016}_{-0.019}$
f_{fac}	$\mathcal{U}(0.00, 0.50)$	$0.0094^{+0.0127}_{-0.0040}$	$0.015^{+0.017}_{-0.008}$	$0.017^{+0.026}_{-0.013}$	$0.0169^{+0.0066}_{-0.0059}$
T_{spot}	$\mathcal{U}(2300.00, 3430.00)$	2918^{+97}_{-115}	2989^{+73}_{-76}	3187^{+148}_{-156}	3200^{+45}_{-60}
T_{fac}	$\mathcal{U}(3430.00, 4802.00)$	4137^{+316}_{-543}	3930^{+260}_{-200}	3635^{+170}_{-105}	4232^{+142}_{-110}
T_{phot}	$\mathcal{N}(3430.00, 54.00)$	3508^{+43}_{-46}	3521^{+44}_{-44}	3523^{+43}_{-53}	3634^{+20}_{-25}
$\log g_{\text{spot}}$	$\mathcal{U}(4.34, 5.34)$	$4.63^{+0.13}_{-0.13}$	$4.57^{+0.16}_{-0.14}$	$4.47^{+0.14}_{-0.09}$	$4.50^{+0.11}_{-0.10}$
$\log g_{\text{fac}}$	$\mathcal{U}(4.34, 5.34)$	$4.75^{+0.33}_{-0.28}$	$4.68^{+0.35}_{-0.22}$	$4.88^{+0.29}_{-0.31}$	$4.51^{+0.19}_{-0.11}$
$\log g_{\text{phot}}$	$\mathcal{U}(4.34, 5.34)$	$4.79^{+0.19}_{-0.19}$	$4.76^{+0.19}_{-0.17}$	$4.97^{+0.20}_{-0.20}$	$4.90^{+0.13}_{-0.10}$
χ^2_ν	—	1.49	1.24	1.10	2.04
$\ln Z$	—	2375.2	2383.99	2454.39	2473.06

Fig. Set 15. Retrieved Spectra for Individual Visits

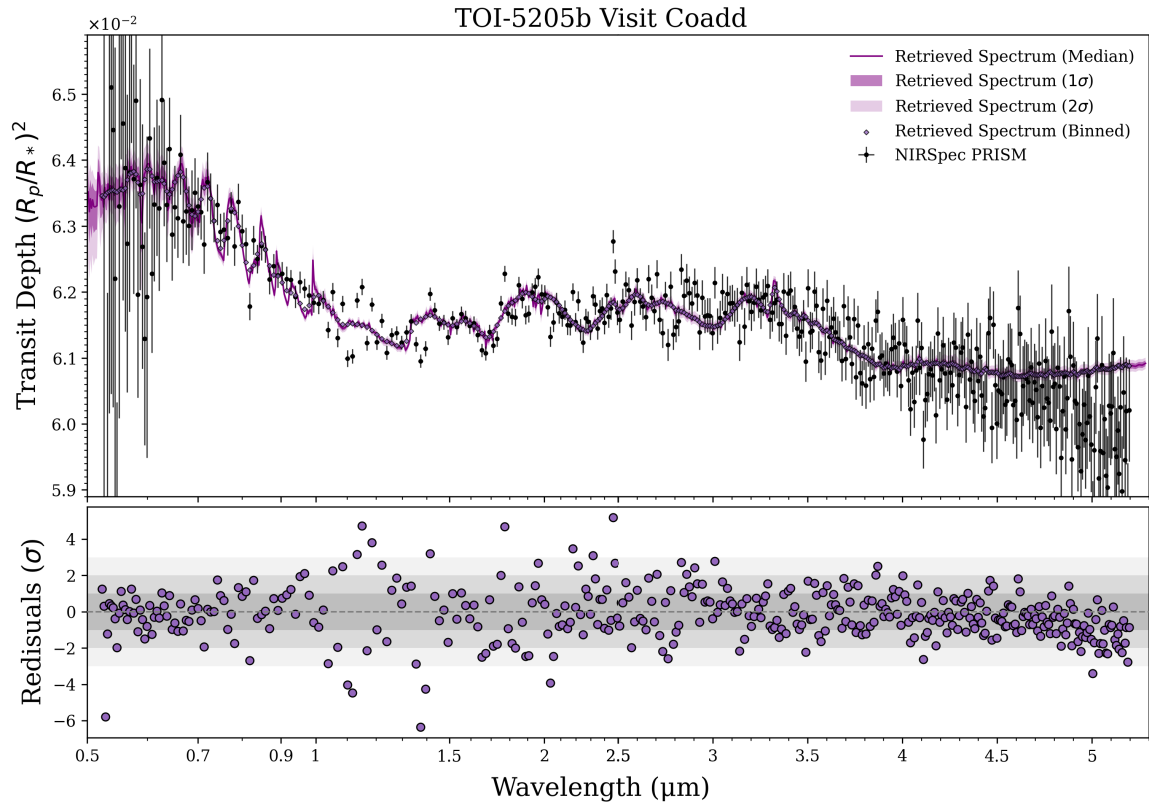


Fig. Set 15.1 – Overview. The three-visit co-added transmission spectrum of TOI-5205b fitted with the cloud free M3.1 retrieval model (top panel) and the residuals on the fit (bottom panel). A logarithmic x-axis is used from 0.5-2.5 μm and a linear x-axis $> 2.5 \mu\text{m}$. The cloudy retrieval fits using model M3.2 are indistinguishable from those shown here. The complete figure set (4 images, for three visits plus the combined spectrum) is available in the online journal.

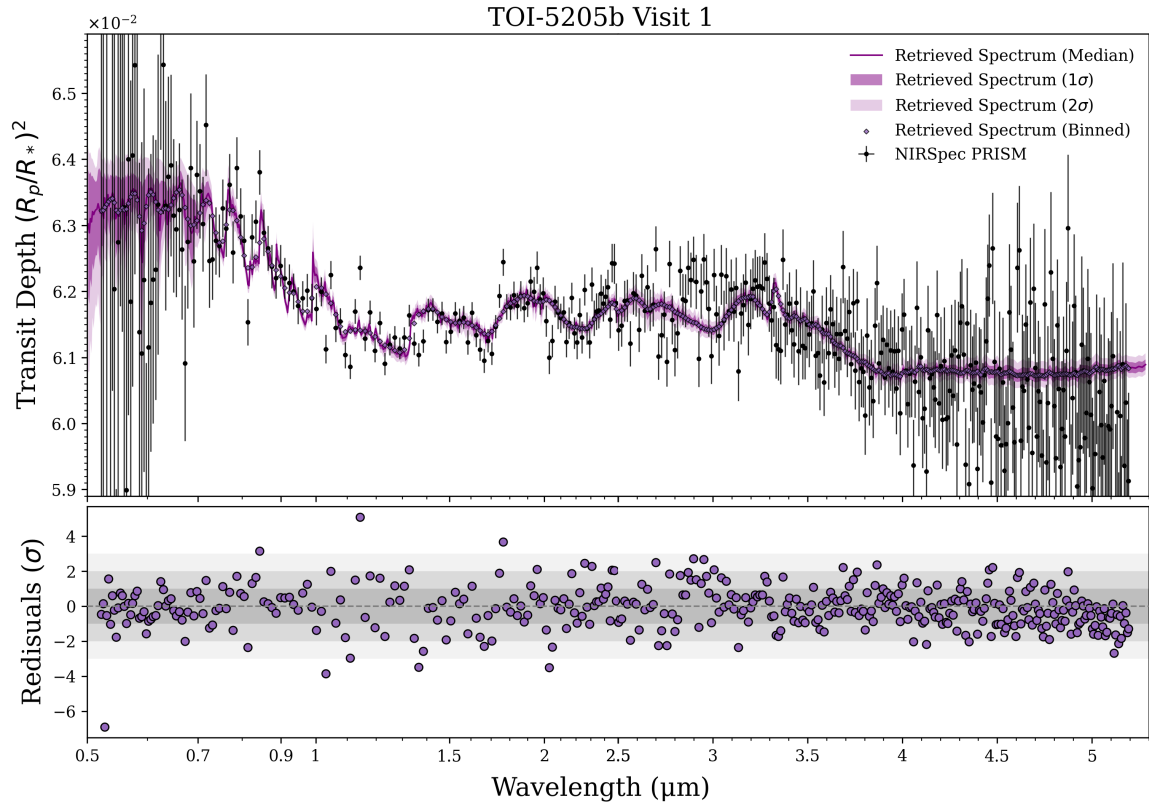


Fig. Set 15.2 – Visit 1. Fitted spectrum and residuals to the Visit 1 spectrum using model M3.1 (as shown in Fig. Set 15.1).

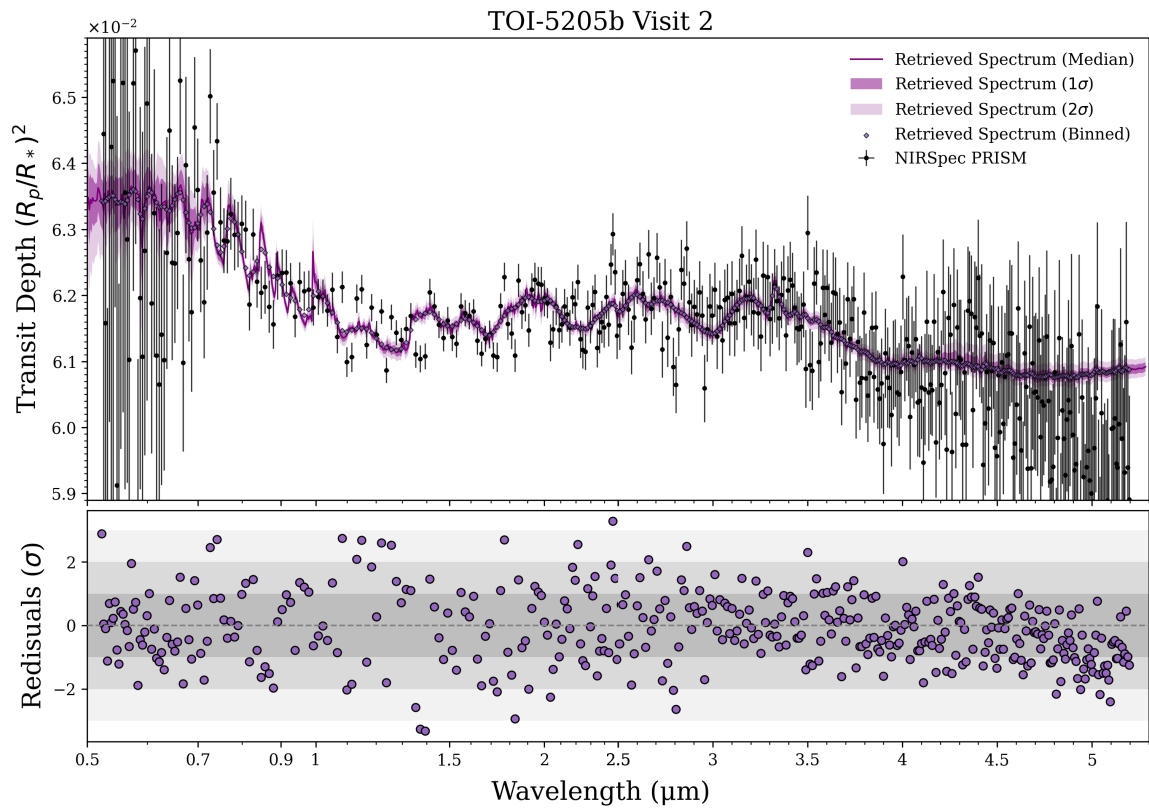


Fig. Set 15.3 – Visit 2. Fitted spectrum and residuals to the Visit 2 spectrum using model M3.1 (as shown in Fig. Set 15.1).

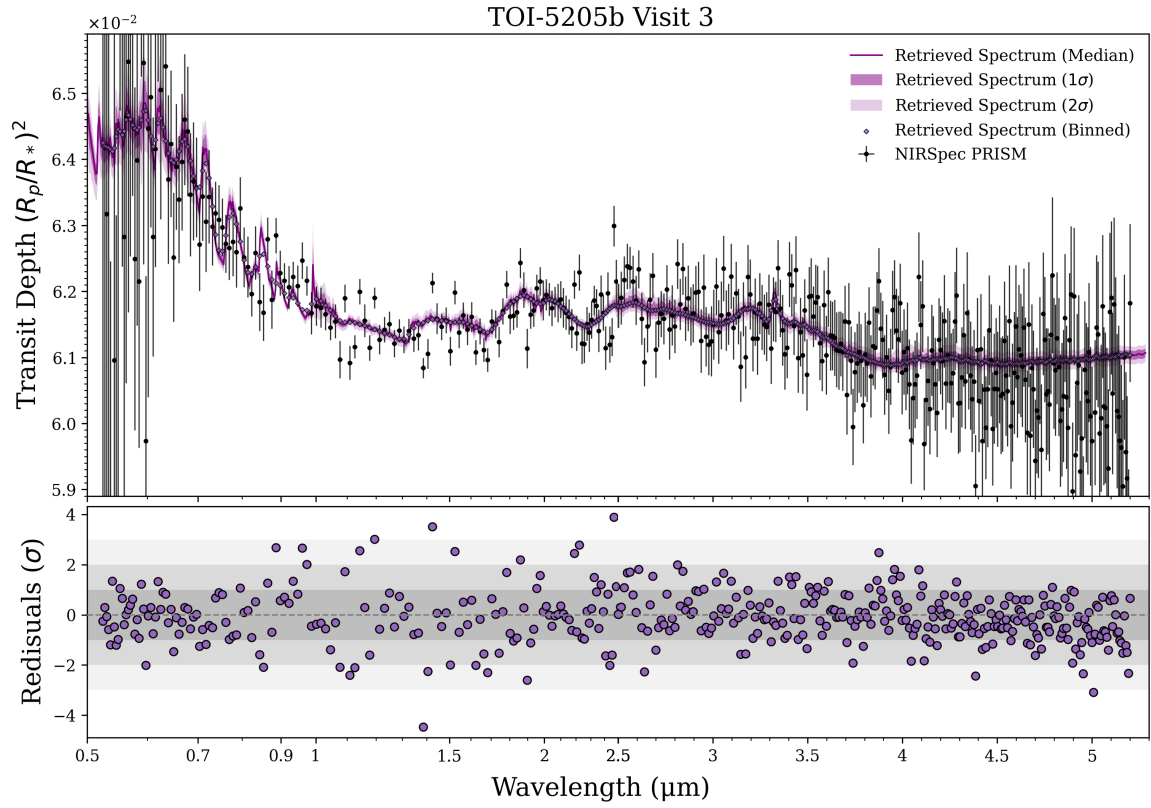


Fig. Set 15.4 – Visit 3. Fitted spectrum and residuals to the Visit 3 spectrum using model M3.1 (as shown in Fig. Set 15.1).

E.3. Retrievals on Partial Spectra

To understand how different portions of the transmission spectrum drive the retrieval towards constraints on the planet atmosphere and the contaminating star, we made several wavelength cuts to the co-added transmission spectrum and repeated our previous retrieval simulations using the cloud-free M3.1 model from §5. Figure 16 presents the spectrum with the various models (upper right inset) and 1-D and 2-D marginalized posterior distributions for five different retrievals covering wavelengths of $\lambda > 3.5$, 2.5, 1.5, 0.9, and 0.5 μm . The choice to focus on the spectra at wavelengths longer than these cuts is based on the stronger impact of stellar contamination at bluer wavelengths (see Figure 6; e.g., Seager & Shapiro 2024).

Markedly different results are obtained using data from different wavelength ranges, including many statistically incompatible constraints for the atmospheric temperature, gas abundances, and reference radius. Results for $\lambda > 3.5$ μm show that a high temperature atmosphere with abundant H_2S (a volume mixing ratio of -2.31 ± 0.43) and no CH_4 fits the downward sloped spectrum. For $\lambda > 2.5$ μm a dichotomous result is obtained with a low temperature atmosphere (386 ± 57 K) with abundant CH_4 and no constraint on H_2S . These two longwave only datasets prove to be poor predictors of the shortwave data as they immediately diverge beyond the cutoff. Results for $\lambda > 1.5$ μm are similar to the $\lambda > 3.5$ μm case with high T and high abundances of CH_4 and H_2S , and it offers a good prediction of the shorter wavelength data, except for at 1 μm where the data lack a feature predicted by the models. The $\lambda > 0.9$ μm results are almost entirely consistent with the full wavelength constraints ($\lambda > 0.5$ μm) and show modest temperature atmospheres that are within 1σ of T_{eq} . The primary difference between the $\lambda > 0.9$ and $\lambda > 0.5$ μm cases is the star photosphere, spot and faculae characteristics. In particular, the spot and faculae area covering fractions are much more precisely constrained using the data from 0.5 – 0.9 μm .

E.4. Limited sensitivity to CS_2 and NH_3 in the atmosphere

A carbon-rich atmosphere and a sulfur reservoir present an opportunity to explore more complex sulfur chemistry. Recent tentative detections of carbon disulfide (CS_2) in the atmosphere of TOI-270d ($350 \text{ K} \leq T_{\text{eq}} \leq 380 \text{ K}$) using JWST (Benneke et al. 2024; Holmberg & Madhusudhan 2024) motivated an investigation in other sulfur reservoirs beyond H_2S and SO_2 . In atmospheres that are oxygen-poor, Mukherjee et al. (2024) demonstrate that carbon sulfides may be sig-

nificant reservoirs of the S-inventory in the upper atmosphere. The importance of carbon sulfides is expected in planetary atmospheres cooler than TOI-5205b ($T_{\text{eq}} \leq 600 \text{ K}$), however, because we do not detect SO_2 , we investigated the expected presence of CS_2 using the best-fitting VULCAN grid (see §4.2). For TOI-5205b, the sulfur-enhanced atmospheres ($f_S=100$) provide the maximum VMRs of $\log[\text{CS}_2] = -8.56$ ($\log K_{zz} = 9$) or $\log[\text{CS}_2] = -8.22$ ($\log K_{zz} = 6$). H_2S remains the most abundant sulfur-bearing molecule for TOI-5205b at a VMR consistent with the free chemistry retrieval. Even in the most sulfur-enhanced model allowing for disequilibrium chemistry, CS_2 is not expected to be a significant component in the atmosphere of TOI-5205b.

We were also motivated to investigate the presence of NH_3 by recent JWST observations of WASP-107b, a warm Neptune orbiting a Sun-like star with an equilibrium temperature ($T_{\text{eq}} \sim 750 \text{ K}$) comparable to TOI-5205b, which has a detection of ammonia in its atmosphere (Welbanks et al. 2024; Sing et al. 2024). NH_3 , like CH_4 , is expected to become readily observable in the atmospheres of warm gas giants and a significant reservoir for nitrogen (Fortney et al. 2020; Ohno & Fortney 2023a,b). From the POSEIDON free chemistry retrieval for the modified M3.1 model that included ammonia (see §5.2.3), we recovered a marginal (2σ) detection of $\log[\text{NH}_3] = -6.64_{-0.73}^{+0.35}$. For reference, the best-fitting VULCAN models predicts a value of $\log[\text{NH}_3] = -5.86$. At the equilibrium temperature of TOI-5205b, the dominant spectral feature of NH_3 is expected between 2.9 – 3.1 μm . Welbanks et al. (2024) demonstrate the difficulty in detecting NH_3 with multiple instruments (HST/WFC3, JWST/NIRCam, and JWST/MIRI) and used a cross-validation technique to identify this wavelength range as the most important for detecting NH_3 in WASP-107b. In TOI-5205b, this is a region where stellar contamination, H_2S , and CH_4 all contribute to the spectrum (see Figure 6), such that the models do not differ significantly with the inclusion of NH_3 . We conclude that while TOI-5205b is very similar in temperature to WASP-107b, the transmission spectrum of TOI-5205b does not provide evidence for NH_3 in its atmosphere.

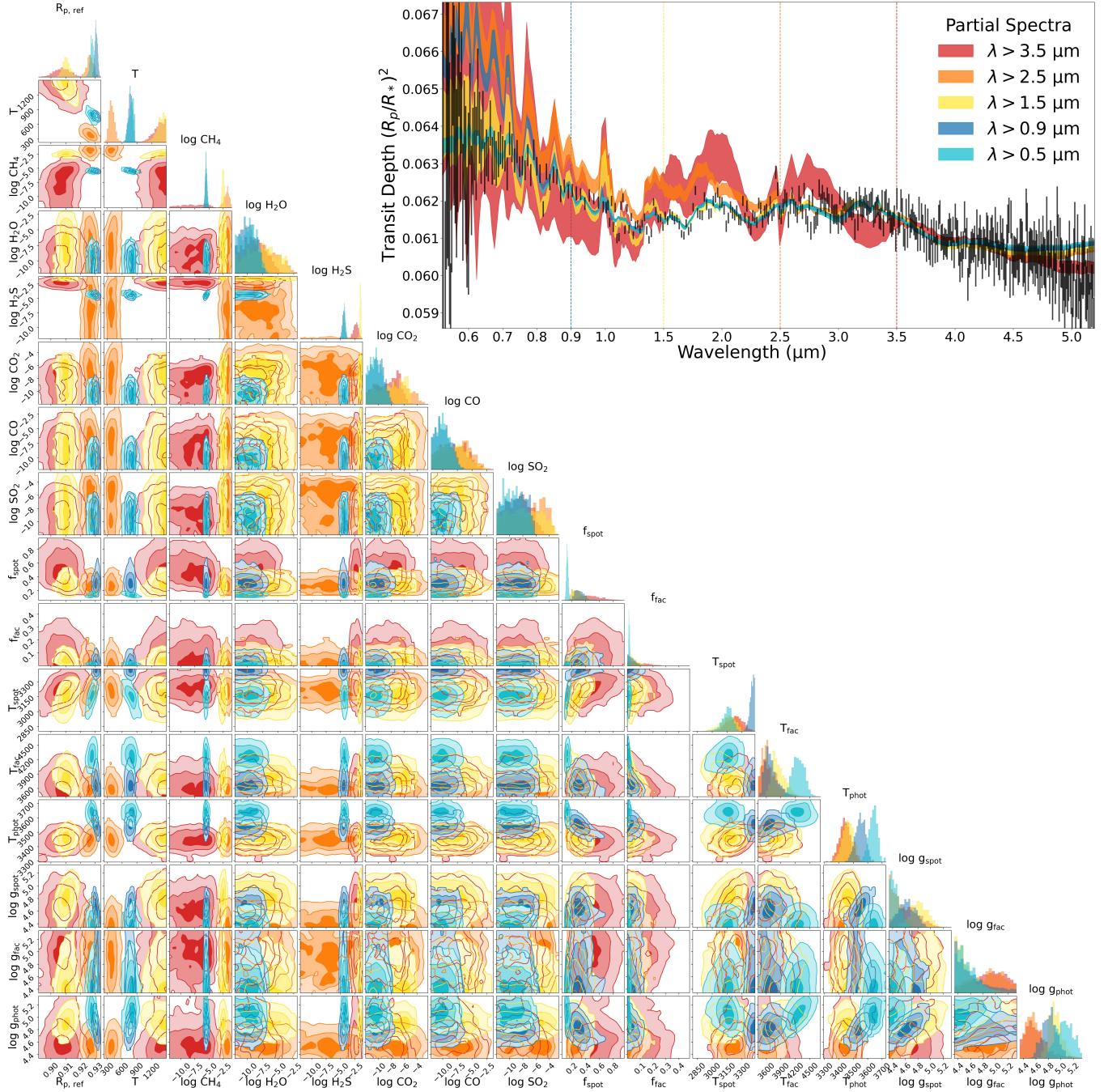


Figure 16. Posterior probability distributions for stellar and planetary parameter (lower left corner of subplots) and 1σ range of fits to the spectrum (upper right panel) from retrievals covering only selected wavelength ranges of the transmission spectra. Colors indicate the short wavelength limit for the different cases. Transmission spectrum envelopes extend shortward of the dashed line corresponding to the respective case wavelength limit to visualize the posterior predictive accuracy of the retrieval constraints on the omitted portion of the data. These predictions illustrate the many possible (mis)interpretations that could emerge from access to limited wavelength data.